

Benchmarking of the Simulation of the ATLAS Hall Background

Dissertation

zur Erlangung des Grades eines Doktors
der Technischen Wissenschaften
an der Technischen Universität Graz

vorgelegt von
Dipl. Ing. Helmut Vincke

am Institut für Theoretische Physik

Begutachter:

Ao.Univ. Prof. DI. Dr. Christian W. Fabjan

Ao.Univ. Prof. DI. Dr. Hansjörg Müller

Graz, Oktober 2000

Kurzfassung

Ein neuer Teilchenbeschleuniger, der sogenannte “Large Hadron Collider (LHC)” wird im Jahr 2005 am CERN bei Genf in Betrieb genommen. Diese Maschine wird hauptsächlich mit Protonen betrieben. Die Energien, welche bei den Proton-Proton (p-p) Kollisionen erzeugt werden, erreichen einen Wert von 14 TeV. Dieser Wert übertrifft die heutzutage erreichten Energien um einen Faktor 10. Ein weiterer wichtiger Parameter des LHCs ist die erreichbare Luminosität des Beschleunigers, welche mit $10^{34} \text{ cm}^{-2} \text{ s}^{-1}$ angegeben werden kann. Durch den LHC werden Physiker die Möglichkeit bekommen in noch nie erreichte Bereiche der Teilchenphysik vorzustoßen. Hypothesen bezüglich der Physik in diesem Energiebereich werden bestätigt oder durch neue, den Experimenten besser entsprechende, Theorien ersetzt werden.

Eines der vier am LHC installierten Experimente, der “A Toroidal LHC Apparatus (ATLAS)“, wird dazu verwendet werden um die Physik der p-p Kollisionen bei diesen Energien zu untersuchen. Um diese Aufgabe zu verifizieren ist ATLAS mit Meßapparaturen ausgestattet die eine genaue Identifizierung der Sekundärteilchen, welche bei den primären Proton-Proton Kollisionen erzeugt werden, ermöglichen. Da der LHC mit extrem hoher Luminosität bzw. Energie betrieben wird, muß man mit einem sehr hohen Strahlungsuntergrund rechnen. Um das Konzept des Detektors auf die erforderlichen Gegebenheiten in ATLAS anzupassen, muß der Einfluß des Strahlungsuntergrundes auf die Detektoren genau eruiert werden. Die zusätzliche Rate, die in den Müonendetektoren erwartet wird, wurde bereits errechnet. Diese berechnete Rate wurde jedoch mit einem Unsicherheitsfaktor fünf versehen. Dieser Faktor setzt sich aus mehreren Beiträgen zusammen. Der größte Beitrag, nämlich ein Wert von 2.5, wird durch die Simulation des Teilchenuntergrundes hervorgerufen. Diese Rechnungen wurden mit dem Teilchentransportprogramm FLUKA durchgeführt. FLUKA ist noch nie unter solchen Bedingungen getestet worden; daher ist die Genauigkeit dieser Berechnungen nur innerhalb des erwähnten Faktors bekannt.

Die Aufgabe dieser Arbeit bestand darin, dieses Programm für ATLAS äquivalente Bedingungen zu testen. Um dieses Vorhaben umzusetzen, wurden zwei verschiedene Meßreihen durchgeführt. Die meßtechnischen Bedingungen wurden mit FLUKA simuliert um die Ergebnisse mit den Meßresultaten zu vergleichen. Diese Doktorarbeit beschäftigt sich hauptsächlich mit den Simulationen die benötigt wurden um dieses Überprüfungsverfahren durchzuführen. Um einwandfreie Simulationen garantieren zu können, nahm der Autor dieser Arbeit bei allen Messungen aktiv teil.

Die erste Meßreihe beschäftigt sich mit Kalibrationsexperimenten eines BGO Szintillators, um dessen Effizienz auf Photonen und Neutronen meß- und simulations-technisch zu erfassen.

Der weitaus wichtigere Teil dieser Arbeit befaßt sich mit der simulationstechnischen Realisierung eines Experimentes, welches Ähnlichkeiten mit den Untergrundstrahlungsbedingungen in ATLAS aufweist. Dieses Vorhaben wurde mittels eines Gußeisenblocks, welcher von einem Hadronenstrahl mit ATLAS relevanten Energien bestrahlt wurde, in die Tat umgesetzt. Der Eisenblock weist bezüglich seiner Dicke, gemessen in hadronischen Absorptionslängen, sehr große Ähnlichkeiten mit den

Dimensionen des “ATLAS Forward Calorimeters“ auf. Hinter dem bestrahlten Eisenblock wurde ein BGO installiert, welcher restliche Schauerprozesse der hadronischen bzw. elektromagnetischen Kaskade registrierte. Dieser Meßaufbau wurde in FLUKA simuliert, um darauffolgend das Simulationsergebnis mit der Messung zu vergleichen. Da diese Meßbedingungen als ATLAS ähnlich angesehen werden können, verifiziert dieser Vergleich die Verlässlichkeit von FLUKA bezüglich des ATLAS Untergrundes.

Diese Doktorarbeit beschreibt in allen Einzelheiten die simulationstechnische Umsetzung des Meßaufbaues in FLUKA. Weiters werden Simulationsergebnisse im Detail diskutiert und erläutert. Ein anschließender Vergleich mit den Meßergebnissen erlaubt es, den Unsicherheitsfaktor bezüglich der Simulationen wesentlich zu reduzieren und neu zu definieren.

Abstract

The Large Hadron Collider (LHC), mainly to be used as a proton-proton machine, will be operational in the year 2005. This collider will provide primary beam energies and luminosities ten times higher compared to present-day machines. This development opens the possibility to explore particle physics in ranges, which have never been explored before. Physicists will be able to verify or falsify theories regarding these new energy ranges. Furthermore, new, unknown physics will be encountered, which provides us with knowledge concerning particle behavior under conditions similar to the very early state of the universe.

At the LHC, four experiments will be installed. One of them is the **ATLAS** (A Toroidal LHC ApparatuS) experiment. It is a general-purpose detector, which will provide high accuracy measurements in terms of mass and type identifications of particles, emerging from the LHC proton-proton collisions. These new energy domain and luminosity reached in ATLAS will also create new problems. One of these issues is the high particle background rate occurring in the ATLAS detector. This particle background is produced by the hadronic and electromagnetic showers, which are induced in the detector by secondary products of the p-p collisions. The particle background has strong impact on the detectors used in the sense that the detectors have to operate reliably under such radiation conditions. Therefore, a profound knowledge concerning this particle background is necessary in order to design and operate ATLAS properly.

The background radiation field in ATLAS was already calculated with the Monte Carlo simulation program **FLUKA**. Unfortunately, the predictions concerning the background induced counting rates in the muon system of ATLAS are only understood within an uncertainty level of approximately five. The main contribution of this factor can be understood as limited knowledge concerning the ability of FLUKA to simulate these kinds of scenarios. In order to reduce the uncertainty, benchmarking simulations of a measurement scenario similar to the ATLAS background situation were performed. These kinds of simulations will prove to which extent FLUKA is able to provide reliable results concerning the ATLAS background situation.

In the framework of this thesis, benchmarks concerning two different kinds of simulations are performed. Measurements are carried out in order to produce a base for the benchmarking simulations. These measurement situations are reproduced in FLUKA. A subsequent comparison between the measurement and the simulation results yields the level of reliability of the used program. In this work the simulations concerning the benchmark procedure are explained in detail. Furthermore, the comparison with the measurements are presented and discussed. In order to guarantee an accurate reproduction of the measurements in the simulation, the author of this thesis participated also in the measurements. Details about these measurements can be found in [Gsc00].

The first kind of the benchmark deals with the simulation of simple measurements. The measurements are concerned with the response of a BGO scintillator to photons and neutrons. These particles are emitted from radioactive calibration sources.

The main body of the thesis deals with the simulation work concerning a benchmarking procedure related to the ATLAS background situation. A cast iron construction, which is irradiated by a hadron beam, originating from the H6 beamline at CERN, is used to verify the reliability of FLUKA under ATLAS conditions. Not only in terms of hadronic absorption lengths, but also in other respects the chosen set-up can be seen as an analogue to the ATLAS forward calorimeter.

Particles, having ATLAS relevant energies, hit the absorber and produce hadronic and electromagnetic showers. Behind the iron structure the remnants of the shower processes are measured and simulated. The simulation procedure and its encouraging results, including the comparison with the measured numbers, are presented and discussed in this work.

CONTENTS

Kurzfassung	III
Abstract	V
CHAPTER 1	3
1. THE LHC AND THE ATLAS EXPERIMENT	5
1.1. INTRODUCTION	5
1.2. THE LARGE HADRON COLLIDER	5
1.2.1. <i>Design Parameters of the LHC</i>	5
1.3. LHC PHYSICS.....	7
1.3.1. <i>Revelation of the existence of the Higgs boson</i>	7
1.3.2. <i>Minimal Super-Symetric Extension of the Standard Model (MSSM)</i>	10
1.3.3. <i>Super-Symmetry</i>	10
1.3.4. <i>Top Physics</i>	11
1.3.5. <i>B Physics</i>	11
1.3.6. <i>Studies concerning the quark gluon plasma</i>	11
1.4. EXPERIMENTS AT LHC	12
1.4.1. <i>ATLAS</i>	12
1.4.2. <i>CMS</i>	12
1.4.3. <i>ALICE</i>	12
1.4.4. <i>LHCb</i>	13
1.5. THE ATLAS DETECTOR	14
1.6. THE ATLAS MUON SPECTROMETER	17
1.7. BACKGROUND CONDITIONS IN THE ATLAS MUON SPECTROMETER	19
1.8. UNCERTAINTIES OF THE BACKGROUND CALCULATIONS	21
1.9. MOTIVATION FOR THE FLUKA BENCHMARK STUDIES.....	21
CHAPTER 2	23
2. THE MONTE CARLO CODE FLUKA	23
2.1. GENERAL FEATURES OF FLUKA	23
2.1.1. <i>Geometry in FLUKA</i>	24
2.1.2. <i>Tracking</i>	24
2.1.3. <i>Scoring</i>	25
2.1.4. <i>Biasing</i>	25
2.2. DIFFERENT MODELS USED IN FLUKA.....	26
2.2.1. <i>Simulation of the hadronic cascade in FLUKA</i>	26
2.2.2. <i>Simulation of electromagnetic effects in FLUKA</i>	30
2.3. APPLICATIONS	32
2.4. HISTORY OF FLUKA	32
2.5. ATLAS BACKGROUND CALCULATIONS WITH FLUKA.....	34

CHAPTER 3.....	36
3. EVALUATION OF PARTICLE-DEPENDENT BGO RESPONSE	36
3.1. INTRODUCTION	36
3.2. DESCRIPTION OF THE SIMULATED MEASUREMENT DEVICE	37
3.3. BGO DETECTOR RESPONSE TO DIFFERENT GAMMA SOURCES	38
3.3.1. <i>Experimental setup</i>	38
3.3.2. <i>Simulation procedure to obtain measurement comparable results</i>	40
3.3.3. <i>Procedure to obtain particle currents entering the BGO</i>	43
3.3.4. <i>Simulation results</i>	44
3.3.5. <i>Comparison between simulated and measured results</i>	50
3.4. BGO DETECTOR RESPONSE TO DIFFERENT NEUTRON SOURCES	53
3.4.1. <i>Experimental set-up</i>	53
3.4.2. <i>Simulation procedure to obtain measurement comparable results</i>	55
3.4.3. <i>Procedure to obtain particle currents entering the BGO</i>	55
3.4.4. <i>Simulation results</i>	56
3.4.5. <i>Comparison between simulated and measured results</i>	61
3.5. SUMMARY OF THIS CHAPTER.....	64
 CHAPTER 4.....	 65
4. SIMULATION OF THE ATLAS EQUIVALENT MEASUREMENTS.....	65
4.1. INTRODUCTION	65
4.2. SPS AND H6 AREA	66
4.3. ATLAS EQUIVALENT SHIELDING	66
4.4. EXPERIMENTAL SET-UP	67
4.5. SIMULATED BEAM CONDITIONS.....	70
4.6. SIMULATION PROCEDURE FOR OBTAINING RESULTS	71
4.6.1. <i>Simulation of the shower processes induced by the primary beam particles</i>	71
4.6.2. <i>Simulation of energy deposition in the BGO crystal</i>	73
4.6.3. <i>Convoluting the BGO energy deposition spectrum with the BGO resolution function</i>	74
4.7. CALCULATED RADIATION CONDITIONS BEHIND THE DIFFERENT SHIELDING CONSTRUCTIONS	75
4.7.1. <i>Simulated fluences behind the shielding</i>	75
4.7.2. <i>Characterization of events hitting the BGO</i>	83
4.7.3. <i>Hadronic origin of particles entering the BGO</i>	84
4.7.4. <i>Induced counting rates and spectra in the BGO</i>	85
4.8. ASSESSMENT OF THE SYSTEMATIC UNCERTAINTIES OF THE MEASUREMENTS	88
4.8.1. <i>Variable distance between beam and BGO crystal</i>	88
4.8.2. <i>Influence of the carbon contents in the iron absorber</i>	92
4.8.3. <i>Influence of the composition of the primary hadron beam</i>	94
4.8.4. <i>Influences of the size of the BGO crystal</i>	99
4.8.5. <i>Influence of variable absorber depth</i>	101
4.8.6. <i>Influence of the absorber density</i>	104

4.8.7. Influence of the distance between BGO and iron absorber	104
4.8.8. Summary of the systematic uncertainties:.....	105
4.9. SUMMARY OF THIS CHAPTER	106
 CHAPTER 5	107
5. ANALYSIS AND DISCUSSION OF THE RESULTS	107
5.1. INTRODUCTION	107
5.2. COMPARISON BETWEEN MEASURED AND SIMULATED RESULTS	107
5.2.1. Comparison of the total counting rates	107
5.2.2. Comparison between the average energy deposition	110
5.2.3. Comparison of the measured and simulated photon rate	111
5.3. COMPARISON BETWEEN THE SHIELDING CONDITIONS AT H6 AND ATLAS:	113
5.3.1. Prediction of ATLAS background fluences with H6 results:	113
5.3.2. ATLAS background fluence results:.....	116
5.4. CONCLUSION FOR THE ATLAS BACKGROUND UNCERTAINTY.....	116
5.5. SUMMARY OF THIS CHAPTER.....	117
 CHAPTER 6	119
6. CONCLUSION	119
APPENDIX A	121
BGO NEUTRON CROSS SECTION DATA USED IN FLUKA	121
Low energy neutron group limits.....	121
Energy limits of neutron induced photons	122
FLUKA cross section data used for Oxygen.....	123
FLUKA cross section data used for Germanium.....	125
FLUKA cross section data used for Bismuth.....	127
APPENDIX B	129
Revision history.....	129
APPENDIX C	133
GLOSSARY	133
BIBLIOGRAPHY	135
ACKNOWLEDGEMENTS	140
CURRICULUM VITAE.....	140

CHAPTER 1

1. The LHC and the ATLAS experiment

1.1. Introduction

This chapter is primarily concerned with the high-energy physics experiment facility ATLAS which will be located at the Large Hadron Collider (LHC). This machine is being constructed to produce new states of matter with masses beyond 1 TeV. With the capacity to produce such high energies, it will be possible to research matter in a state comparable to the matter of the universe 10^{-17} to 10^{-6} s after the Big Bang. New physics at temperatures up to 10^{16} Kelvin will also reveal its secrets. This chapter discusses details about the design parameters of ATLAS and the LHC. Furthermore, an overview concerning all other detectors, which will be build around the LHC collider, is provided.

1.2. The Large Hadron Collider

1.2.1. Design Parameters of the LHC

The Large Hadron Collider is planned to be used mainly as a proton-proton (p-p) machine and will replace the Large Electron Positron collider (LEP) in the year 2005. In LEP, electrons and positrons were accelerated up to a center of mass energy of around 200 GeV. Due to the high synchrotron radiation of these particles in the LEP circle, which has a circumference of 27 km, this energy represents an upper limit for the existing circular e^+e^- collisions.

The existing LEP tunnel system will be used for the construction of the LHC. The fact that protons instead of electrons are accelerated implies a lower energy loss due to the afore mentioned synchrotron radiation effect. With this machine, protons will be accelerated in two separate beam lines to a center of mass energy of 14 TeV. In comparison to leptons, the proton has a substructure consisting of quarks and gluons. Therefore, the kinetic energy is shared among these particles. The proton-proton collision has to be seen as a collision of their constituents, each of them carrying only a certain part of the whole energy. At the position of the four interaction points, the particle bunches will have a transverse radius of 15 μm and a length of 30 cm. The time between the single bunches in the accelerator will be 25 ns. The LHC will be operated up to a luminosity of $10^{34} \text{ cm}^{-2} \text{ s}^{-1}$. This implies a collision rate of 10^9 proton-proton interactions per second. The LHC system consists of two separated beamlines (housing counter rotating beams), which are fed by the Super Proton Synchrotron (SPS) with protons having an energy of 450 GeV. A sketch of the whole LHC facility is shown in Figure 1.1.

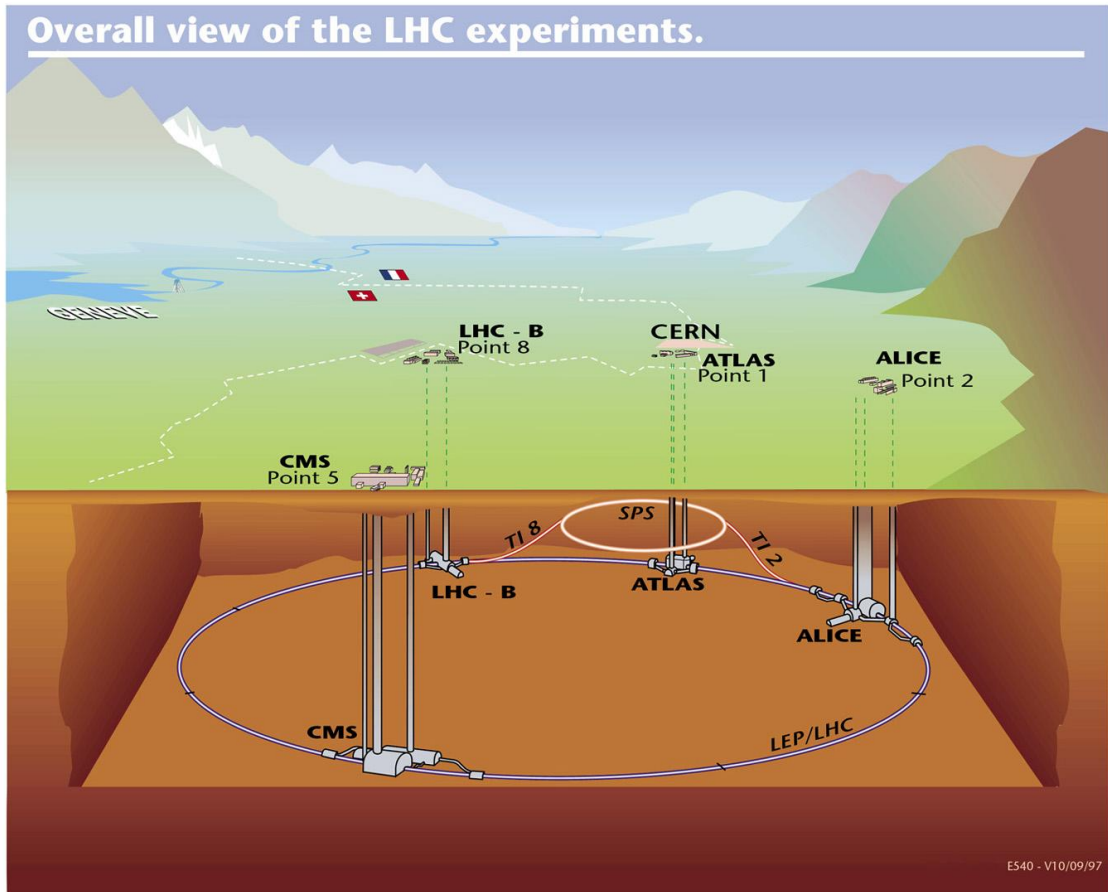


Figure 1.1: Schematic picture of the LHC accelerator facility, including its experiments at CERN

Apart from accelerating protons, it will be also possible to use the LHC as a collider facility in order to produce collisions of lead ions. In this operation mode a center-of-mass energy in the range of PeV will be reached.

For realizing these particle energies super-conducting NbTi bending magnets, quadrupols and accelerating cavities will be necessary in order to keep the accelerated charged particles in a well-defined path within the 27 km circle. Each of the 1300 super-conducting dipoles will produce a magnetic field of 8.4 Tesla. For reaching the necessary currents, the magnet materials have to be operated at 1.9 K. The whole LHC facility, including its detectors, is installed underground approximately 100 m below the surface.

1.3. LHC physics

The main goal of the LHC experiments is to study particle physics at the TeV scale. In these investigations, which will last more than a decade, the following topics are examples of major interests:

- Higgs boson
- Minimal Super-Symmetric Extension of the Standard Model (MSSM)
- Super-Symmetry
- Top Physics
- B Physics
- Studies concerning the quark gluon plasma

The first of these issues, the Higgs boson, is discussed in more detail in this chapter. The others issues will be explained only summarily.

1.3.1. Revelation of the existence of the Higgs boson

The symmetry breaking in the electroweak sector $SU(2) \times U(1)$ of the Standard Model is not yet understood. In the Standard Model the Higgs mechanism is introduced, This mechanism implies also the existence of the Higgs boson. This particle can be seen as the interaction particle of the Higgs field. The mass of each particle originates from its coupling with this field. This theory predicts a particle mass of the Higgs boson between 80 and 1000 GeV. Final results of LEP experiments found "possible" evidences for Higgs bosons having a mass of ~ 115 GeV. If one can exclude that these events originate from the Higgs boson decay, the mass of this particle has to be higher than 110 GeV.

If the Higgs mass is assumed to be of 500 GeV, the cross section at LHC concerning its production is calculated to be 1 pb. This value increases with decreasing particle mass. Taking into account this value, a Higgs production event rate of 10^5 events at a mass of 500 GeV per year can be expected. The most promising production channels in the LHC concerning the Higgs boson can be found in the gluon-gluon (especially at low energies) and the $WW(ZZ)$ fusion. The Feynman diagrams of 4 different interactions, which produce a Higgs particle can be found in Figure 1.2. Furthermore, the cross sections of the p-p collisions which lead to a Higgs production is displayed in Figure 1.3.

After its production, the Higgs decays through one or more steps into particles, which can be measured directly or via a measurement concerning the missing energy. The possible decay modes of the Higgs decay can be found in Figure 1.4.

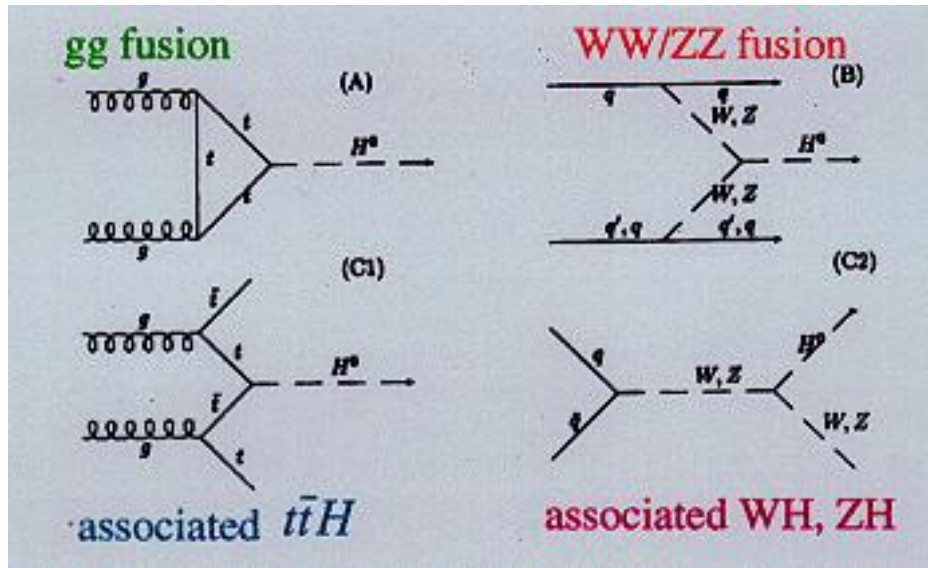


Figure 1.2: Feynman diagrams concerning the Higgs production, induced by a p - p collision

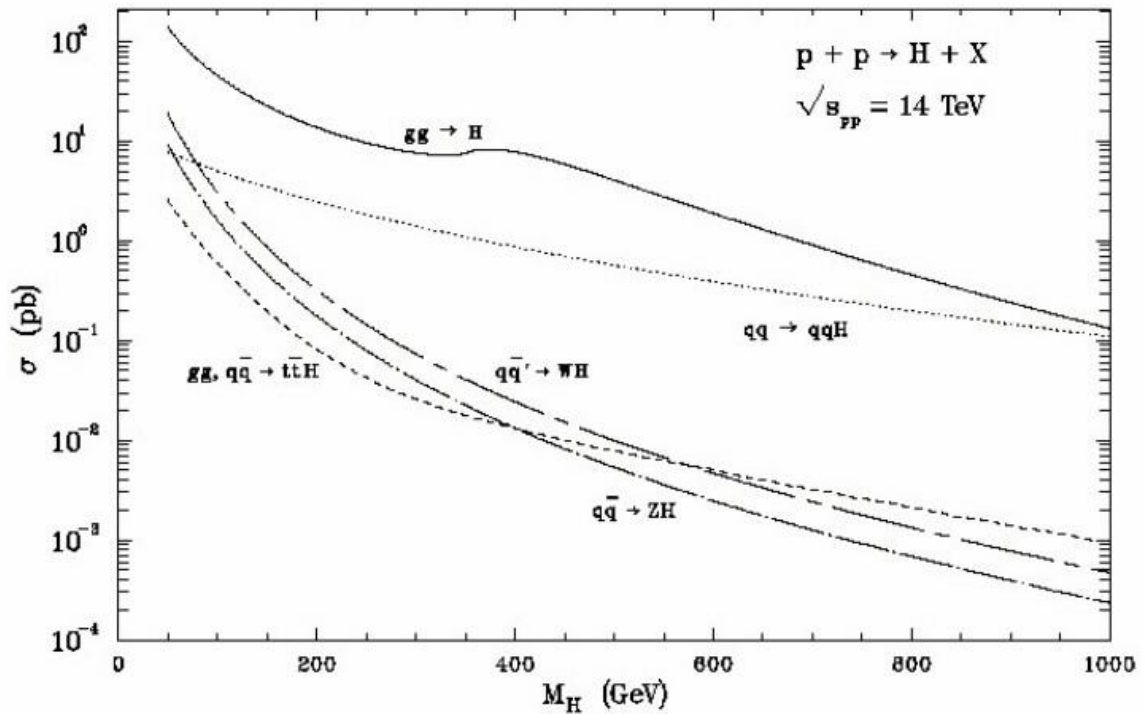


Figure 1.3: Higgs production cross section of a 2×7 TeV p - p collision as a function of the Higgs mass.

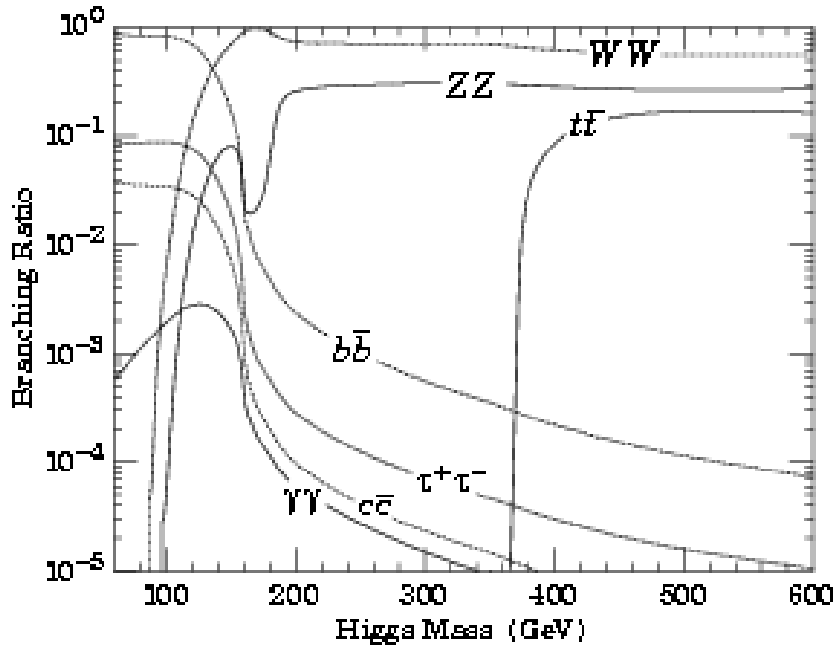


Figure 1.4: Higgs decay branching ratio as a function of the Higgs mass

Referring to Figure 1.4, one can see that the Higgs decay can be divided into 3 different mass regions:

1. **Low-mass region:** If the Higgs has a mass below 120 GeV, its decay is dominated by the $b\bar{b}$ channel ($\sigma \sim 20\text{pb}$). The coupling to fermions increases with the fermion mass. Therefore, the Higgs decays mainly into b quarks, which have highest possible mass in that energy range. The main problem with this channel is the huge QCD background. The signal to noise rate is far below 10^{-5} . Therefore, a kind of additional signature of the Higgs production has to be found. If one checks the production channels, where the Higgs production is accompanied by a production of other particles ($W, Z, t\bar{t}$), the necessary additional identification process for the Higgs decay is found (see Figure 1.2). These additional particles decay into leptons, which can be measured either in the electromagnetic calorimeter or by missing energy (neutrinos) detection.

A further possibility to detect the Higgs boson in the low energy range can be found by searching for the $H \rightarrow \gamma\gamma$ channel. The ratio between processes having the same final state as the Higgs signal and the desired signal rate is only 1:60. Besides this direct $\gamma\gamma$ production, other channels occur which fake mainly by jet decays a Higgs decay production of two photons. The electromagnetic calorimeter has to be able to exclude these events via an excellent gamma jet separation capability (very challenging for the EM calorimeter). This additional background is 10^8 times higher than the expected $\gamma\gamma$ rate originating from the Higgs decay. Another disadvantage of this decay channel is its low cross section ($\sigma \sim 50\text{fb}$). Its branching ratio is only 10^{-3} .

2. **Intermediate mass region:** This region covers a range between 120 and the 800 GeV. If the Higgs has a mass within these values, it will mainly decay into a $WW^{(*)}$ or $ZZ^{(*)}$ pair. The star indicates that one of the produced particles is virtual. A Higgs with a mass below 160 GeV (W) or 180 GeV (Z), respectively, decays into a real and a virtual bosons. Above this level, two real bosons emerge from its decay. In the lower part of this range, the complete decay modes can be written as:

$$\begin{aligned} H &\rightarrow WW^* \rightarrow l\nu l\nu \\ H &\rightarrow ZZ^* \rightarrow ll ll \end{aligned}$$

For the higher mass, the following decay modes become valid:

$$\begin{aligned} H &\rightarrow ZZ \rightarrow ll ll \\ H &\rightarrow ZZ \rightarrow ll \nu\nu, l\nu \text{ jet jet} \\ H &\rightarrow WW \rightarrow l\nu \text{ jet jet} \end{aligned}$$

The channel, where two real Z's decay into four leptons is considered the “gold plated channel”. It has almost no background. But, on the other hand, its production probability is quite low. The four leptons have a high transverse momentum ($5 \text{ GeV}/c < p_T < 50 \text{ GeV}/c$). In order to achieve a good acceptance for such events, the geometrical acceptance of leptons has to be maximized. Concerning background in this intermediate mass region, one should mention that the background rate drops above 180 GeV significantly.

3. For a Higgs mass above 800 GeV other decay channels than the four lepton decay become more important. The heavy Higgs decays with a more than six times higher probability in two leptons and two neutrinos or in a lepton, a neutrino and two jets. In order to detect the escaping neutrinos, the missing energy of the whole process has to be measured.

1.3.2. Minimal Super-Symmetric Extension of the Standard Model (MSSM)

This theory is the simplest extension of the Standard Model and is characterized by having two Higgs doublets. This Higgs spectrum contains one charged Higgs bosons (H^\pm), two neutral scalars (h,H) and one pseudoscalar (A).

1.3.3. Super-Symmetry

If Super Symmetric (SUSY) particles exist then they will be produced at the LHC up to a mass of 5 TeV. Some of these SUSY particles are supposed to be stable. Considering their interaction cross section with normal matter, the theory claims a very low value. In case of their existence, these particles will be detected via the measurement of missing energy. The existence of this kind of particles could be seen as a possible explanation of existing dark matter in the universe.

1.3.4. Top Physics

At LHC energies a large number of $t\bar{t}$ (about 10^7 per year) will be produced. This allows further studies concerning properties like mass, decay channels and coupling of this quark.

1.3.5. B Physics

The main issue of B physics is the observation of the CP violation. Accurate knowledge of this topic could explain why the universe consists mainly of matter instead of antimatter. B physics will be investigated with the LHCb project. But also CMS and ATLAS have the capability to study reactions of interest concerning this issue.

1.3.6. Studies concerning the quark gluon plasma

In the early stage of the universe, matter was in a high-energy state, where quarks could move without being captured in confinement. This state will be realized by collisions of lead ions with each other. The detector, which deals in a dedicated way with this effect, is called ALICE.

In order to investigate the mentioned effects a particle collider like the LHC is absolutely necessary. If one examine the graph shown in the Figure 1.5, it becomes obvious that a discovery of the Higgs particle requires energies and luminosities at the level provided by the LHC.

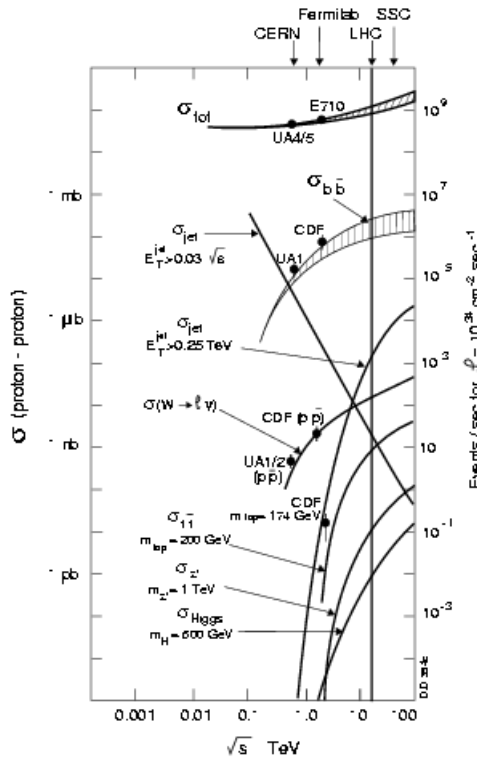


Figure 1.5: Energy dependent p-p cross sections.

1.4. Experiments at LHC

Four different detectors will be installed at the LHC. Two will be general purpose proton-proton detectors. Two other additional detectors will have more specialized purposes. This chapter provides a short overview about these four new detectors at CERN.

1.4.1. ATLAS

The ATLAS (A Toroidal LHC ApparatuS) detector is a general purpose detector which consists in principal of three parts. These parts are the Inner Detector, the Calorimeter and the Muon System. The total system is covered by a magnetic field, which has in the inner part of the detector a strength of two Tesla. Around the muon chambers a field of 0.5 Tesla is induced by the magnets. More detailed information about this detector system can be found in Chapter 1.5.

1.4.2. CMS

The Compact Muon Solenoid: This detector can be seen also as a general purpose detector, designed to run at the highest luminosity at the LHC. The CMS detector is optimized for the search of the SM Higgs boson over a mass range from 90 GeV to 1 TeV. If the Higgs does not exist at all, CMS has also the ability to detect a wide range of possible signatures concerning alternative electro-weak symmetry breaking mechanisms. Furthermore, this detector is also well adapted for the study of top, beauty and τ physics at lower luminosity. Moreover, it will cover several important aspects of the heavy ion physics program. This detector is designed to identify and measure muons, photons and electrons with high precision. The energy resolution for these particles will be better than 1% at 100 GeV. A large super-conducting solenoid is located at the core of the CMS detector. This magnet generates a uniform magnetic field of 4 Tesla. The choice of a strong magnetic field leads to a compact design for the muon spectrometer without compromising the momentum resolution up to rapidities of 2.5. A high resolution crystal electromagnetic calorimeter, designed to detect the two photon decay of an intermediate mass Higgs, is located inside the coil. Hermetic hadronic calorimeters surround the intersection region up to $\eta = 4.7$. The CMS detector will have a mass of 12500 tons. It is interesting to know that the mass of the Eiffel Tower in Paris has a value of 10000 tons. Further details concerning this detector can be found in [CMS94].

1.4.3. ALICE

The ALICE (A Large Ion Collider Experiment) Collaboration builds a detector which is dedicated to explore heavy-ion (lead-lead) collisions. The aim is to study the physics of strongly interacting matter at extreme energy densities. Under these conditions the formation of a new phase of matter, the quark-gluon plasma, will be researched. The properties of such a phase are key issues in QCD for the understanding of confinement and of chiral-symmetry restoration. For this purpose, it is intended to carry out a comprehensive study of the hadrons, electrons, muons and

photons produced in the collision of heavy nuclei. Further details concerning this detector can be found in [ALI95].

1.4.4. LHCb

The LHCb detector will be built as an open forward collider which will be well suited to study CP violation in the B decay for many years. This machine will be an optimized apparatus in order to research B physics events. It will be designed to provide a good particle and mass identification capability. Furthermore, an excellent time resolution of this detector can be expected. The interaction rate of the lead-lead collisions is 15 MHz. This yields a b-hadron production rate of 75 kHz. Further details concerning this detector can be found in [LHC98].

1.5. The ATLAS Detector

ATLAS (A Toroidal LHC ApparatuS) is a general purpose detector which will exploit the full potential of the LHC proton-proton program. The LHC will provide 10 times higher center of mass energies and 100 times higher proton-proton collision rates than existing colliders. This will open a new frontier in physics and ATLAS will explore this great potential.

In order to explore the physics of interest at LHC energies with high precision, ATLAS has to be able to perform accurate measurements concerning the properties of the following particles:

- Charged leptons
- Photons
- Non-interacting particles, such as neutrinos, through missing energy measurement
- Hadronic jets
- Bottom quarks

The ATLAS detector (shown in Figure 1.6) will be 22 m high, 44 m long, and will weigh 7000 tons.

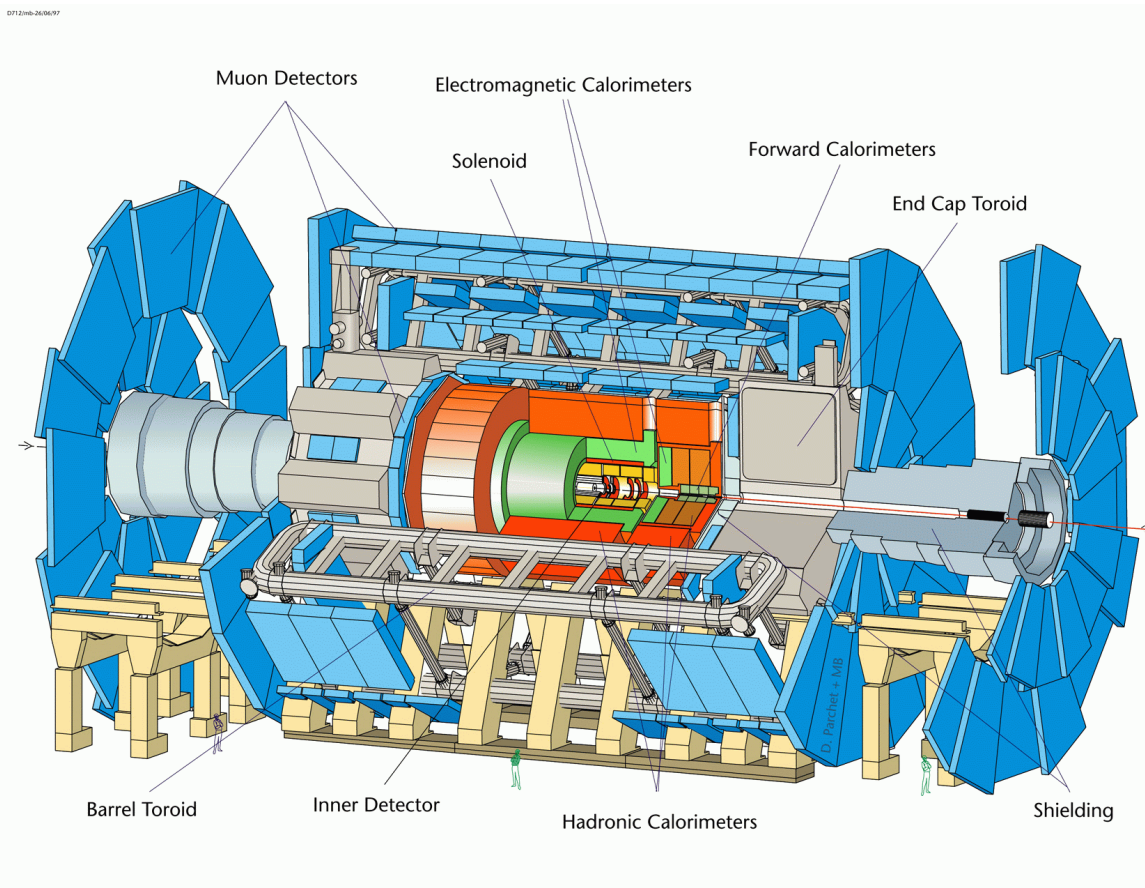


Figure 1.6: View of the ATLAS detector

ATLAS consists of three subsystems:

1. **The Inner Detector:** This tracker, which is pictured in Figure 1.7 is equipped with semi-conductor pixel and strip detectors, which provide high-accuracy measurements of charged particles trajectories. The silicon pixel detector is assembled of three barrel layers consisting of 140 million pixels which provide a resolution of about $10\text{ }\mu\text{m}$ in $r-\phi$ and of $50\text{ }\mu\text{m}$ in z direction. The so-called **Semi-Conductor Tracker (SCT)** contains 4 double layers of silicon strip detectors. These detectors measure the track with small angle stereo giving a resolution of about $20\text{ }\mu\text{m}$ in $r-\phi$ and 0.7 mm in z . The SCT system, is surrounded by the **Transition Radiation Tracker (TRT)**. This part of the Inner Detector is built of 420000 proportional drift tubes, having a diameter of 4 mm. Each track passes through more than 30 tubes, giving excellent pattern recognition of the track. Furthermore, electrons can be identified by their characteristic transition radiation. The Inner Detector is embedded in a magnetic field of 2 T, which is produced by a superconducting solenoid. More details concerning this detector part can be found in [ATI97].

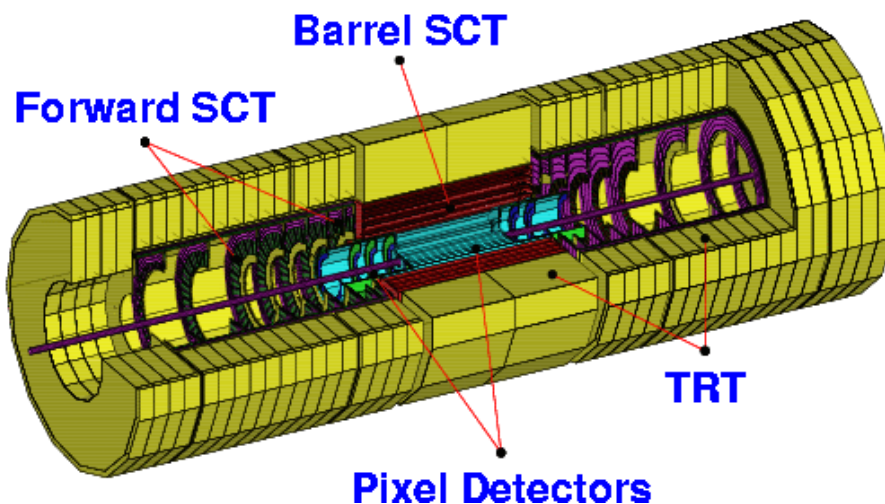


Figure 1.7 The ATLAS Inner Detector

2. **The Calorimeter Structure:** The calorimeter is divided into two parts. The inner part, the Electromagnetic Calorimeter, is optimized for the absorption and measurement of electromagnetic particles. The outer part, which has to absorb and measure hadronic particles, is called Hadronic Calorimeter. The structure of the calorimeter can be found in Figure 1.8. More details concerning this part of ATLAS can be found in [ATC96]

- *Electromagnetic calorimeter:* The electromagnetic calorimeter is a lead – liquid Argon detector, which has an accordion-shaped structure. The lead is well suited to stop electromagnetic particles, and the liquid argon technology can be seen as very radiation resistant. The main features of this detector are a good energy resolution, a good hermeticity and an excellent long-term stability of the detector response. This detector part will also provide a trigger

system in order to reject uninteresting events. The thickness of this detector measured in radiation lengths will be $24 X_0$ in the barrel region and will exceed $26 X_0$ in the forward regions.

- *Hadronic calorimeter:* The barrel hadronic calorimeter is adjacent to the electromagnetic calorimeter and has an outer radius of 4.23 m. The materials used for the hadronic calorimeter vary with the pseudo-rapidity. For $|\eta| < 1.6$, a sampling calorimeter is used with iron as absorber and “scintillating tile” as active material. In the range $1.5 < |\eta| < 4.9$ a hadronic liquid argon calorimeter is used. The end cap hadronic calorimeter ($|\eta| < 3.2$) is a copper liquid argon detector which has a parallel plate layout. The forward calorimeter, covering $|\eta| < 4.9$, has to withstand a high radiation level. It is a matrix consisting of mainly iron, copper and tungsten. This matrix system is filled with liquid argon.

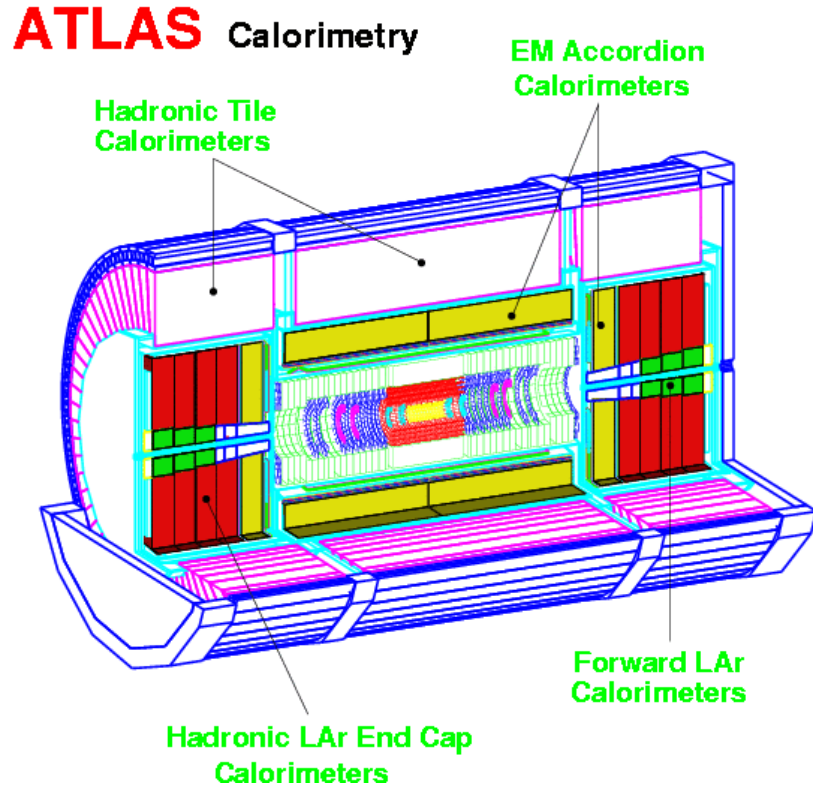


Figure 1.8: Layout of the ATLAS calorimeter system

3. **The Muon Spectrometer:** The ATLAS Muon Spectrometer consists of four different types of chambers. Two of them provide the system with muon trigger signals. The other two types are precision chamber systems. Further details about the muon detector system can be found in the next chapter.

1.6. The ATLAS Muon Spectrometer

Emerging muon tracks have to be identified after their passage through 10 – 15 absorption lengths (λ) of calorimeter material. This identification is carried out via measuring traces, which are induced by muons in the spectrometer structure. The path of the muons are bent as a function of their momenta by a magnetic field, having a strength of ~ 0.5 T. In Figure 1.9 one can see a cross-section of the muon spectrometer along and perpendicular to the beamline. In order to describe the muon detector system, one has to describe the regions defined by different pseudo rapidities. In the region from $|\eta| = 0$ to $|\eta| = 1$ the detector is arranged in a barrel structure around the collision point. This structure consists of three barrel layers, which are assembled at a radial distance of 5 m, 7.5 m and 10 m to the detector center. In the forward region, the “end-cap chambers” cover the area up to $|\eta| = 2.7$. The four chamber layers of this system are perpendicularly aligned to the beamline (see dark MDT chambers in left picture of Figure 1.9). The distance between the single layers and the p-p collision point are 7 m, 10 m, 14 m and 21-23 m.

The magnet system, which provides the outer part of ATLAS with a constant magnetic field, consists of three parts. The barrel toroid, which covers the barrel chambers and two end-cap toroids covering the chambers close to the beam axis. The magnet technology used is an air-core super-conducting toroid magnet. The low average density of this structure prevents excessive multiple scattering in the magnet material.

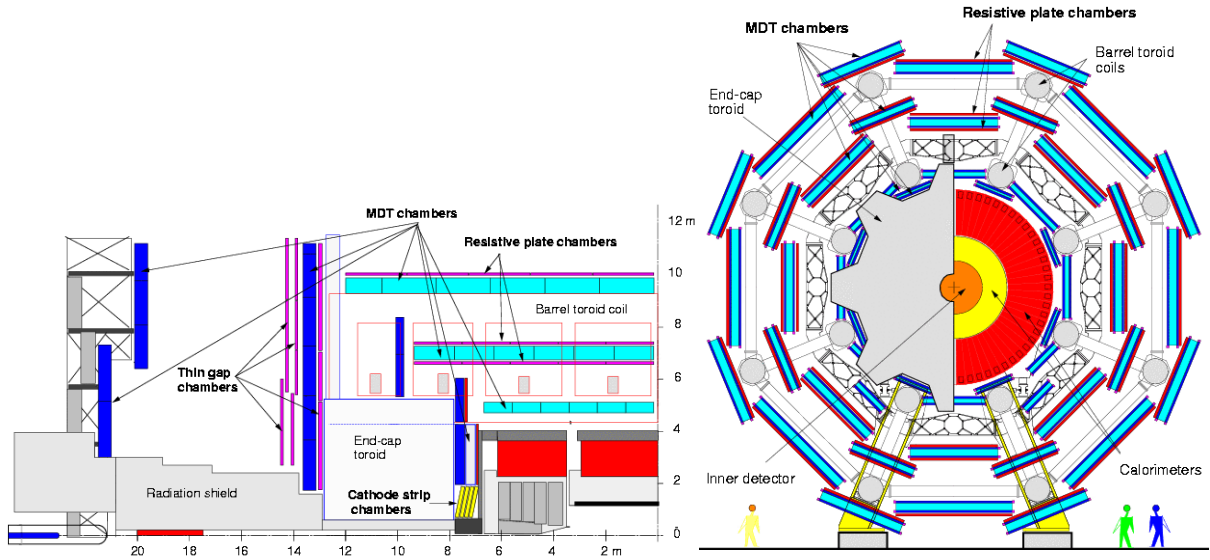


Figure 1.9: Cut through the ATLAS detector showing the muon chamber system.

In order to describe this spectrometer more accurately, one has to mention the chamber technologies used. In the Muon Spectrometer we have four different kinds of detectors. Two of them are used as trigger chambers and two are used as precision chambers.

Precision Chambers: In order to perform precision measurements of the muon trajectories, **Monitor Drift Tubes (MDTs)** are used over most of the solid angle. These detectors are arranged in the mentioned layer system in order to perform “sagitta” measurements of the muon track. Each chamber can be seen as an assembly of drift tubes, consisting of an aluminum cylinder filled with Ar/CO₂ (93/7) as counter gas. In the middle of the tube, a wire establishes an electric field. If a muon crosses a tube, an electron avalanche is induced in the gas. The drift time of the electrons, starting at the position of the muon path, to the wire is measured. This procedure provides the detector with the distance between the muon path and the wire. By means of a very accurate alignment system, the position of each tube in the ATLAS detector is known with a precision of $< 40\mu\text{m}$. As result, the position of the track in the bending plane can be determined. The information, concerning the position along the axis of the tube, is provided by the trigger chambers. The momentum of the muon can be calculated via the information obtained by all three layers of muon chambers. The bending of the muon track by the known magnetic field specifies this value.

Within the range of $2.0 < |\eta| < 2.7$ the innermost MDT-chambers are replaced by “**Cathode Strip Chambers (CSCs)**”. At that position the radiation level is already too high for the MDT system. Therefore, a more resistant type of chamber has to be used (see Figure 1.9 left side). The CSCs are based on a multi-wire proportional chamber technique. The spatial resolution of this chamber type can be stated to $60\mu\text{m}$.

Trigger chambers: The muon trigger system is based on two different chamber types. The first covers the barrel region of the muon spectrometer and is called **Resistance Plate Chamber (RPC)**. The RPC chamber system consists of 3 layers. Two of them are located at either sides of the middle MDT chambers. The third is mounted either above or below the outer MDT chambers. **Resistance Plate Chambers** are gaseous, self-quenching parallel plate detectors. The system consists of a pair of electrically transparent plates, separated by small spacers. Signals are induced capacitively on external readout strips. The efficiency of this chamber is higher than 99 % and its space-time resolution can be stated to be $1\text{cm} \times 1\text{ns}$. This chamber provides the muon system with the second coordinate, which cannot be measured by the MDTs.

At the end-cap regions three stations consisting of so called **Thin Gap Chambers (TGC)** are mounted close to the middle MDT station. The TGCs are multi-wire proportional chambers, which provide the muon system with the necessary trigger information in this area. More details about the muon system can be found in [ATM97].

In addition to the desired muon tracks in the system, the ATLAS muon detector has also to deal with a high level of accompanying radiation. This radiation causes serious complications to the detector. It becomes the major criterion concerning the chamber design. This kind of radiation, called “background radiation”, will be discussed in the following chapter.

1.7. Background conditions in the ATLAS muon spectrometer

The background emanating from the calorimeter and the shielding material is one of the main constraints on the muon spectrometer instrumentation layout and operation. It influences parameters such as the rate capability of the muon trigger detectors, the pattern recognition efficiency and the momentum resolution. Furthermore, it can cause severe radiation damage in the detector components. The background can be split conceptionally into two main classes:

1. *Primary background:* primary collision products penetrate into the muon spectrometer. These particles are time-correlated with the primary p-p collision. They originate mainly from decays of light ($\pi, K \rightarrow \mu X$) and heavy ($c, b, t \rightarrow \mu X$) flavors. Furthermore, muons, coming from gauge boson decay ($W, Z \rightarrow \mu X$), contribute as well to this primary background. In addition, also hadronic punch-through induces counts in the detector system.
2. *Radiation background:* Low energy neutrons, originating from primary hadrons, which interact with the forward calorimeter, the shielding, the beam pipe and other machine elements, can be found at a high level in the detector. These neutrons escape the absorber and create via nuclear processes low energy photons. The consequence of this reaction cycle is the production of a “radiation gas”, consisting of low energy photons and neutrons. This radiation field embeds the outer parts of the ATLAS detector (muon chambers). At rapidity $\eta = 2$ ($\theta = 15^\circ$), the photon background produces counting rates in the muon chambers at a level of 100 Hz/cm^2 . In comparison to this value, the expected muon rate is only 10^{-3} Hz/cm^2 . Detailed information about the performance of the ATLAS Muon Spectrometer can be found in [Ale98].

The second part of the background contributes much stronger to the fluence at the position of the muon chambers. In order to reach the muon system, the particles have to cross a certain amount of matter. In Figure 1.10 the contributions of the various ATLAS detector parts to the thickness of the shielding is shown. The right side of Figure 1.10 shows the counting rate of the innermost MDT station as a function of the pseudorapidity. The innermost chamber is by far the most endangered chamber in terms of radiation influences. For this graph a photon sensibility of $8 \cdot 10^{-3}$ was assumed. The MDT neutron sensibility is approximately 10^{-3} . In comparison to these values, the muon detector sensibility concerning charged particles is close to one. Taking these numbers into account, one can see that neutral particles dominate by far the fluence in the region of the muon chambers.

For a more accurate description of the photon and neutron fluences, one has also to investigate the energy dependent behavior of the particles entering the muon system. The fluences depend strongly on the angular position with respect to the beam axis. In order to show this effect, the energy dependent fluence behavior is displayed for three different rapidity ranges in Figure 1.11. In general, one can say that the fluence increases with increasing pseudorapidity. In these figures, a significant dependence of the photon fluence on the neutron influences can be found. The fact that the neutrons influence the photon production can also be seen at the sharp edge of the photon fluence at 10 MeV. Above this energy almost no (n, γ) reactions occur, which could produce photons.

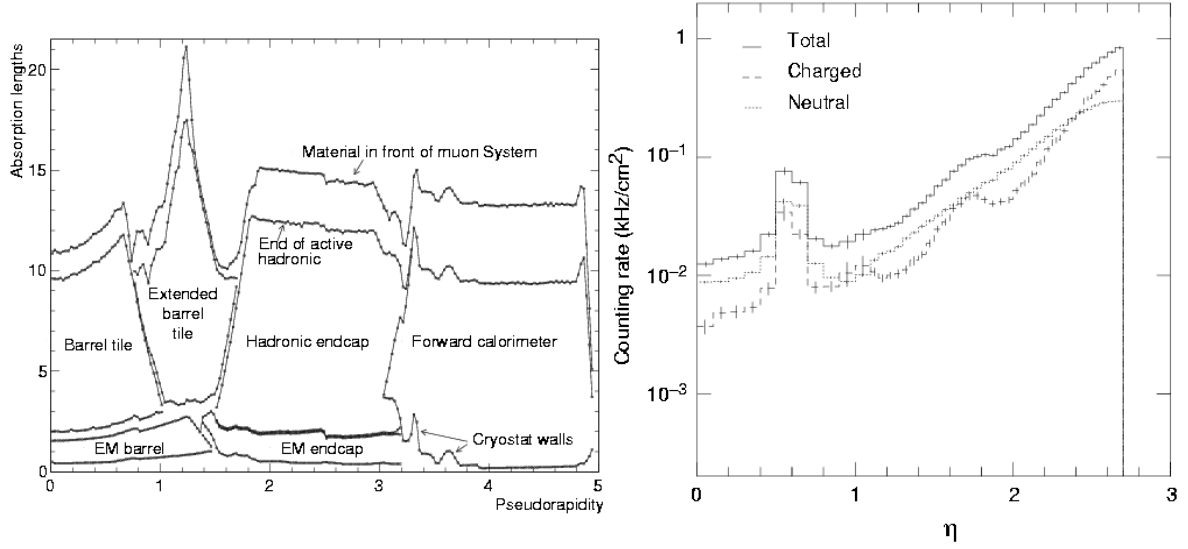


Figure 1.10: Contributions of the various ATLAS detectors to the thickness of the shielding, shown as a function of the pseudorapidity (left). The materials in front of the muon chambers have a strong influence on the detector counting rate. This rate, at nominal luminosity, is shown for the innermost chamber as a function of the pseudorapidity (right).

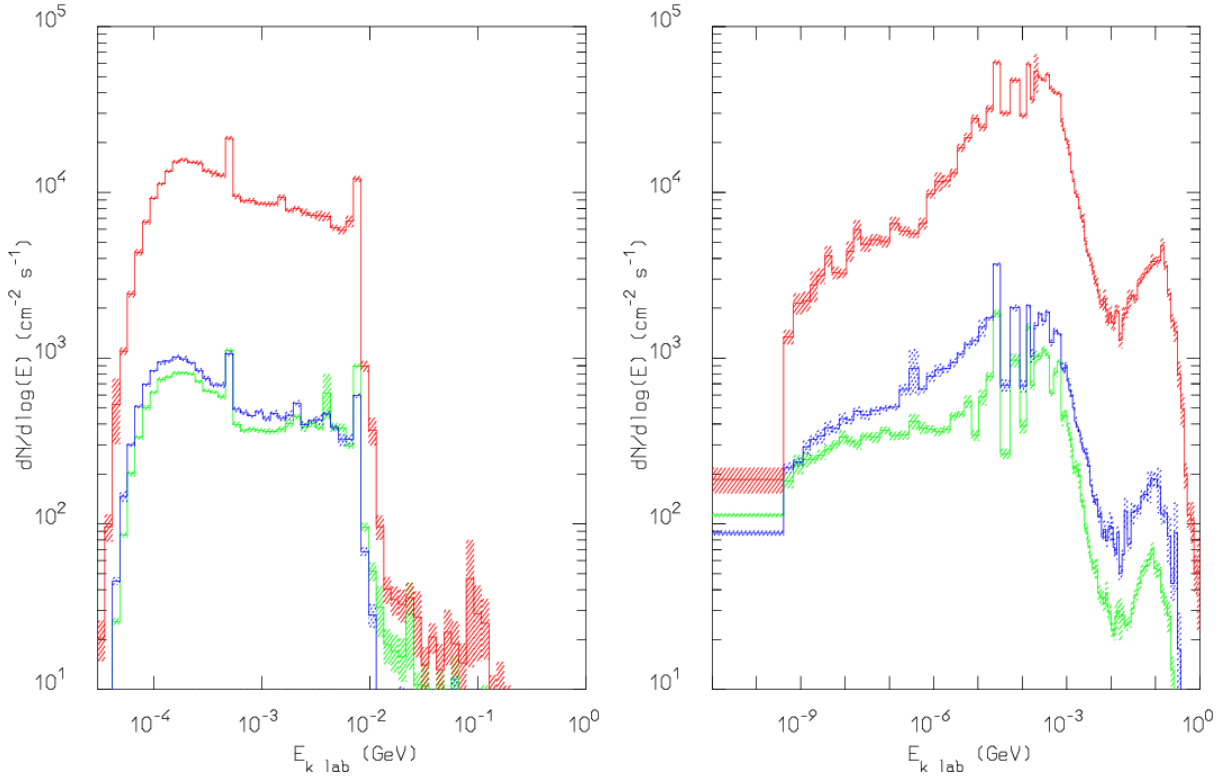


Figure 1.11: The calculated photon (left) and neutron (right) fluence as a function of the photon (neutron) energy. Three different rapidity regions of the innermost muon spectrometer (top curve: $2.3 < \eta < 2.7$, middle curve: $1.4 < \eta < 2.3$ and bottom curve $\eta < 1.4$) are presented.

1.8. Uncertainties of the Background Calculations

All the background fluence calculations were performed with the Monte Carlo particle transport program FLUKA. Details about this program can be found in Chapter 2. The count rates in the MDT's were multiplied with a factor of five in order to cover uncertainties caused by limited knowledge of mainly the following three points:

1. p-p cross sections and multiplicities

The cross section, including secondary particle multiplicity of a proton-proton collision at a center of mass energy of 14 TeV, is of course not exactly known. The portion of this contribution to the total uncertainty factor was evaluated to be 1.3. There is no possibility to lower this value until the LHC is switched on in the year 2005.

2. Muon chamber sensitivity

The muon chamber sensitivity is up to now known with an uncertainty of 50 %. By performing additional investigations concerning the detector sensibility to neutrons and photons, it is expected to lower this uncertainty contribution to a factor of 1.2.

3. Calculations concerning particle production processes in the ATLAS detector material

Limited knowledge of the shower reactions and also of the photon production via neutron induced interactions yields by far the biggest uncertainty. This value was estimated to a factor of 2.5. Photon and neutron fluences in ATLAS, originating from these processes, were calculated with FLUKA.

1.9. Motivation for the FLUKA benchmark studies

In section 1.8 we have shown that the background calculations are estimated to have an uncertainty factor of five due to the superposition of different contributions. One contribution is the limited knowledge of the showering process in the absorber and the ensuing neutron and photon production. This part of the uncertainty factor contributes to the total uncertainty of five with a factor of 2.5.

This value of 2.5 reflects an assessment concerning the capability of FLUKA. The reason for this high number can be found in the fact that no relevant benchmarking of FLUKA concerning such a measurement situation has been done up to now. This kind of benchmark could be obtained in the simulation of a measurement situation, which is characterized by ATLAS comparable photon and neutron radiation conditions. It was considered very important to verify the reliability of FLUKA in this way, as the level of background influences in a critical way many features of the muon spectrometer.

We have emphasized that the background radiation, emanating from the calorimeter and the shielding material, is one of the main constraints of the muon spectrometer

layout and operation. It influences parameters such as momentum resolution, the pattern recognition, radiation damage of the detector components and the rate capability of the muon and trigger detectors.

In particular the following issues will be influenced by the precise knowledge of the background :

- The detailed rate performance of the readout electronics:
While the front-end electronics has been designed to function up to a rate of about 600 kHz, the bandwidth of the readout drivers has not yet been defined. This is a major cost issue.
- The required radiation hardness of the instrumentation:
A large number of commercial items (low and high voltage supplies, CCDs, Hall probes, etc.) will be used. Precise knowledge of the radiation level will allow the correct choice of this instrumentation. This will have considerable importance on the organization and cost of this instrumentation.
- Performance of the trigger system:
The muon trigger rate will contribute the dominant fraction of triggers which may be determined by accidental trigger rates. Knowledge of the background will allow the optimal choice of trigger electronics, trigger algorithms and will permit a better evaluation of the physics potential with low- p_T muons (B-physics).
- Performance of the spectrometer.
The knowledge of the background will allow optimization of the pattern recognition programs and, hence, a better evaluation of the physics potential, particular at high luminosities and beyond design luminosities.

The main program of this thesis is to define and to simulate an ATLAS-comparable shielding situation in order to compare it with measurements performed with this experimental set-up. This benchmarking program will provide us with the necessary information to reduce the uncertainty factor significantly. The aim of these benchmark studies was to reduce the uncertainty factor from 2.5 to 1.2

CHAPTER 2

2. The Monte Carlo Code FLUKA

2.1. General features of FLUKA

FLUKA is a 3D Monte Carlo particle transport program, which simulates particle histories in a user-defined surrounding. In these histories all particles, listed in Table 2.1, can be produced and transported. Except for μ^- and τ^- -neutrinos, interactions with matter are simulated in all details. This introduction deals with the latest version of FLUKA, which was revised at the beginning of 2000.

Table 2.1: Particles simulated in FLUKA

Electron	Positron	Electron neutrino	Electron antineutrino
Neg. muon	Pos. muon	Muon neutrino	Muon antineutrino
Neg. tau	Pos. tau	Tau neutrino	Tau antineutrino
		Photon	
Pos. Hadrons	Neg. Hadrons	Neutral Hadrons	
Proton	Antiproton	Neut. antikaon	Neutron
Pos. antisigma	Neg. antisigma	Neut. antisigma	Lambda
Pos. kaon	Neg. kaon	Neut. antixi	Anti lambda
Pos. omega	Neg. omega	Neut. kaon	Anti neutron
Pos. pion	Neg. pion	Neut. pion	Kaon zero long
Pos. sigma	Neg. sigma	Neut. sigma	Kaon zero short
Pos. xi	Neg. xi	Neut. xi	

In comparison to many other particle transport programs, FLUKA is a fully integrated code which can simulate all transportation and production aspects from PeV to very low particle dependent energies. These energy ranges are stated in Table 2.1.

Table 2.1: Particle dependent energy ranges used in FLUKA

	Transport limits	Limits for primary particles
Charged hadrons	1 keV- 20 TeV	100 keV – 20 TeV
Neutrons	thermal – 20 TeV	thermal – 20 TeV
Anti neutrons	50 MeV – 20 TeV	100 MeV – 20 TeV
Muons	1 keV – 1000 TeV	100 keV – 1000 TeV
Electrons (for high Z)	1 keV – 1000 TeV	150 keV – 1000 TeV
Electrons (for low Z)	1 keV – 1000 TeV	70 keV – 1000 TeV
Photons	1 keV – 1000 TeV	7 keV – 1000 TeV

The simulation procedure in FLUKA is similar to real life experiments. The path of the particles through the geometry is simulated according to the cross sections, which are introduced via the region material compositions. A source particle is started in the existing geometry in a specified region. It propagates unchanged until it crosses a boundary to an adjacent region, it undertakes an interaction with a particle belonging to the regions matter or it decays. In case an inelastic reaction or a decay occurs, new particles can be produced. After the simulation of the path of the primary particle, the histories of the secondary particles are going to be simulated as well. In general, the simulation of a particle stops if the particle falls below an energy threshold or if it escapes the system.

2.1.1. Geometry in FLUKA

FLUKA uses a combinatorial geometry package, which was developed at ORNL (Oak Ridge National Laboratory) for the neutron and γ -ray transport program MORSE [Emm75]. To this package additional geometry features, like infinite cylinders and planes, were added. Complex objects can be defined by using the Boolean operations union, difference and intersection.

A limited repetition capability (lattice capability) is now available which avoids describing repetitive structures in all details. Thus, only one single module has to be defined and can then be reiterated as frequently as needed. In essence, this allows to define geometries, containing up to ten thousand different regions, by using only a small number of region and body definitions.

A geometry debugger detects double- or non-defined regions and provides an ability to plot selected sections of the geometry (derived from the ISPRA PLOTGEOM program).

A program package called FLUKACAD/PIPSICAD, which transforms the input file into an AutoCAD script file, was developed by the author of this thesis [Vin00]. The produced script file can then be used to generate a 3-dimensional drawing of the FLUKA geometry in AutoCAD, including all features of AutoCAD like rendering, dimensioning etc. In addition, double- and non-defined regions can be found and plotted in a reliable and fast way. This package is also able to picture particle tracks, calculated by FLUKA, in three dimensions.

2.1.2. Tracking

An improved model for multiple scattering, derived from Moliere's theory [Mol47, Mol48, Mol55], which is similar to the algorithm used in EGS4 [Nel85], is used in FLUKA. This work has been applied to all charged particles [Fer91a] during the past ten years. This newly developed model reproduces the electromagnetic physics in even greater detail than the EGS4 version. It also takes into account special high-energy effects, very grazing angles, correlations between lateral and longitudinal displacements and back-scattering effects close to boundaries. Furthermore, this model contains a more sophisticated algorithm to tread the boundary problem. This accurate tracking algorithm always calculates the distance to the nearest boundary

which allows an exact transport to region boundaries. With this procedure, material discontinuities can be properly treated in FLUKA. Boundary crossing points are identified precisely even in the presence of very thin layers. In this model, the combined effect of multiple scattering and magnetic fields is also included. In materials of low densities (gases) single scattering can either be requested or even "switched off" in case of simulating interactions with residual gas in accelerator vacuum chambers.

2.1.3. Scoring

In order to score values concerning the conditions of the simulated particle histories, one has to define a kind of "detector" in FLUKA. This tally yields quantities evaluated by the simulation procedure. The most important detectors addresses simulations like:

- Particle fluences and currents;
- Induced track length of particles in defined volumes;
- Number of inelastic reactions in defined volumes;
- Amount of energy depositions in a volume (per primary particle or in average);
- Produced residual nuclei;
- Angle dependent particles production yields.

2.1.4. Biasing

Except for analog Monte Carlo simulations, FLUKA can be run also in a non-analog mode in order to increase statistics in regions rarely reached by particles. In order to perform non-analog calculations, so called "biasing methods" can be used. These methods are listed with name and function below.

- Importance Biasing at Boundaries: according to the importance of the entered region, particles are killed or split.
- Russian Roulette / Splitting for hadronic interactions: the user tunes with this feature the average multiplicity of secondary particles.
- Leading Particle Biasing: only the particle out of two, which has the higher energy, is followed after an electron/positron or photon interaction.
- Weight Windows: region, particle and energy dependent control of the statistical weight at collision points can be applied with this feature.
- Decay Biasing: the decay length of selected particles can be artificially reduced in order to improve statistics of daughter production in desired regions.
- Interaction Length Biasing: the interaction length of selected particles in matter can be artificially reduced in selected materials, forcing more interactions.
- Neutron Non Analog Absorption: the scattering-to-absorption ratio of low energy neutrons can be controlled by the user.
- Neutron Biased Down-scattering: accelerates or slows down neutron moderation in selected regions.

2.2. Different models used in FLUKA

The production and transportation models used are particle and energy dependent. In general one can split the simulation roughly in two parts. The first deals with particles produced in the electromagnetic cascade. The second considers interactions, which produce hadronic particles. Both parts are also responsible for the transport of the primary and secondary particles down to low energies. The electromagnetic cascade is well understood and is mainly based on QED based models. In case of hadronic interactions, different models for different energy ranges have to be used.

2.2.1. Simulation of the hadronic cascade in FLUKA

2.2.1.1. *Dual Parton Model*

The production of secondary particles originating from interactions of hadrons, having an energy higher than 4 GeV, is treated by the Dual Parton Model. A comprehensive review of this model is given in [Cap94]. In this model hadronic high energy collisions are seen as collisions of particles having a partonic structure. A baryon is assumed to consist of a valence quark, a valence diquark and a certain number of so called sea-quark-antiquark pairs. Correspondingly, a meson is assumed to consist of a valence quark, a valence antiquark and also a certain number of sea-quark-antiquark pairs. The interaction of these particles with nucleons can be described via the exchange of Pomerons and Reggeons (quasiparticles). The collision and recombination procedure of the involved particles can be described in the following steps: the hadron and the nucleon split into colored systems (valence and sea quarks). This is followed by an appropriate recombination of the single colored systems with each other. The result of this procedure is the production of color neutral chains of new hadrons. In order to describe inelastic interactions involving nuclei, the Dual Parton Model uses the Gribov-Glauber approximation [Gla55, Gri70, Ber72]. This approximation relates the inelastic hadron nucleus interaction to inelastic scattering processes between the incoming hadron and the individual nucleons. The realization of the DPM is described in FLUKA by an exchange of only one Pomeron or Reggeon. Therefore, the upper laboratory energy limitation for hadrons can be stated at 20 TeV.

The secondary particles propagate through the nuclear matter of the same nucleus and have a well defined chance to interact with the spectator nucleons in the same nucleus. This procedure including the subsequent de-excitation of the nucleus is well known under the name “Generalized Intra Nuclear Cascade Model”. The pertinent energy range is covered mainly by two different models. The first, called NUCRIN, is responsible for the inelastic reactions between 4 and 2.5 GeV. The second model, which covers hadron inelastic interactions below 2.5 GeV, is called PEANUT.

2.2.1.2. *NUCRIN*

NUCRIN is a “Quasi Two Particle Resonance Production and Decay Model” and is generally used in the energy range between 4 and 2.5 GeV (for pions and nucleons between 4 and 3.5 GeV). Within this energy range, resonances, induced by high energy collisions, are produced. The consecutive decay of these resonances is simulated in order to produce secondary particles. The cross sections, necessary for the simulation, are mainly obtained by fits to measurements.

2.2.1.3. *PEANUT*

Within the energy range from 20 MeV to 2.5 GeV (pions and nucleons 3.5 GeV) the **Pre-Equilibrium Approach to NUClear Thermalisation** model is used. This part of FLUKA computes inelastic reactions between the incident particle and the nucleus. Furthermore, the de-excitation phase of the residual nucleus is simulated in this model in some detail.

In PEANUT the nucleus is represented as a sphere. The density of this sphere is described by Woods-Saxon. This applied density approach is assumed to be different for neutrons and protons. The nucleus is radially divided into 14 zones, having different densities. The actual intra-nuclear cascade is followed by exciton pre-equilibrium emission. This part of the model becomes important as soon as all nucleons fall below an energy of 30 MeV.

The particle entering the nucleus is treated via relativistic kinematics. Furthermore, the trajectories of primary and secondary particles inside the nucleus are calculated by a reproduction of nuclear and Coulomb potentials. The nucleus itself is seen as a Fermi sea of nucleons, which are assumed to move independently from each other in a common single-particle potential. This potential can be assumed as a mean field resulting from all two-body interactions among nucleons. Due to this Fermi motion inside the nucleus the secondary particle production threshold is changed. This implies for example that the production threshold for pions induced by a nucleon-nucleon interaction are reduced from 290 MeV (laboratory system energy) to a smaller, nucleus dependent energy. The elastic and inelastic interaction rate of the primary and secondary particles is treated according to the local particle density inside the nucleus. Further quantum mechanics effects, like Pauli blocking or the formation zone concept, are included in the model. The characteristic property of the Intra Nuclear Cascade is that the primary particle and the secondary produced particles can interact with other spectator nucleons of the same nucleus.

The end of this stage is a compound nucleus in an equilibrium state. This nucleus is characterized by its charge, mass number and momentum and carries a certain excitation energy shared by the nucleons.

Evaporation, fragmentation and nuclear de-excitation

The excitation energy of the compound nucleus (*pre-fragment*) can be higher than the separation energy. Thus, nucleons and light fragments can still be emitted. In FLUKA the emission process is described as an evaporation of nucleons, deuterium, tritium, ^3He and α -particles from a hot system.

In case of heavy nuclei a fraction of the excitation energy might also be spent to induce collective deformations, *i.e.* to cause fission processes. In FLUKA the calculation of the fission probability is based on a statistical method [Fer96, Wei37, Boh39]. The masses of the two fragments obey charge and excitation energy dependent distributions [Fer95]. After the fission process both fragments are treated independently, being possibly able to emit further particles themselves.

For light pre-fragments the statistical assumptions and the sequential emission scheme, which underlies classical evaporation models, may become invalid. This can be due to the fact that a moderate excitation energy can already represent a substantial fraction of the total binding energy or that the mass of the “emitted” fragment is comparable to the mass of the pre-fragment. Therefore, in FLUKA the so-called Fermi Break-up model [Fer96, Fer70, Eph67] is applied to pre-fragments with mass numbers below 18. It is assumed that the excited pre-fragment disassembles in one step into two or more fragments. All combinations formed by up to six fragments are considered.

Evaporation processes become energetically impossible when the nuclear excitation energy of a pre-fragment is lower than the energy necessary for nucleon or fragment emission. The residual excitation energy is then dissipated through the emission of photons.

In FLUKA the pre-fragment proceeds through consecutive photon emissions until the ground state of an isotope (*residual nucleus*) is reached [Fer96].

Isotope production

As discussed in [Fer96b], general features concerning the production of residual nuclei are well reproduced by FLUKA. The production cross sections for a residual nucleus having a certain charge and mass number, or the fission cross sections can be considered as examples.

However predictions on cross sections for the production of individual isotopes can be wrong by large factors [Fer96]. Reasons for these uncertainties include the following facts. Slight inaccuracies in excitation energy spectra reaching the evaporation stage can result in substantial shifts among close isotope yields. Furthermore, multi-fragmentation is not considered in the model.

Although comparisons of individual isotope yields with data have already shown promising results [Fer96], care has to be taken in the prediction of isotope yields where no data exist.

2.2.1.4. *Elastic nuclear interaction*

The elastic scattering mechanism of hadrons at nuclei can be very important if the target nucleus is small compared to the direction perpendicular to the hadron track. The scattering is described in terms of the optical model [Wet81]. The optical potential is produced via a real and an imaginary part. The real part can be seen as the sum of a central and a spin-orbit contribution. This part has a Woods-Saxon radial dependence. The imaginary contribution shows rather a periphery-peaked shape. Furthermore, the total elastic cross section is parameterized by fitting to experimental data.

2.2.1.5. *Low-energy neutrons*

Neutron interactions below 19.6 MeV are followed down to user-defined region-dependent energy cut-offs, which can be as low as thermal energies. The model used here resembles the neutron and γ -ray transport program MORSE [Emm75]. However, many improvements concerning the code are incorporated in FLUKA.

In order to simulate the low energy neutron transport including inelastic reactions, cross-section data sets, containing data for more than 130 frequently used elements, materials and isotopes, are used. These cross section sets consist of 72 neutron energy groups (or 37 wider groups), gamma production data and Kerma factors for energy deposition calculations. For many materials data sets correlated with a temperature of 87 Kelvin and approximately 0 Kelvin are available. The difference to the normal sets can be found in a reduced Doppler broadening of the cross sections at thermal energies.

The neutron transport is verified via a standard multi-group transport (P5) with photon and fission neutron production. This model contains detailed kinematics of elastic scattering on hydrogen nuclei. Furthermore, the transport of proton recoils and protons from N(n,p) reaction are considered. Photons, which were emitted after an inelastic reaction or a neutron capture, are not transported in accordance with the multi group treatment. These particles are passed through to the more accurate Electro-Magnetic Fluka (EMF) package, which performs continuous transport in energy and additional secondary electron production.

In general, for nuclei with the exception of hydrogen, kerma factors are employed to calculate energy deposition. In the case of hydrogen the recoiling protons are explicitly generated and transported.

Further details concerning this multi-group procedure and the subsequent gamma production can be found in Chapter 3. In this chapter related problems, concerning the simulation of a neutron experiment, are explained. The energy dependent group limits of the photon and neutron groups and information about cross sections concerning three materials can be found in Appendix A.

2.2.2. Simulation of electromagnetic effects in FLUKA

2.2.2.1. *Transport of charged hadrons and muons*

Beside hadronic effects Fluka has to deal also with electromagnetic influences on hadrons. In order to transport charged hadrons and muons from 1000 TeV down to low energies, FLUKA takes the following effects into account:

Energy loss

The energy loss (dE/dx) is calculated by using Bethe-Bloch theory. The FLUKA model includes a delta-ray production and a transportation mechanism, which includes spin effects and Landau fluctuations. Furthermore, shell and other low-energy corrections are included using methods, introduced by Ziegler [Zie77]. A method, introduced by Sternheimer [Ste84], is used in order to perform the density effect correction for the ionization loss of charged particles.

Multiple Coulomb scattering

An improved model for multiple scattering, derived from Moliere's theory [Mol47, Mol48, Mol55], which is similar to the algorithm used in EGS4 [Nel85], is used in FLUKA. Correlation between lateral and longitudinal displacement are taken into account in the multiple scattering procedure.

Delta rays, pair production and bremsstrahlung

These effects are simulated in FLUKA in great detail. Secondary particles can be treated by applying explicit transport or via an approximate continuous energy loss.

Muon-photo-nuclear effect

Nuclear interactions, induced by charged particles via transferring virtual photons, are applied. In general, they affect all charged hadrons. But this effect is particular relevant for the treatment of muons.

2.2.2.2. *EMF: Electro-Magnetic FLUKA*

In FLUKA a fast-parameterized description of EM-cascades can be used, if only the gross energy deposition mechanisms are of concern.

But also a detailed transport module for electrons, positrons and photons is available. This part of FLUKA, called **Electro-Magnetic FLUKA (EMF)**, is based on the EGS4 code [Nel85]. The original EGS4 code was altered in order to improve the calculation of the electromagnetic cascade. For performing electromagnetic simulations concerning the mentioned particles, one has to produce the necessary material data tables using the program “PEMF”. PEMF is a pre-processor, which provides cross sections by using a method introduced by Sternheimer, Seltzer and Berger [Sel85,

Sel86]. In the following section the main properties of the simulation procedures are explained summarily.

Electrons/positrons

- Special transport algorithm [Fer91a], including complete multiple Coulomb scattering treatment (see hadron and muon transport above) is performed. For this aim a spin relativistic correction (at the level of second Born approximation) and the effect of nucleus finite size are taken into account.
- Concerning dE/dx a separate treatment of electrons and positrons is performed. Differences in bremsstrahlung production has to be regarded in order to calculate this effect [Kim86]. The differential cross sections are derived using the method of Sternheimer, Seltzer and Berger [Sel85, Sel86]. Furthermore, a density correction (Sternheimer density effect) is realized by using this method.
- Detailed angular distribution of the production of bremsstrahlung photons. The Landau-Pomeranchuk-Migdal suppression effect [Lan52, Lan53, Mig56, Mig57] and the Ter-Mikaelyan polarization effect in the soft part of the bremsstrahlung spectrum [Ter54] are taken into consideration.
- Electro-hadron production (only above mass energy of 770 MeV) via virtual photon spectrum and Vector Meson Dominance Model [Möh89] is performed. (The treatment of the latter effect has not been checked with the latest versions).
- Positron annihilation including the subsequent production of two photons is undertaken.
- Delta-ray production via Bhabha and Möller scattering are taken into account.

Photons

- Pair production with actual angular distribution of electrons and positrons is performed.
- Compton effect with respect to atomic bonds is calculated through the use of inelastic Hartree-Fock form factors.
- Photoelectric effect with actual photo-electron angular distribution [Sau31], detailed interaction on six K and L single sub-shells, optional emission of fluorescence photons and approximate treatment of Auger electrons are regarded.
- The Rayleigh effect stayed unchanged to EGS4 [Nel85].
- Photon polarization is regarded for Compton, Rayleigh and photoelectric effects.
- Photo-nuclear interactions are calculated. Particles produced in these interactions are also tracked.

2.3. Applications

In essence, FLUKA has always been a specialized program in order to calculate a multitude of applications in accelerator environments. Besides traditional shielding calculations, FLUKA is now used in many domains. Examples for applications are target design and optimization calculations, predictions of activation in irradiated facilities, simulations concerning radiation damage, isotope transmutation and calculations concerning accelerator component design parameters.

The capability to deal with the low-energy neutron component of the cascade extended the field of interest. The fact that FLUKA covers the whole particle and energy spectrum increases the application range of this program tremendously.

FLUKA is now successfully employed in many domains as background studies for underground detectors, cosmic ray physics, detector design for radiation protection, shielding of synchrotron radiation hutches, evaluation of organ dose in a phantom due to external radiation, calculation of dose received by aircraft crews, as well as, for simulations concerning high energy physics, neutrino physics, electron and proton radiotherapy, nuclear transmutation, tritium production at electron accelerators, energy amplifiers, maze design for medical accelerators, testing of physical models, etc.

2.4. History of FLUKA

The Monte Carlo program FLUKA looks back to a history of almost 40 years. In order to classify this period, one has to focus on three different generations of development.

First generation (the CERN SPS Project, 1962-1978)

Early versions of hadron cascade codes which finally became FLUKA, have existed since 1964 [Ran64,Gei65,Ran72]. The code was originally non-analog and used as a tool for designing shielding of high energy proton accelerators. The need to write the fully analog FLUKA (FLUktuierende KAskade) arose from the idea to apply the code to evaluate the performances of NaI crystals as hadron calorimeters [Ran70]. Various versions of the original program were used at CERN until about 1980 [Sch74]. The main application field concerned radiation studies connected with a 300 GeV Project [Goe71], which was then later realized as the 450 GeV SPS accelerator.

Second generation (development of new hadron generators, 1978-1989)

A complete re-design of the code was started in the early 80s, as a collaboration between CERN, Helsinki University of Technology and Leipzig University [Möh81, Aar84, Aar84a, Ran85b]. Along with a new modular structure, many changes were introduced in the code physics. The most important implementations in the code were the Dual Parton Model event generator [Ran83, Ran83a, Ran85, Ran85a], which includes a quasi two-particle production model (code HADRIN) for hadron-hadron collisions [Hän79,Hän84,Hän86]. Furthermore, the code NUCRIN, dealing with

hadron-nucleus collisions [Hän84a,Hän86a], was introduced to the program. FLUKA was also linked on-line with the EGS4 code [Nel85] for the treatment of EM showers originated from π^0 decays. Also a transport algorithm in magnetic fields for hadrons was introduced (but not yet for electrons).

Third generation (the modern multi-particle code, 1988 to present)

The second phase of the FLUKA development was completed in 1987 when the new version was frozen [Aar86,Aar87]. At about that time the Milan section of INFN joined in the collaboration, starting a period of strong development. As a result of the work carried out in the last twelve years, the accuracy of FLUKA has been dramatically improved and its field of application has been extended well beyond the traditional radiation protection domain. The range of possible applications of FLUKA has been expanded to cover in addition to the original shielding and beam heating studies, also calorimetry, prediction of radiation damage, dosimetry, detector design, cosmic ray studies, waste transmutation and many other applications.

The original EGS4 implementation in FLUKA was progressively improved, updated and increasingly integrated with the hadronic and the muon components of FLUKA. The end product appears as a very improved code to the original EGS4 and is now called Electro-Magnetic-Fluka (EMF). Despite the fact that 90% of this code is new and original, most of the structure (and a few remaining routines) are similar to the original EGS4 implementation.

Details about the revision history of FLUKA can be found in the Appendix B.

2.5. ATLAS Background calculations with FLUKA

The particle fluences in the ATLAS detector, coming mainly into being via shower processes, which are induced by secondary particles of the p-p collisions, were calculated with FLUKA. The minimum-bias events, which are used as a source in FLUKA were generated by using the code DTUJET93 [Bop94]. The final simulations concerning the background issue were performed in the year 1998. The benchmarking simulations presented in this thesis were mainly performed with the version of the year 1999. There are no major changes between the two versions which could influence the result significantly. Hence, the result of the benchmarking procedure can be related to the background simulation results. In these calculations the whole EM cascade (e^- , e^+ and γ) was calculated down to an energy of 30 keV. The neutrons were followed to a level of thermal energies. The results concerning the simulated fluence distributions in the ATLAS hall are shown in Figure 2.1 (photons) and Figure 2.2 (neutrons) respectively. These pictures can be also found in [ATM97].

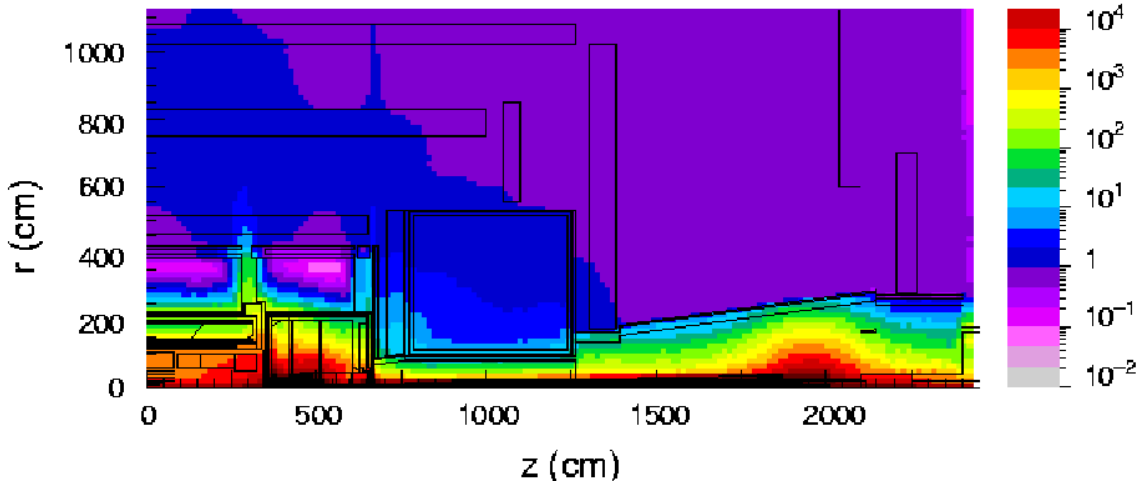


Figure 2.1: photon fluence in the ATLAS hall (kHz/cm^2) at a luminosity of 10^{34} .

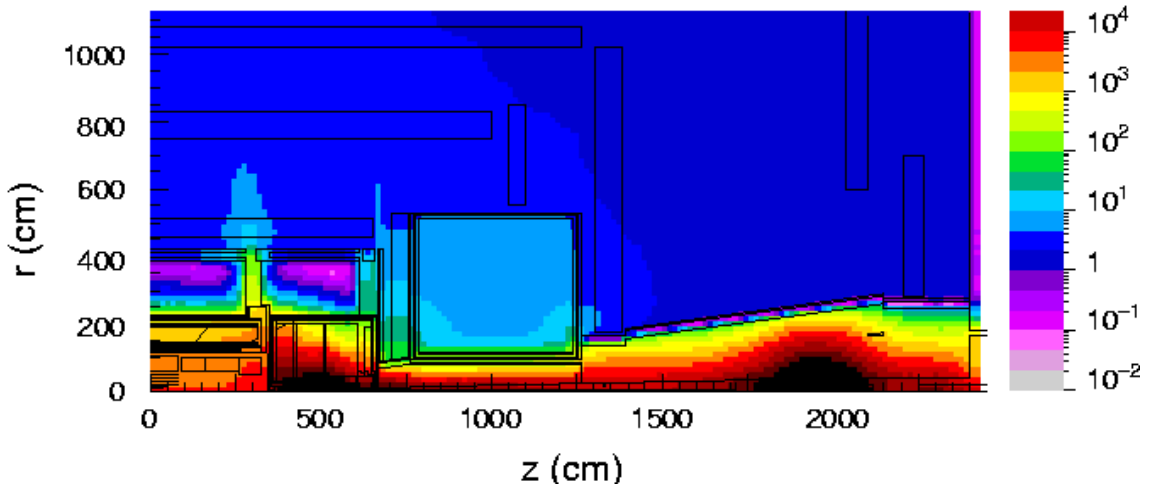


Figure 2.2: neutron fluence in the ATLAS hall (kHz/cm^2) at a luminosity of 10^{34} .

In order to obtain a better orientation in this picture one should also consult Figure 1.9. This Figure is equivalent in terms of the construction because further details about the detector components are shown. The calculated photon and neutron fluences as a function of the location show the following characteristics:

1. Close to the beam axis, the radiation field is extremely high. Especially at the position of the forward calorimeter (between $z \sim 4$ m to $z \sim 6.5$ m), the radiation level increases due to interactions of p-p secondaries with the detector material. A second point along the beam axis, having an extreme high radiation level, can be found at $z \sim 20$ m. Also here, interactions of secondary particles, having a very high energy, with the shielding material can be found.
2. The lateral Electromagnetic and the Hadronic Calorimeter have to operate in a radiation field of up to several thousand particles per cm^2 . In these regions the photon contribution is similar to the neutron contribution.
3. Except for several shielding gaps, a strong decrease of the fluence as a function of the distance to the beam axis can be observed. Two very significant gaps can be found at a position of $z \sim 3$ m and 6.5 m respectively. Around these gaps, a increased level of radiation can be observed. The fluence contributions, which are mainly characterized by these gaps, influence the radiation in positions up to the outer muon layer ($r = 10$ m).
4. The first muon layer, located at $z \sim 7$ m (parallel to r), is the most irradiated one. The neutron fluence in this chamber is up to a factor of 10 higher than the comparable photon fluence. The neutron fluence ranges in this chamber from around 100 kHz/cm^2 down to a level of a few kHz/cm^2 . The contributing photon fluence can be found in the most ranges of this chamber within a few kHz/cm^2 .
5. Muon chambers, which are located further away from the beam axes are in general less strong influenced by the background radiation.
6. At the outer part of the hall construction a neutron fluence around 10 times higher than the correlating photon fluence can be found. These fluences are correlated to each other by neutron induced gamma reactions. In general, at positions with low neutron fluences also a corresponding low photon fluence can be found.

Further details concerning fluence contributions in the range of the muon chambers can be found in Chapter 1.7.

CHAPTER 3

3. Evaluation of particle-dependent BGO response

3.1. Introduction

In order to benchmark FLUKA, two main groups of experimental set-ups were chosen as the focus of this thesis.

The first kind deals with simple geometries and well-defined radioactive sources, which were used to irradiate a BGO scintillator. In these experiments, the energy deposition, which is induced by photons and neutrons in the crystal, is simulated in order to be compared with appropriate measurement results. This kind of comparison provides us with a first-order benchmark concerning the energy deposition induced by different particles with variable energies.

In the beginning of the chapter, the simulated BGO scintillator is described in detail. This section is followed by a general description of the simulation procedure, which deals with the experimental set-up of the low-energy photon measurements. Furthermore, the procedure to obtain simulation results, comparable with the measured results, is discussed. The subsequent subchapter presents the simulation results and the comparison with the measurements.

The second part of this chapter deals with the simulation of the neutron measurements. These measurements were carried out with an Am-Be source which emits, besides photons of an energy of 4.439 MeV, a continuous neutron spectrum. The first part of this section explains the measurements including their reproduction in FLUKA. In the next subchapter, the simulation results, their comparison with the measurements and a discussion concerning underlying physical and simulation effects are exposed.

The second kind of benchmark simulations deals with experiments performed in the H6 area at CERN. During these measurements a large cast iron absorber was irradiated by a hadron beam. Further details concerning this topic can be found in Chapter 4.

3.2. Description of the simulated measurement device

The main detector, which was used during all measurements, is called “38 A 38 – BGO – X” and is a BGO crystal scintillator. The most important parts of this detector are:

- Crystal: $\text{Bi}_4\text{Ge}_3\text{O}_{12}$
- Photo-multiplier: Hamamatsu R2066
- Voltage divider

The crystal itself can be seen as the heart of the measurement device. Its chemical formula is $\text{Bi}_4\text{Ge}_3\text{O}_{12}$ and the density can be quoted as 7.13 g/cm^3 . Because of its high density and the high atomic number of Bi, the BGO is well suited to detect photons. This leads, therefore, to a high gamma reaction efficiency of the device. The photo-multiplier used is a Hamamatsu R2066. This photo-multiplier consists of a bi-alkali photo-cathode followed by 10 dynodes, which amplify the photo-electric current produced by the incoming particles. The quantum efficiency at 420 nm of this multiplier can be quoted as 22 %. For connecting the photo-multiplier to the voltage divider 12 metallic bins are installed. These bins, imbedded in a polyethylene base, are arranged at a circle with a radius of 1.7 cm around the BGO symmetry axis.

The complete BGO scintillator was implemented in the simulation and is shown in Figure 3.1.

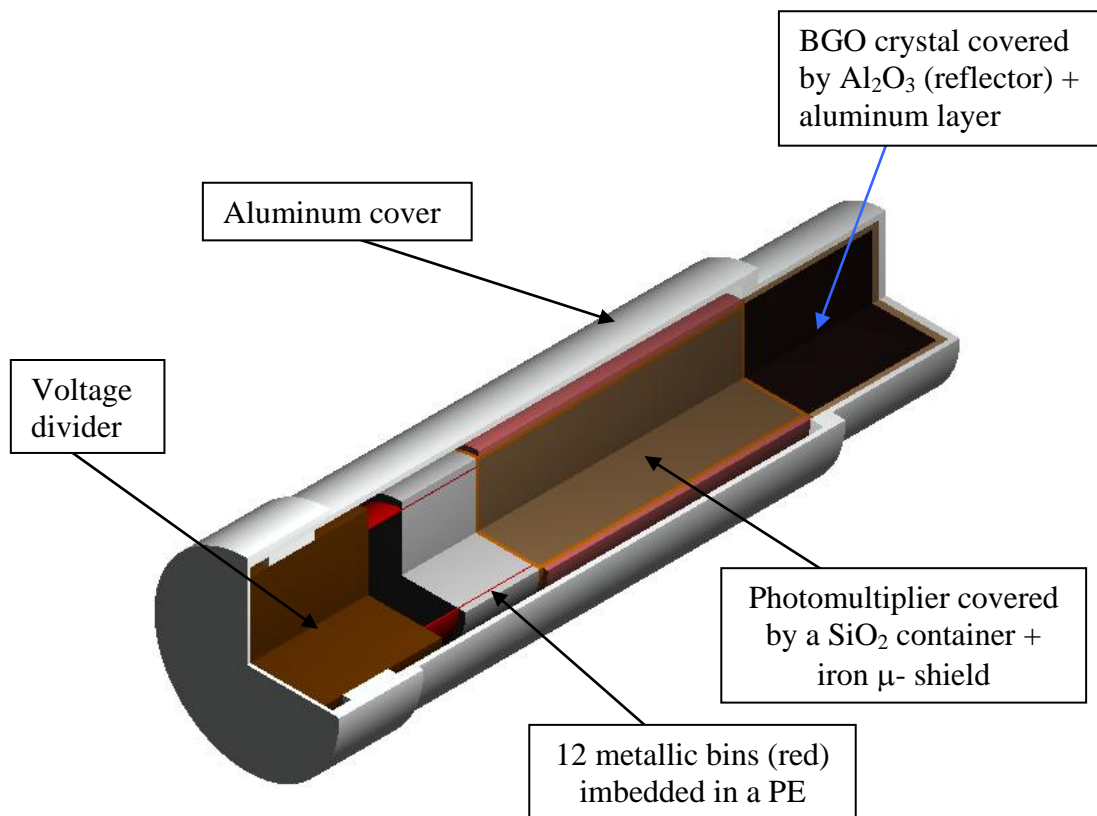


Figure 3.1: Cross section through the simulated BGO scintillator (crystal dimension: 3.8 cm in height and diameter)

The simulation of the BGO was done very accurately. The fact that the surroundings of the crystal have an influence on the calculated fluences entering the crystal, made this accuracy necessary. The BGO crystal, which is a cylinder with both a height and a diameter of 3.8 cm, is surrounded by an Al_2O_3 reflector. This reflector increases the amount of captured scintillation photons, which enhances the energy resolution of the detector. This reflector was implemented in the simulation as an Al_2O_3 cylinder, surrounding the BGO crystal. The crystal itself is connected to the photo-multiplier, which is coated by a glass container (SiO_2). The glass container is surrounded by an iron cover which keeps the internal structure of the photo-multiplier (PM) free of external electromagnetic fields. The real positions of the dynodes inside the photo-multiplier are not known. Therefore, the following approximation concerning the simulation geometry of the PM was performed. The region inside the glass container (photo multiplier) was simulated as low density material, which has a mass equal to the mass of the dynodes inside the PM. The connection between PM and voltage divider was implemented in the simulation via a hollow iron cylinder with the mass of the 12 connection bins. The position of the cylinder coincides with the circle arranged by the real connection points. This simulated bin structure (cylinder) is partially embedded in a polyethylene base. The voltage divider itself was implemented as a mixture of iron and polyethylene. The whole device structure is surrounded by an aluminum cover.

3.3. BGO detector response to different gamma sources

3.3.1. Experimental setup

In order to investigate the photon response of the used BGO, measurements with three different radioactive sources were performed. The sources with their energies and activities are listed in Table 3.1.

Table 3.1: Used sources during the gamma response measurements:

Source	Energy [keV]	Intensity [γ/s]
Cs-137	662	34006 ± 228
Mn-54	854	2294 ± 15
Co-60	$1173.2 : 1332.5 = 1 : 1$	$2 \times (29160 \pm 195)$

In Figure 3.2, the simulation geometry of the experimental set-up is shown. For all measurements, three different angles between the symmetry axis of the BGO and the position of the source were chosen. The angles, measured from the outer mid-point of the cylindrical crystal cover (see arrows in Figure 3.2) were 0, 45 and 90 degree. In the simulation picture, the different source locations are shown as spheres.

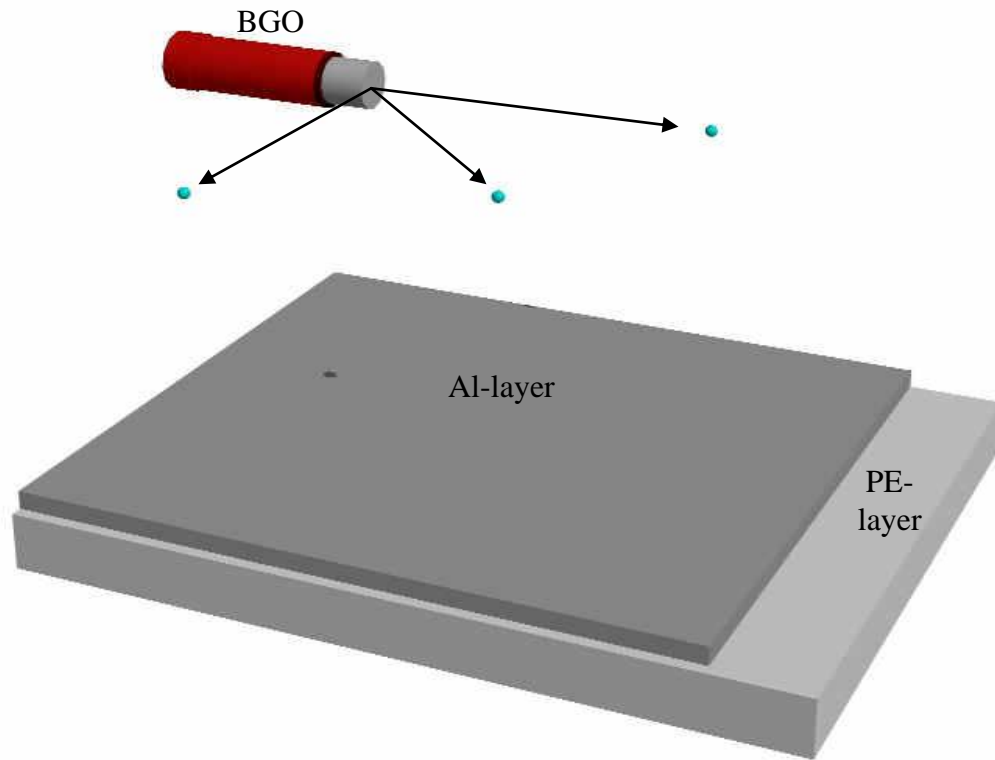


Figure 3.2: Simulated measurement construction: The three small spheres indicate the three different source positions of the source.

The distances between the outer mid-point of the cylindrical crystal cover and the source were chosen in relation to the strength of the source used. In Table 3.2, the different distances are stated:

Table 3.2: Distances between BGO cover and gamma sources

Source	Distance
Cs-137	(29.5 ± 0.1) cm
Co-60	(29.5 ± 0.1) cm
Mn-54	(10.0 ± 0.1) cm

In order to take the back scattered particles (induced by the primary photons) correctly into account, the BGO was installed within a well-defined location. The detector was mounted 24.3 cm (distance between BGO axis and table) above a table, which consists of a 1.6 cm thick aluminum layer located on a 5 cm thick polyethylene layer (see Figure 3.2). The walls surrounding the construction and the support on which the BGO was mounted were neglected in the simulations. The procedure of neglecting these parts is justified because the main part of the back scattered particles originate from the two layers below the BGO.

3.3.2. Simulation procedure to obtain measurement comparable results

In order to obtain simulation results, which are comparable to the BGO measurements, the simulation procedure has to be performed in two steps:

- 1) Simulation of the single particle histories in the geometry used. The energy deposition induced in the BGO crystal is stored in a histogram.
- 2) In order to compare the calculated result with the real BGO measurement, the obtained energy deposition spectrum has to be converted into a spectrum with realistic energy resolution.

3.3.2.1. Simulation of the particle histories in the BGO crystal

For reproducing the measurement, an irradiation of the BGO, induced by a 4π photon point source with appropriate energy, was simulated. In this run, energy depositions generated by each primary particle are calculated by using the FLUKA input card "DETECT" [Fas99]. The result of this procedure is an energy dependent number of counts, induced in the BGO crystal. To use the DETECT card, the user has to state the minimal and maximal countable energy deposition ($EDEP_{min}$, $EDEP_{max}$) in the simulated BGO crystal. The calculated spectrum consists of 1024 energy dependent channels. The minimal and the maximal energy (E_{min} , E_{max}) of the single channels depend on $EDEP_{min}$ and $EDEP_{max}$ as well as on the channel number (CHNR). These values are calculated via the Equations 3.1 and 3.2.

$$E_{min} = EDEP_{min} + \frac{EDEP_{max} - EDEP_{min}}{1024} \cdot (CHNR - 1) \quad \text{Equation 3.1}$$

$$E_{max} = EDEP_{min} + \frac{EDEP_{max} - EDEP_{min}}{1024} \cdot CHNR \quad \text{Equation 3.2}$$

All induced energy depositions in the BGO crystal, having an energy between these two energy thresholds, are put in one of the 1024 channels. No count is added to the histogram if the simulated particle does not produce an energy deposition in the crystal or the amount of deposited energy is outside the range, which is given by $EDEP_{min}$ and $EDEP_{max}$. The result of this procedure shows a spectrum produced in a BGO with an energy resolution, which is independent of the deposited energy. The resolution of this procedure is only determined by the actual energy bin width of the 1024 channels. In order to achieve a real BGO energy deposition spectrum, further manipulations with the obtained result have to be done.

3.3.2.2. Convolution of the BGO energy deposition spectrum with a resolution function

The energy deposition spectrum of the BGO corresponds to a measured spectrum having constant energy resolution. To adapt the result to the real BGO, including electronic instrumentation, a proper convolution of the single energy dependent entries has to be done. A simple example can be found in Figure 3.3, where the BGO is irradiated by an Co-60 source.

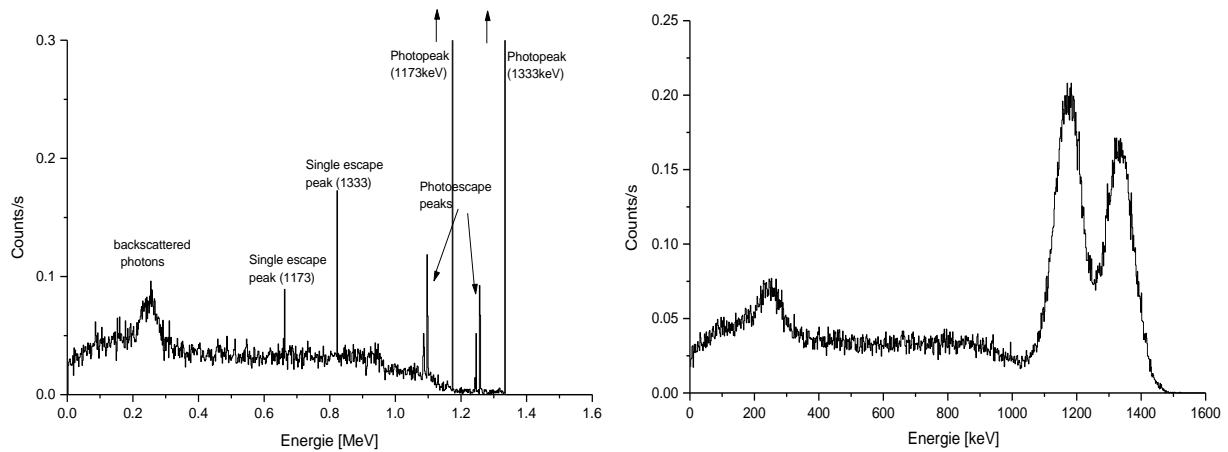


Figure 3.3: BGO energy deposition spectrum induced by a Co source before (left) and after conversion (right). Entries in 1024 (1.76 keV width) channels were convoluted with the proper resolution.

Procedure of the conversion

In a real BGO detector, a specified energy deposition, induced by a particle with a certain energy, is measured with a detector-dependent energy resolution. The measured spectrum around an obtained mean value shows a Poisson distribution. The reason for this behavior can be found in detector-dependent fluctuations of the measurement procedure of energy depositions. The standard variation of the measured spectrum, induced by an energy deposition, is energy dependent and can be obtained via a measurement of the energy deposition caused by a mono-energetic photon source. To adapt the calculated energy deposition to the real spectrum, a calibration measurement with a Cs-137 source was performed. The measured energy including the spectrum resolution, concerning the used BGO, is shown in Table 3.3.

Table 3.3: parameters of the induced BGO spectrum, received by using a Cs-137 source.

Energy	σ around the energy mean value
662keV	36.15 keV

In order to obtain the energy resolution for all energies, this measurement result has to be extrapolated via the following procedure. The Poisson statistic applies the well-known counting behavior for the detector:

$$\sqrt{\text{counts}} = \sigma \quad \text{Equation 3.3}$$

counts means the number of counted scintillation events produced during the measurement of “one” energy deposition. The mean value of these counts corresponds to a certain energy deposition. With knowledge of the amount of the energy deposition (662 keV), plus the measured standard variation (36.15 keV) and the fact that this counting procedure follows the Poisson statistic, the average minimal energy unit (E_{\min}) to produce countable scintillation events can be calculated.

$$\sqrt{\frac{\bar{E}}{E_{\min}}} = \frac{\sigma(E)}{E_{\min}} \quad \text{Equation 3.4}$$

$\sigma(E)$... standard variation in energy units

E ... amount of energy deposition

The Equations 3.3 and 3.4 reflect exactly the same situation. The average value of the deposited energy divided through E_{\min} yields the average number of counts (Equation 3.3), which are induced by the energy depositions in the detector. Therefore, the average minimal energy unit of the detection process in the BGO is: 1.974 keV. This value can be seen as the effectively minimal detectable energy in the BGO arrangement. With the information of E_{\min} one can calculate the σ for each energy by using Equation 3.5.

$$\sigma(E) = \sqrt{E_{\min}} \cdot \sqrt{E} = 1.405 \cdot \sqrt{E(\text{keV})} \quad \text{Equation 3.5}$$

The result, $\sigma(E)$, is obtained in keV. For example: a Cs-137 photon (=662 keV) produces an average of 335.35 scintillation processes, which are detected by the electronics in the BGO. The appropriate counting σ of this energy is 18.3, which corresponds to an energy of 36.15 keV (=18.3·1.974 keV).

To convert the energy deposition spectrum into a real BGO spectrum the mean energy of each channel and the proper sigma is calculated. The events, which are stored in each channel, will be Gaussian smeared with the calculated sigma around the actual channel. Therefore, the sharp energy deposition peaks get a real detector dependent shape. The result of this procedure can be seen in Figure 3.3.

3.3.3. Procedure to obtain particle currents entering the BGO

In order to calculate the efficiency of the detector, the number of particles entering the BGO crystal has to be known. For the FLUKA calculation of this value the simulation detector “USRBDX” [Fas99] was used. This detector is a boundary crossing tally, which counts all particles crossing a well-defined boundary. USRBDX was used in the “one-way current scoring” mode between the reflector and the BGO crystal. That means that all particles which enter the BGO crystal coming from the reflector are counted in this detector.

For calculating an efficiency of the detector, the γ current, which is taken into account, has to be clearly specified. In this thesis, all photons flying from the source into direction BGO crystal are seen as a part of the γ current, which is used to calculate this value. Particles, hitting only the cover or other parts of the BGO, are not taken into consideration. Especially for the photo peak efficiency calculations, these grazing particles have no chance at all to add a counting contribution to the result. Therefore, these γ 's are not considered to be part of the BGO crystal-hitting current.

The computation of the number of γ particles having a flight direction source-BGO was done as follows:

For all different angle and distance situations, all materials, except the external void, were set to vacuum. Analog runs with a very high number of primary particles were performed. The effect of this procedure is that all γ 's with flight direction source-BGO crystal reach the crystal region without being scattered or absorbed. A counting of the particles, which enter the BGO crystal, produces therefore, the desired current.

3.3.4. Simulation results

3.3.4.1. Energy deposition in the BGO

In Figure 3.4, three energy deposition graphs induced by the three simulated sources are shown. In all results, the irradiation angle between source and BGO cylinder axis is 0 degree. For each scenario, the photo peaks and the photo escape peaks can be observed very well. The Co-60 source emits photons at two different energies. Therefore, two photo peaks with the appropriate photo escape peaks can be found. A photo peak count is observed if the whole energy of the entering gamma is absorbed in the crystal. The photo escape peaks come into being in the following way: a γ particle performs a photoeffect reaction in the crystal. The scattered electron, mainly one of the K- or L- electrons, is replaced by an electron originating from an outer and therefore, less strongly bound shell in the atom. The result of this replacement is a X-ray emission. The energy of this emitted photon corresponds to the energy difference between the two atomic orbits. The photo escape peaks are produced if the X-ray photons escape the crystal without getting re-absorbed. The energy gaps between the photo peak and the photo escape peak correspond exactly to the energy of the produced X-ray.

The next lower energy points in the spectra are the Compton edges. These edges can be explained as follows: the energy, which is transferred to the crystal by a Compton scattering process is described by Equation 3.6.

$$E = E' \cdot \frac{1}{1 + \varepsilon \cdot (1 - \cos \vartheta)} \quad \text{Equation 3.6}$$

- E ... Energy of the scattered photon
- E' ... Energy of the incoming photon
- ε ... Incoming photon energy divided by electron mass energy
- ϑ ... angle between incoming and scattered photon

In case a Compton process occurs in the crystal, the back scattered photon either escapes or deposits its energy completely or partly inside the crystal. If the back scattering angle of the photon is 180 degree, the maximal transferable energy is deposited in the crystal. The energy deposition corresponds with the difference between the energy of the primary gamma and the minimum energy of the back scattered photon ($\vartheta=180^\circ$). A Compton scattering process, which deposits an energy higher than the described upper threshold, is impossible. Therefore, the cross section for an energy transfer, via a Compton scattering process, decreases to 0 at this energy. This implies an edge in the spectrum at the corresponding energy. Sharp edges at the appropriate energies are clearly visible for the Cs-137 and the Mn-54 situation at 477 and 638 keV, respectively.

The Compton edges in the simulations of the Co-60 source is less visible than in the lower energy scenarios. The reason for this can be explained with the following arguments:

- The probability to receive a 180° back-scattered photon decreases with increasing energy of the primary photon.
- The probability of observing a pair production (see below) increases with increasing energy. The appearance of this effect reduces the number of Compton scattering processes.

In the case of Co-60, two primary energies occur. Both energies are higher than 1022 keV. Therefore, another type of reaction, the (e^+e^-) pair production, can be observed. This reaction produces two additional peaks in the spectrum. These peaks can be found at energies of *photo peak energy-511 keV* (single-escape peak) and at energies of *photo peak energy-1022 keV* (double-escape peak). The reason of this behavior can be explained with the annihilation of the produced positron in the crystal. The result of this process is a production of two gamma particles, having an energy of 511 keV. In case both photons are re-absorbed inside the crystal, the energy deposition is counted in the photo peak. If one or two of these photons escape the crystal, the total deposited energy is counted in the single- (photo peak–511 keV) and the double-escape peak (photo peak–1022 keV), respectively. In the simulation for the Co-60 source only the single-escape peaks are visible, because the double-escape peaks are superimposed of energy depositions induced by the Compton effect reactions.

In all simulations, a second kind of Compton scattering effect can be observed. The Compton scattering occurs not in the crystal but in the surrounding of the set-up. The primary photons produce in the surrounding, which consists in the simulation mainly of an aluminum and a polyethylene plate, back-scattered photons. These photons are partly seen in the crystal. The energy ranges of these gammas can be calculated by applying the geometrical possible back scattering angle of the photons (θ) to Equation 3.6. In the case of the Mn-54 measurement, the distance between source and crystal was reduced to 10 cm. This implies a smaller back-scattering angle range than in case of a BGO-source distance of 29.5 cm. Therefore, the “back-scattering hill” of the Mn-54 situation extends over a smaller energy interval compared to the correspondent hills of Co and Cs. The theoretical possible angles and energies of the back scattered photons hitting the BGO crystal can be found in Table 3.4.

Table 3.4: Angle and energy of back-scattered photons, originating from the measurement surroundings.

Source	Primary energy	Minimal angle	Maximum energy of back-scattered γ 's	Energy of 180° back-scattered γ 's
Cs-137	662 keV	110°	242 keV	184 keV
Mn-54	835 keV	147°	209 keV	196 keV
Co-60	1172 keV	110°	287 keV	210 keV
Co-60	1333 keV	110°	296 keV	214 keV

The main part of the back-scattered γ 's comes from the plates. However, the Compton scattered photons produced in the BGO detector cover have no restriction in the possible scattering angle. These secondary photons can produce interactions in the BGO crystal, which can also deposit energies within the range between the Compton edge and photo-peak energy.

The fact that the simulation was performed in a fully analog run makes it easy to compute the statistical uncertainties of the single histogram entries. The formula for evaluating the statistical uncertainty of the single channels can be found in Equation 3.7. This equations relates the value of the histogram (counts/(s·MeV)) with the entries in the single bins, obtained in the analog simulation run. The appropriate values to calculate the uncertainties (σ) of the numbers of entries per bin are listed in Table 3.5

$$\sigma(\%) = 100 \cdot \sqrt{\frac{SS}{A \cdot EBIN \cdot PP}} = 100 \cdot \sqrt{\frac{1}{N}} \quad \text{Equation 3.7}$$

With:

SS	Source strength = number of emitted particles per second
A	Value in the histogram (= counts/(s·MeV))
EBIN	Width of the single energy bins in MeV
PP	Number of primary particles used for this analog simulation
N	Number of counts per bin obtained in the analog simulation

Table 3.5: Values for the calculation of the statistical uncertainties

	Cs-137	Mn-54	Co-60
SS	34006	2294	58320
PP	$1.25 \cdot 10^8$	$1.25 \cdot 10^8$	$1.25 \cdot 10^8$
EBIN	$1.758 \cdot 10^{-3}$	$1.758 \cdot 10^{-3}$	$1.758 \cdot 10^{-3}$

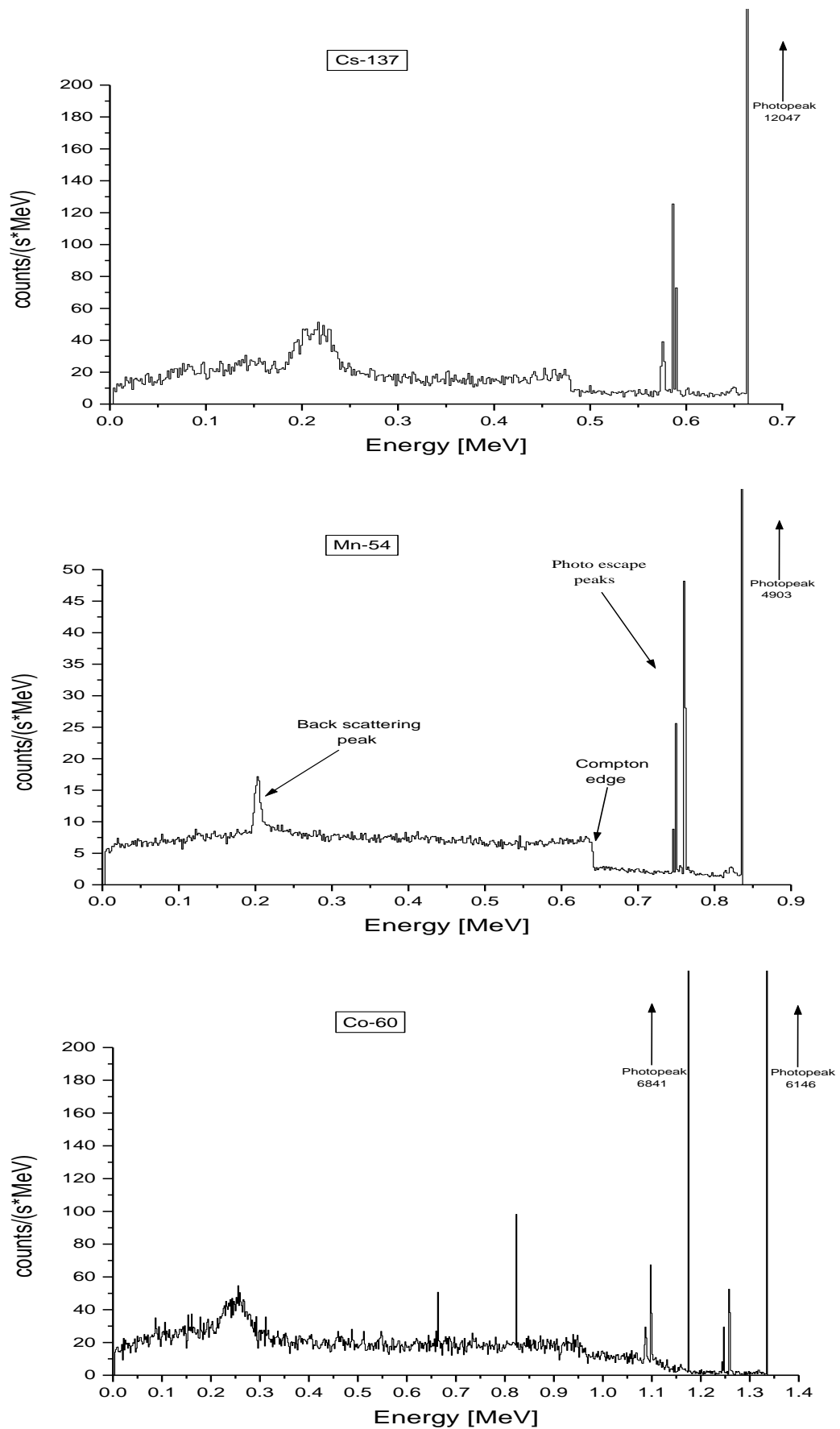


Figure 3.4: BGO energy deposition spectra for Cs-137, Mn-54 and Co-60. The irradiation angle between source and BGO axis is 0° in all 3 cases.

The energy deposition rates, including the efficiency concerning energy depositions higher than 400keV and the photo peak efficiency concerning the single primary energies, are listed for all simulated situations in Table 3.6 and 3.7. In order to avoid a contribution of the back-scattered photons to the final efficiency results, the lower threshold of the compared energy range was set to 400 keV. None of the used sources can produce Compton photons originating from the aluminum or polyethylene plates, which have energies higher than 400 keV. Therefore, counts with energies above this threshold come necessarily directly from the source. The calculation of the efficiency in general and the calculation of the uncertainty, induced by the statistical uncertainties of counting rates and currents entering the BGO, can be obtained with Equation 3.8 and 3.9. In order to provide calculation results concerning the efficiency of the used BGO, the uncertainty induced by inaccuracies of the measured activities is not taken into account in this subchapter. These uncertainties and other measurement inaccuracies are investigated in the next chapter.

$$Eff = \frac{CR}{current} \cdot 100 \quad \text{Equation 3.8}$$

$$\Delta Eff = \sqrt{\left(\left(\frac{dEff}{dcurrent} \cdot \Delta current \right)^2 + \left(\frac{dEff}{dCR} \cdot \Delta CR \right)^2 \right)} \quad \text{Equation 3.9}$$

With:

<i>Eff</i>	...	Efficiency in %
<i>CR</i>	...	Counting rate
<i>current</i>	...	Number of photons entering the BGO crystal
ΔEff	...	Statistical uncertainty of efficiency
ΔCR	...	Statistical uncertainty of counting rate
$\Delta current$...	Statistical uncertainty of the current, entering the BGO crystal

Table 3.6: Simulated counting rate and efficiency of the BGO crystal regarding energy depositions higher than 400 keV.

Element	Energy	Angle	Counting rate > 400keV	Error	Current in BGO	Error	Efficiency > 400keV	Error
	keV	degree	counts/s	%	γ /s	%	%	%
Cs-137	662	0	24.3	0.3	34.30	0.6	70.8	0.7
	662	45	27.1	0.3	50.52	0.5	53.6	0.6
	662	90	30.4	0.3	47.42	0.5	64.1	0.6
Mn-54	835	0	10.84	0.1	18.67	0.2	58.1	0.2
	835	45	11.83	0.1	23.45	0.2	50.4	0.2
	835	90	16.20	0.1	28.74	0.2	56.4	0.2
Co-60	1173 1333	0	36.5	0.4	58.82	0.6	62.1	0.7
	1173 1333	45	40.0	0.3	86.64	0.5	46.2	0.6
	1173 1333	90	45.2	0.3	81.36	0.5	55.6	0.6

Table 3.7: Simulated photo-peak rate and efficiency of the BGO crystal.

Element	Energy	Angle	Photopeak rate	Error	Current in BGO	Error	Photopeak efficiency	Error
	keV	degree	counts/s	%	γ /s	%	%	%
Cs-137	662	0	21.2	0.4	34.30	0.6	61.8	0.7
	662	45	23.4	0.3	50.52	0.5	46.3	0.6
	662	90	26.5	0.3	47.44	0.5	55.9	0.6
Mn-54	835	0	8.62	0.1	18.67	0.2	46.2	0.2
	835	45	9.21	0.1	23.45	0.2	39.3	0.2
	835	90	12.87	0.1	28.74	0.2	44.8	0.2
Co-60	1173	0	12.0	0.6	29.41	0.8	40.8	1.0
	1333	0	10.8	0.7	29.41	0.8	36.7	1.1
	1173	45	12.9	0.6	43.31	0.7	29.8	0.9
	1333	45	11.6	0.6	43.31	0.7	26.8	0.9
	1173	90	15.0	0.6	40.66	0.7	36.9	0.9
	1333	90	13.2	0.6	40.66	0.7	32.5	0.9

3.3.5. Comparison between simulated and measured results

The comparison between the simulated and measured rate can be found in Table 3.8. In this table, the energy deposition counts in the BGO crystal, higher than 400 keV, are listed. The ratio between the two results agrees very well in all cases. The biggest difference between the two results can be found in the case of the Mn-54 measurements. The reason for this circumstance is as follows: the fact that the distance between the Mn-54 source and the BGO is only 10 cm implies a bigger systematic uncertainty, induced by an inaccurate distance measurement. The comparable distance of the other two scenarios is 29.5 cm. In case the uncertainty of the distance measurement is ± 2 mm (corresponding to 2σ) the obtained uncertainty already covers the discrepancy between simulation and measurement.

The measurement uncertainties in Table 3.8 take the following contributions into account:

- Uncertainty induced by distance inaccuracies (Mn-54: $1\sigma = 1.96$ %;
Cs-137, Co-60: $1\sigma = 0.68$ %).
- Uncertainty induced by the limited knowledge of the radioactive source activities ($1\sigma = 0.67$ %).
- Uncertainty induced by the DAQ dead time correction ($1\sigma = 0.5$ %).
- Statistical uncertainties (< 0.3 %).

In case of the simulation, only statistical uncertainties are taken into consideration.

Table 3.8: Comparison between the simulated and measured counting rates ($E > 400$ keV).

Source	Angle	Measurement	Simulation	Ratio M/S
		Counts/s	Counts/s	
Cs-137	0	24.61 ± 0.26	24.3 ± 0.1	(1.01 ± 0.01)
	45	27.10 ± 0.28	27.1 ± 0.1	(1.00 ± 0.01)
Mn-54	0	10.52 ± 0.21	10.84 ± 0.01	(0.97 ± 0.02)
	45	11.53 ± 0.23	11.83 ± 0.01	(0.97 ± 0.02)
	90	15.43 ± 0.30	16.20 ± 0.02	(0.95 ± 0.02)
Co-60	0	36.46 ± 0.39	36.5 ± 0.2	(1.00 ± 0.01)
	45	39.52 ± 0.41	40.0 ± 0.1	(0.99 ± 0.01)
	90	45.56 ± 0.48	45.2 ± 0.1	(1.01 ± 0.01)

In Figure 3.5 three simulated spectra are compared with the proper measurement results. The simulated results were obtained via the two-stage process explained in Chapter 3.3.2. In order to show each angle situation once, the comparison for Co-60 is performed at of 0° , for Cs-137 at 45° and for Mn-54 at an angle of 90° . All three spectra agree very well. The fact that the real BGO used a lower energy threshold in order to discriminate the noise explains that the measured spectra do not show counts with energies lower than 50 keV. Even at slightly higher energies, the influence of the discriminator threshold is still visible. The measured “back-scattered hill” at low energies is stronger than in the comparable simulated one. The explanation of this

circumstance can be found in the fact that the simulations do not consider the influence of the surrounding walls. These walls increase only the number of back-scattered photons with a scattering angle close to 180° . With Equation 3.6, one can see that these photons correlate with energies close to the minimum back-scattering energy, listed in Table 3.4. At photon energies, which correlate to angles of back scattered γ 's originating from the two plates, the comparison between measurement and simulation agrees very well again. For the calculation of the statistical uncertainty concerning the simulation result, Equation 3.7 has to be used with the proper values of Table 3.9. The shown uncertainties of the measurements are the same uncertainty types which were already explained for the total rate.

Table 3.9: Values for the calculation of the statistical uncertainties.

	Cs-137	Mn-54	Co-60
SS	34006	2294	58320
PP	$1.25 \cdot 10^8$	$1.25 \cdot 10^8$	$1.25 \cdot 10^8$
EBIN	$6.836 \cdot 10^{-3}$	$6.836 \cdot 10^{-3}$	$6.836 \cdot 10^{-3}$

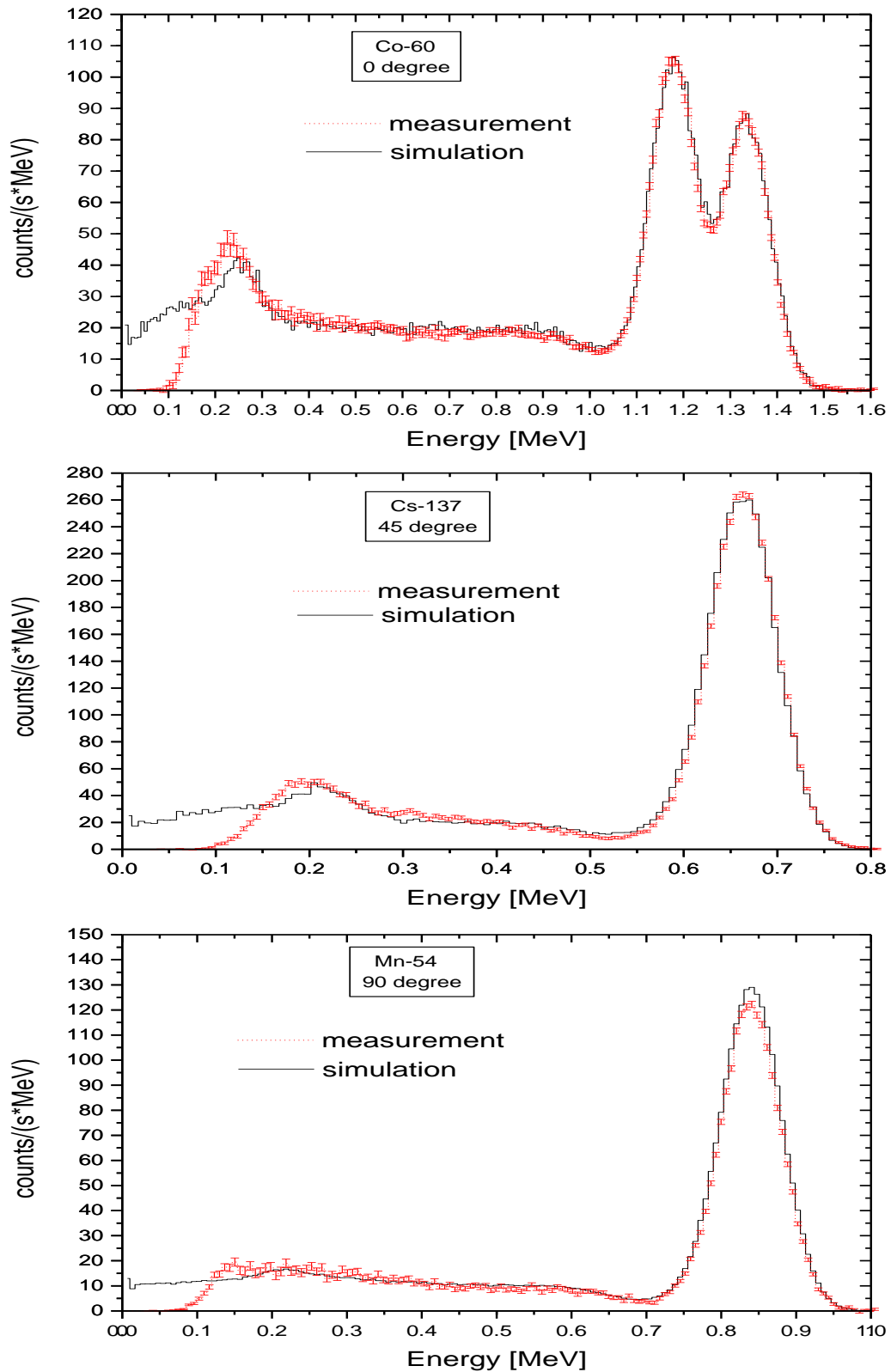


Figure 3.5: Comparison between measurement and simulation spectra. The red dotted line shows the measurement curves, including uncertainties.

3.4. BGO detector response to different neutron sources

3.4.1. Experimental set-up

In order to investigate the neutron response of the BGO detector, measurements using an Am-Be source were performed. General characteristics of the source used can be found in Table 3.10. The energy dependent spectrum of the emitted neutrons is shown in Figure 3.6. The cylindrical source itself was encapsulated in a steel cylinder in order to absorb low energy photons (~ 60 keV) originating from the ^{241}Am decay process.

Table 3.10: Characteristics of the Am-Be source.

4π neutron emission rate	4π gamma emission rate	Gamma energy	Height of the source	Diameter of the source
s^{-1}	s^{-1}	MeV	mm	mm
2220 ± 155	763 ± 41	4.439	10.7	15.8

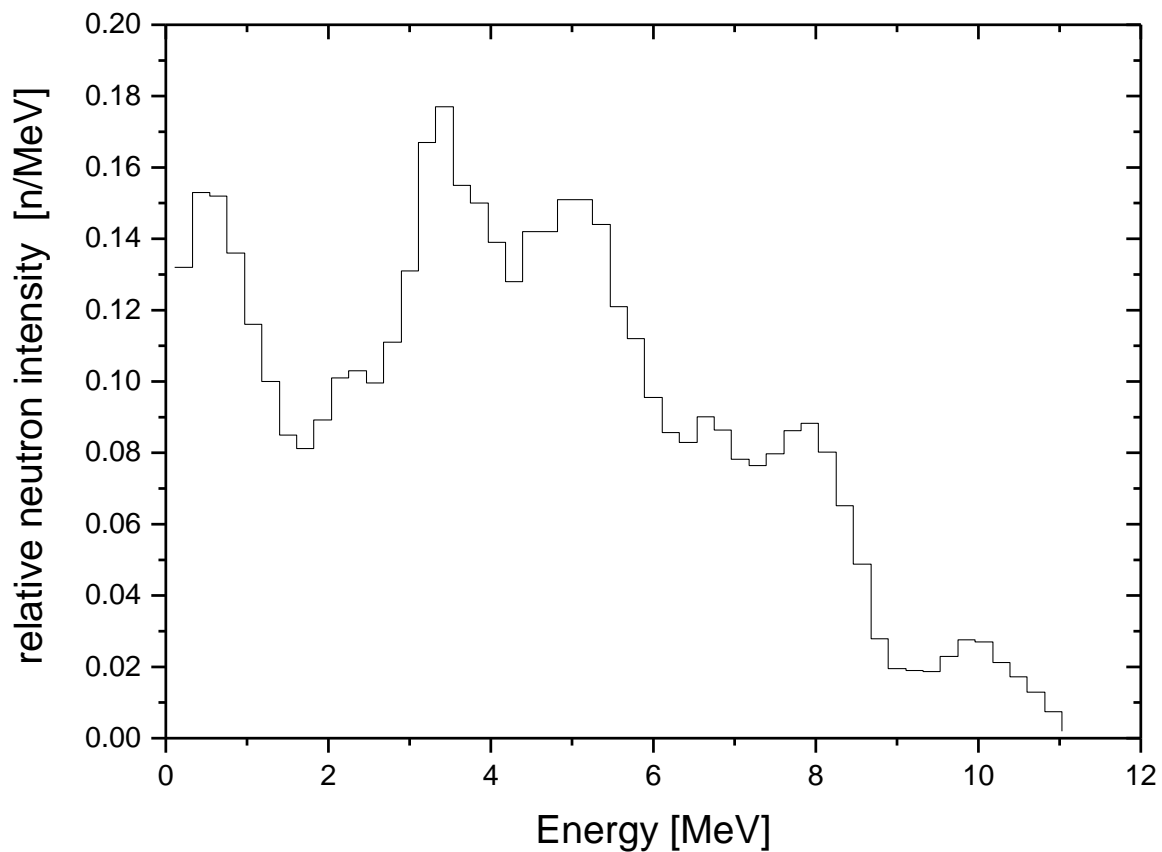


Figure 3.6: Energy distribution of the emitted Am-Be neutrons.

During the measurement cycle the encapsulated source was covered by an additional plastic bottle, which was simulated as an appropriate polyethylene cylinder. The simulated measurement set-up can be found in Figure 3.7.

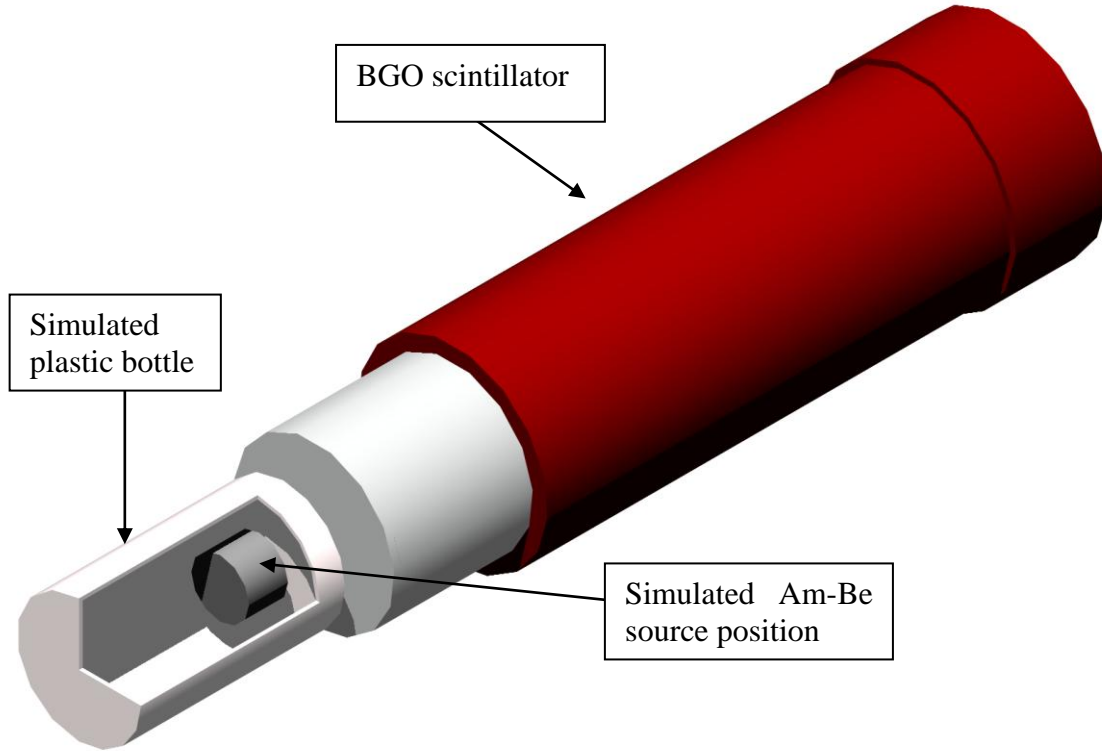


Figure 3.7: Simulated measurement set-up. In order to show the simulated position and shape of the Am-Be source, the outer cylinder (plastic bottle) is displayed in the picture with a cutout .

The emitted neutron and photon rate and the pertinent spectra of the Am-Be source were always determined as the sum of the source including the steel cover. The values concerning the number of emitted particles already contain possible reactions with the encapsulation material. Therefore, no consideration of the steel hull was performed in the simulations.

The distance between the front face of the plastic bottle and the BGO cover was 8mm. The internal structure of the encapsulation and, therefore, the accurate position of the actual source inside its cover was, unfortunately, not clearly known. Finally, based on an inaccurate sketch of the source, the simulated Am-Be source was located on the BGO axis, having a distance of 1.5 cm to the front face of the aluminum cover. Due to this small distance between source and BGO an implementation of the surrounding walls was not necessary and was, therefore, neglected in the simulation.

3.4.2. Simulation procedure to obtain measurement comparable results

In order to obtain simulation results, which are comparable to the BGO measurements, the simulation procedure was performed in three steps:

1. Separated neutron and photon history simulations in the experimental geometry. The induced energy depositions in the BGO crystal were stored in histograms.
2. The obtained BGO energy deposition spectrum was converted into a real BGO spectrum in order to compare it with the BGO measurement result.

Details concerning step one and two can be found in Chapter 3.3.2.

3. An adaptation of the simulated total spectrum to the measured one was performed.

The third step of the procedure can be explained as follows: As shown already in Chapter 3.3, FLUKA calculations concerning photon energy depositions in the BGO crystal lead to reliable results. In order to adapt the simulated total spectrum to the real number of particles entering the BGO, the factor between the simulated and the measured gamma counts in the range of 4.439 MeV has to be determined. The calculated total energy deposition spectrum has to be multiplied with this normalization factor in order to obtain a measurement comparable simulation result. This normalization adapts the simulated geometry, in particular the distance between the Am-Be source and the BGO, to the experimental dimensions.

3.4.3. Procedure to obtain particle currents entering the BGO

The procedure described in Chapter 3.3.3 was used with the following modification in order to obtain particle current results for the Am-Be situation. Compared to the photon simulation (all materials were set to vacuum) the plastic bottle keeps its real material composition. To obtain the number of particles having a flight direction to the BGO crystal, the reactions of the neutrons and photons with the bottle material has to be taken into account. The probability of a photon or neutron hitting the BGO crystal can be found in Table 3.11. The small difference between the total photon rate and the rate of photons with an energy of 4.439 MeV can be explained by possible reactions of primary γ particles with the bottle material. An interacting primary gamma can be converted into a photon with lower energy. It can be concluded from these results that the simulated bottle has almost no influence on the spectrum of the source.

Table 3.11: Probability of primary neutrons and photons to cross the BGO crystal

Particle	Crossing probability %
Neutrons	10.31 ± 0.01
Photons	10.36 ± 0.01
Photons (4.439 MeV)	10.30 ± 0.01

3.4.4. Simulation results

3.4.4.1. Energy deposition in the BGO

Analysis of induced photon processes

The simulated energy deposition spectrum induced by Am-Be photons is shown in Figure 3.8.

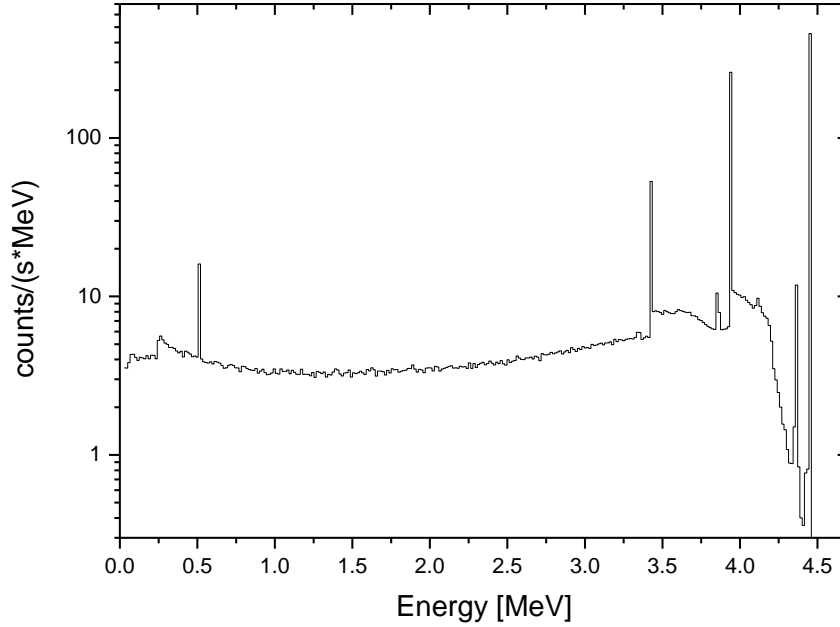


Figure 3.8: Simulated BGO energy deposition spectrum induced by Am-Be photons (4.439 MeV).

The statistical uncertainty of the simulation result is calculated with Equation 3.7 using the necessary values of Table 3.12.

Table 3.12: Values for the calculation of the statistical uncertainties

	SS	PP	EBIN
Am-Be	763	$2 \cdot 10^7$	$1.465 \cdot 10^{-2}$

The characteristic energy points of the energy deposition spectrum in Figure 3.8, including their pertinent effects are as follows :

242 keV: First possible energy deposits induced by Compton back-scattered photons become visible. This point corresponds to the energy of a 180° back-scattered photon. The primary photon, having an energy of 4.439 MeV, crosses the BGO crystal without performing a reaction. In the

material outside the crystal the γ particle is Compton scattered and produces beside the scattered electron a photon, which reaches again the detection area of the BGO. The minimal possible energy of this back-scattered photon is 242 keV and corresponds to a scattering angle of 180° .

- 511 keV: The primary photon produces in the surroundings of the crystal an (e^+, e^-) pair. The positron annihilates into two photons with energies of 511 keV. These photons have an angle difference of 180° . Therefore, only one of them can reach the crystal in order to produce an energy deposition at the stated energy.
- 3417 keV: Double-escape peak: The primary photon produces a (e^+, e^-) pair in the crystal. Both of the 511 keV photons, which were produced in the annihilation process of the positron, escape the crystal. Therefore, the energy deposition of this process is $(4.439 - 1.022)$ MeV.
- >3417keV: This part of the spectrum can be explained by a Compton process of one or even of both of the 511 keV photons. The scattered photon(s) of this process escape the system.
- 3845 keV: Combination of single-escape and photo-escape peaks. This peak originates from an annihilation of an e^+ , which was produced by pair production. One of the 511 keV photons induce a photo effect. The resulting X-ray escapes the system. The second 511 keV photon escapes the crystal. Therefore, the energy gap between this energy and the primary photon energy is obtained by losing the energy of the X-ray particle and one of the 511 keV photons.
- 3928 keV: Single-escape peak: the same process as explained before occurs. However, no X-ray escapes the crystal. The energy difference between the photo peak and this peak is therefore 511 keV.
- >3928keV: The range adjacent to the single-escape peak can be explained via a Compton process of one of the 511 keV photons. The scattered photon of this process escapes the system. The energy of the second annihilation photon is absorbed completely.
- 4197 keV: The possible range of the energy transfer from the primary photon to a crystal electron via a Compton effect ends at this energy. A strong decrease of the continuous spectrum until the next significant peak can be observed.
- 4355 keV: Photo-escape peak: a produced X-ray particle escapes the crystal and does not contribute its energy.
- 4439 keV: The whole energy of the entering photon is absorbed in the crystal. This peak is independent of the processes taking place inside the crystal. The crucial effect to achieve the total energy peaks is that all secondary produced particles are absorbed in the BGO crystal.

The necessary values to determine the efficiencies of the BGO can be found in Table 3.13. The efficiencies including their statistical uncertainties were evaluated with Equation 3.8 and 3.9.

Table 3.13: Necessary simulated values in order to calculate the BGO efficiencies to the 4.439 MeV photons.

Total current in BGO	Current of 4.439 MeV in BGO	Counting rate > 400 keV	Efficiency > 400 keV	Photo peak rate	Photo peak efficiency
γ/s	γ/s	Counts/s	%	Counts/s	%
79.05 ± 0.08	78.60 ± 0.08	29.69 ± 0.03	37.60 ± 0.05	6.68 ± 0.02	8.50 ± 0.03

The probability of absorbing the whole photon energy in the BGO (photo-peak efficiency) is in this case much smaller than in case of the low-energy sources. The higher the primary energy of the photons, the higher is the chance that a part of the energy will escape the crystal. But on the other hand, the probability of inducing a count with different energy deposition does not decrease as strongly as in case of the photo-peak efficiency.

Analysis of induced neutron processes

The simulated energy deposition spectrum in the BGO crystal, induced by Am-Be neutrons, is shown in Figure 3.9.

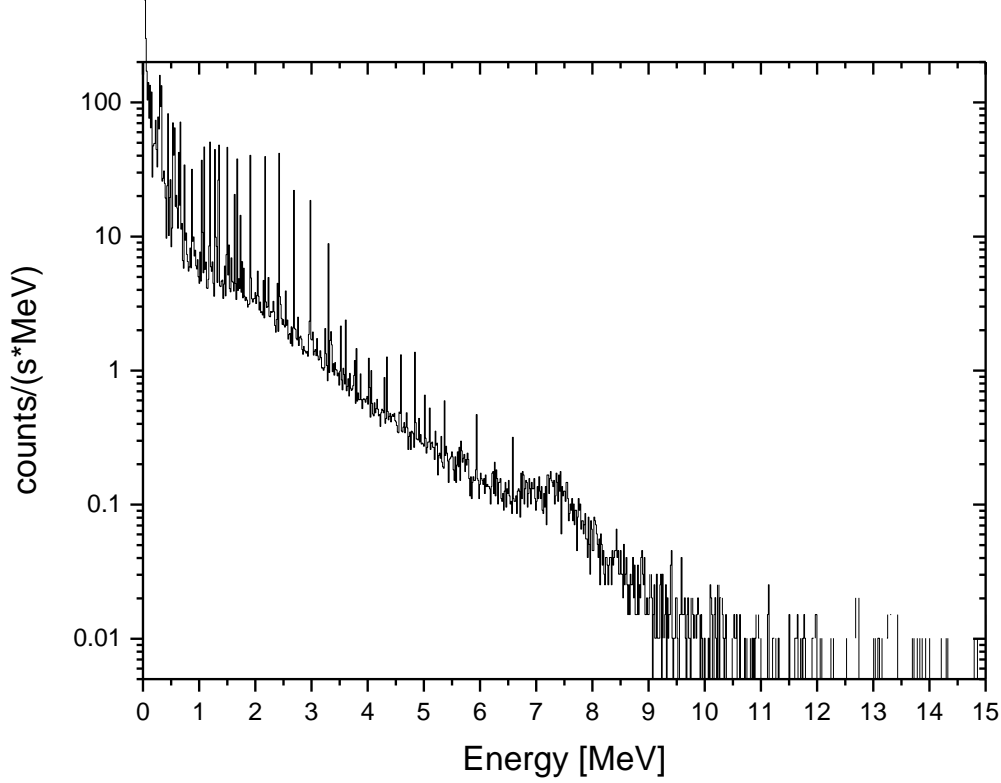


Figure 3.9: Simulated BGO energy deposition spectrum induced by Am-Be neutrons.

The statistical uncertainties of the single counts in Figure 3.9 can be calculated by using Equation 3.7 and the values of Table 3.14.

Table 3.14: Values for the calculation of the statistical uncertainties of Figure 3.9.

	SS	PP	EBIN
Am-Be	2220	$3 \cdot 10^7$	$1.465 \cdot 10^{-2}$

At all energies, strong peaks are added to the continuous part of the spectrum. This circumstance is explainable through the FLUKA energy bin structure of low energy neutrons (see Appendix A). The bin structure requires a special procedure concerning the simulation of neutron-caused energy depositions. The simulation for neutrons with energies below 19.6 MeV and for photons produced by these neutrons is as follows: The simulated neutrons, having an energy between 0 and 19.6 MeV, are split in 72 energy dependent groups. Below this 19.6 MeV threshold, the neutrons no longer have a well-defined energy, but rather they belong to a specified energy group. If the

neutron, belonging to one of these groups, undergoes a reaction in the material, the following simulations procedure is performed. At the scattering process the particle is given a specified probability to stay inside the same energy group or to be down-scattered into a group covering a lower energy range. No matter to which group the neutron is scattered (even scattering within the same group), the computed energy deposition for this simulation step is always the same. This energy amount is a mean value of all energy depositions, which can be induced by neutrons of the pertinent energy group. The energy deposition peaks of the simulated spectrum, which is displayed in Figure 3.9, are produced by this simulation procedure. These sharp peaks correspond exactly to the average value of the possible neutron energy depositions, which are stored for the energy dependent groups of Ge, Bi and O. Further details about these energy groups and the energy deposition values can be found in Appendix A. In order to give examples of this procedure a few energy deposition bins of the spectrum in Figure 3.9 are explained more explicitly in Table 3.15.

Table 3.15: Details of 6 simulated energy peaks, induced by Am-Be neutrons in the BGO crystal.

Deposited energy	Material	E_{\min} of neutron energy bin	E_{\max} of neutron energy bin	Neutron group number
MeV		MeV	MeV	
0.2193	Bi	6.7032	7.4082	10
0.2581	Bi	7.4082	8.1873	9
1.340	O	6.7032	7.4082	10
1.716	O	10.000	11.052	6
2.678	Ge	8.1873	9.0484	8
3.284	Ge	10.000	11.052	6

At each scattering process, the actual neutron has also a well specified probability to produce secondary neutrons and photons. In case a photon is produced, the energy of this gamma is selected within a given photon energy group structure (see Appendix A). The neutron induced photons have, in general, an energy between 0 and 20 MeV. Also this energy range is divided into 22 energy dependent groups. The actual energy group, chosen for the produced gamma, is selected by given probability distributions, which are assigned to the scattering nuclei and to the energy groups of the scattered neutron. After this group is selected, the photon energy, which is passed through to the EM part inside FLUKA, is chosen randomly inside the actual group.

The necessary values to determine the efficiencies of the BGO to neutrons can be found in Table 3.16. The efficiencies with their statistical uncertainties were evaluated with Equation 3.8 and 3.9.

Table 3.16: Simulated values in order to calculate the BGO efficiencies to Am-Be neutrons, having an energy spectrum between 0 and 11.03 MeV.

Total n current in BGO	Counting rate > 100 keV	Efficiency > 100 keV	Counting rate > 400 keV	Efficiency > 400 keV
γ/s	Counts/s	%	Counts/s	%
228.8 ± 0.2	47.00 ± 0.19	20.54 ± 0.08	27.98 ± 0.15	12.01 ± 0.06

3.4.5. Comparison between simulated and measured results

As already mentioned in Chapter 3.4.2.2, a normalization factor between the simulation and the measurement has to be evaluated. This normalization adapts the simulated geometry, in particular the distance between the Am-Be source and the BGO, to the experimental dimensions. In order to obtain this factor, the simulated and measured Am-Be photo peaks were integrated between 4.3682 and 4.5527 MeV. Within this energy range the measured counts are dominated by photon induced effects. Therefore, a comparison between the integrated photo peaks leads to the desired result. The simulated and measured rate within this energy range can be found in Table 3.17. In order to adapt the simulation to the real circumstances, the computed results have to be multiplied with this factor. In Figure 3.10, the convoluted and normalized simulation spectrum is compared with its measured counterpart.

Table 3.17: Comparison between measured and simulated photo peak within an energy range of 4.3682 and 4.5527 MeV.

Measured photo peak	Simulated photo peak	Measurement/simulation
Counts/s	Counts/s	
6.9459	4.6691	1.4876

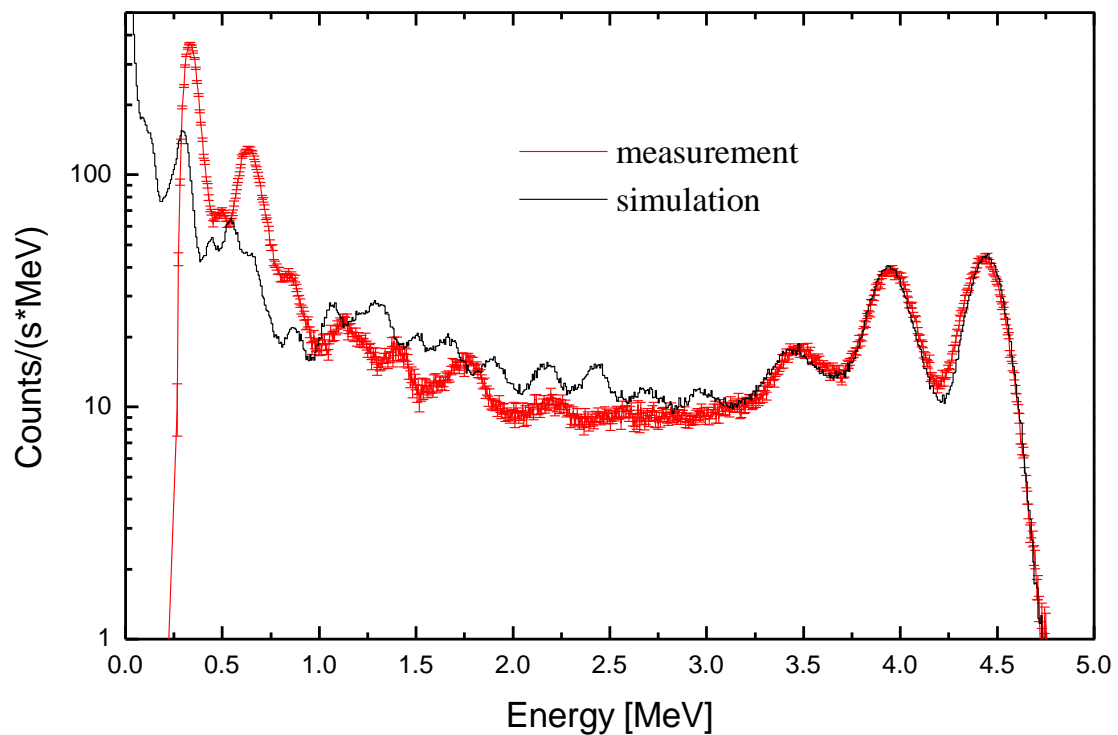


Figure 3.10: Comparison between measured and simulated BGO energy deposition spectrum induced by an Am-Be source.

The spectrum shows a very good agreement in the range of photon induced effects, namely for the photo, the single-escape and the double-escape peaks. In the lower energy range, which is dominated by neutron induced energy depositions, discrepancies between the two results can be found. In order to achieve a better understanding of these discrepancies, the simulated gamma spectrum was subtracted from the measurement spectrum. The result of this procedure is compared with the simulated neutron energy deposition and can be found in Figure 3.11.

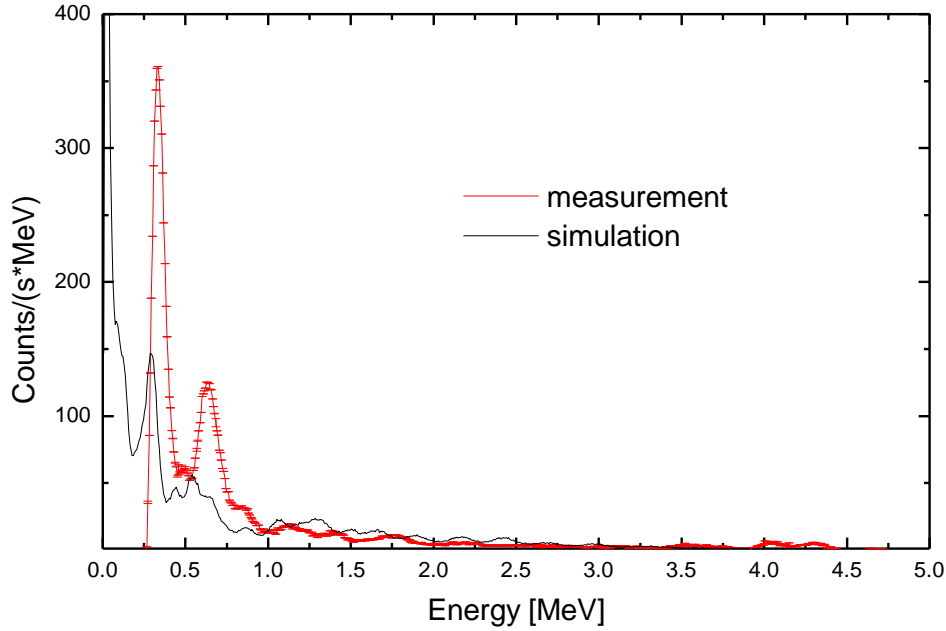


Figure 3.11: Simulated and measured BGO neutron response to Am-Be neutrons.

The uncertainty of the simulation in Figure 3.11 can be calculated by using Equation 3.7 in combination with the necessary values given by Table 3.18. But the resulting uncertainties have to be multiplied with 1.220 ($=\sqrt{1.4876}$). This factor takes the normalization between simulation and measurement into account.

Table 3.18: Values for the calculation of the statistical uncertainties of Figure 3.11.

	SS	PP	EBIN
Am-Be	2220	$3 \cdot 10^7$	$6.836 \cdot 10^{-3}$

The reason that the peaks in the simulated neutron spectrum do not agree with the measured peaks, can be found in the explanation of the simulated energy deposition procedure of neutrons in FLUKA.

Also, the real existing and therefore, measured peaks, originating mainly from (n,n',γ) processes are simulated only approximately in the explained way. For example, the measured peak at around 630 keV is induced by inelastic collisions between neutrons

and various Ge isotopes. This peak is a combination between (n,n',γ) processes of ^{76}Ge (563 keV), ^{74}Ge (596 and 609 keV), ^{72}Ge (630 keV) and ^{70}Ge (668 keV), which are induced by scattered neutrons. In the used simulation cross sections only the probability of producing photons in the energy range between 400 keV and 1 MeV (photon group number 19) is stored. This probability corresponds to the real probability of neutron induced photon production in this energy range. The actual simulated energy of the photon, which is referred to the EM part in FLUKA, is chosen randomly within this energy range. Therefore, no sharp peaks, originating from neutron induced photons, can be found in the simulated spectrum. Another reason that the simulated spectrum does not correspond to the measured one can be found in the unknown correlation between the production of scintillation photons and the energy deposition in the crystal, induced by neutrons and heavier particles.

However, the total rate (integrated counting rate between 10^{-5} eV and infinite) can be expected to be simulated correctly because the total cross sections of Bi, Ge and O are implemented correctly in FLUKA. Therefore, the probability that a neutron undertakes any kind of reaction inside the crystal is taken correctly into consideration. But the amount of deposited energy and, therefore, the location of the produced count in the spectrum, which is induced by a single neutron, cannot be expected to be correct. In general, the further away one of the integration thresholds is set from the mentioned values the less of the total spectrum is taken into account for the summation of the rate within a given range. Therefore, the integrated rate over a small energy range can disagree with the measurement. In Table 3.19 the simulated and measured counting rates within an energy range of 400 keV – 6.5 MeV are shown.

Table 3.19: Simulated and measured BGO counting rates (400 keV – 6.5 MeV).

Simulation	
	Counts/s
total spectrum	$85,1 \pm 3.9$
γ spectrum	44.2 ± 2.5
n spectrum	40.9 ± 3.0
Measurement	
	Counts/s
total spectrum	96.5 ± 0.1
n spectrum	52.3 ± 2.5

The uncertainties of the simulation results contain statistical uncertainties, influences induced by the measured neutron ($1\sigma = 7\%$) and photon activities ($1\sigma = 5.4\%$) as well as uncertainties induced by the adaptation via the photon rate (2%). For the measured uncertainty only the statistical error is regarded. The main reason for the disagreement between measured and simulated neutron rate ($\sim 30\%$) can be found in the lower integration threshold (400 keV) of the observed energy deposition range.

The simulated γ and neutron currents entering the BGO crystal are calculated to (117.6 ± 6.6) γ/s and (340.5 ± 24.8) n/s . This value includes also the geometrical correction of 1.4876. With these values the measured BGO efficiency for neutrons can be calculated to be $(15.4 \pm 1.4)\%$.

3.5. Summary of this chapter

In this chapter the response of the BGO to photons and neutrons was investigated.

The first part of this chapter dealt with the BGO response to low energy photons. Three different radioactive sources, namely Cs-137, Mn-54 and Co-60, were used in order to irradiate the detector. The energy deposition in the BGO crystal was simulated in detail. Physical effects, like pair production, Compton scattering and photo-effect, were reproduced in the simulation with high accuracy. The comparison of the simulated rate with the measured one yields an agreement mostly better than 2 %. Concerning the comparison of the simulated spectra with their measured counterparts one can say that their agreement is very good in all energy regions. Effects, like photo peaks, Compton edges or single- and double-escape peaks coincide in all details with the proper measured values. We conclude that we understand the absolute photon response at the 2 % level.

In the second part of this chapter, the response of the BGO detector to Am-Be source particles was simulated. The simulation of the energy deposition spectrum induced by Am-Be photons agrees very well with the measurement. Concerning the simulation of the energy deposition induced by neutrons one can summarize the situation as follows: The integrated rates between 400 keV and 6.5 MeV agree at a level of 30 %. This discrepancy between the measured and the simulated rate is mainly due to the high value of the lower integration threshold (400 keV). The simulated counts in the BGO can be expected to be correct in terms of their number, but not in terms of the single energy deposit. Concerning the simulated neutron spectrum one has to mention that the agreement with the measured graph is not very good. Also this fact can be explained with the FLUKA simulation procedure concerning energy deposit. It should be stressed that the FLUKA simulation procedure, concerning energy depositions of neutrons, has in general no distortion effect on the total neutron counting rate. Integral neutron efficiencies can therefore be quite reliably obtained with FLUKA.

CHAPTER 4

4. Simulation of the ATLAS equivalent measurements

4.1. Introduction

As mentioned previously, the calculated ATLAS background levels were increased by an uncertainty factor of 5 in order to cover all possible simulation uncertainties. The main contributor (2.5) to this factor is the uncertainty of the background fluence calculations, which were performed with FLUKA. Up to now, no relevant benchmarking, concerning a situation similar to the ATLAS background scenario, was realized. This kind of benchmark would have to focus on the electromagnetic and hadronic shower productions and the transport of the produced particles inside a shielding, which is similar to the Atlas calorimeter construction. The showers have to be induced by incoming particles, which have energies similar to the particles produced by the proton-proton collision in ATLAS.

The benchmarking simulations, presented in this chapter, deal with the simulation of experiments, which were performed in the H6 area at CERN. During these measurements, a big cast iron absorber was irradiated by a hadron beam. Behind the absorber a measurement set-up, which measured the energy deposition induced by the produced particle showers, was installed. This scenario can be shown to be similar to the photon and neutron background situation at the range of the muon chambers in ATLAS. A BGO detector, described in Chapter 3.2, was used to measure energy depositions induced by various particles.

We first describe the simulated measurement set-up including the beam facility. Furthermore, a detailed explanation, concerning the simulation procedure, is given. This section is followed by a presentation of the simulation results. At the beginning of this subchapter, the induced radiation conditions around the BGO detector are discussed. Not only the fluences in the range of the BGO detector, but also the hadronic origin of the single particles, entering the detector, are explained. At the end of the chapter, the simulated results concerning the energy depositions in the BGO crystal are presented and discussed in detail.

4.2. SPS and H6 area

The ATLAS benchmarking experiments were performed in the H6 area, which is located in the Northern Area of the Super Proton Synchrotron (SPS) accelerator at CERN. The H6 area can be provided with different kinds of particles having various momenta between $5 \text{ GeV}/c < p/z < 205 \text{ GeV}/c$ (z being the particle charge). The particle beam is produced by an irradiation of a beryllium target (T4) with a 450 GeV/c proton beam, coming from the SPS. The beam intensity of the SPS can be as high as several 10^{12} particles per burst. Between each burst, which lasts 2.58 seconds, the machine needs another 11.82 seconds to accelerate another bunch of protons to the desired 450 GeV/c.

Behind this Be target a sophisticated system of beam optic elements filters particles with the desired momentum. From the target position the beam is sent to the H6 area. The beam line between T4 and H6 is well defined by a set of magnets and collimators. Before the beam enters the H6 area it crosses an ionization chamber, called PIC-counter. With this device the intensity of the beam is evaluated. The beam line from the T4 production target to the PIC-counter is about 390 m long. The particle path is monitored along the track via several scintillators and Multi Wire Proportional Chambers.

4.3. ATLAS equivalent shielding

In order to benchmark the ATLAS background simulations, a measurement situation similar to the ATLAS calorimeter and shielding conditions has to be implemented. Hence, the chosen experimental construction has to satisfy the following requirements:

1. In terms of hadronic absorption length the shielding depth has to be similar to the absorption power of the ATLAS forward calorimeter. This part of the calorimeter system can be seen as the main source for the high neutron and photon background fluences in the surroundings of the muon spectrometer in ATLAS.
2. The primary particles used for this set-up should be similar to the particles emerging from the p-p collision in ATLAS. The particle fluence produced in a interaction between two protons at LHC energies consists mainly of pions.

The chosen experimental set-up for the measurement consists of cast iron, which is irradiated mainly by pions. It satisfies the required specifications in both points.

4.4. Experimental set-up

The experimental set-up was build in the H6 area at CERN. This area was implemented in all FLUKA simulations in order to obtain realistic and reliable simulation results, which are compared with the pertinent measurements. The simulated H6 area geometry used for these calculations is displayed in Figure 4.1.

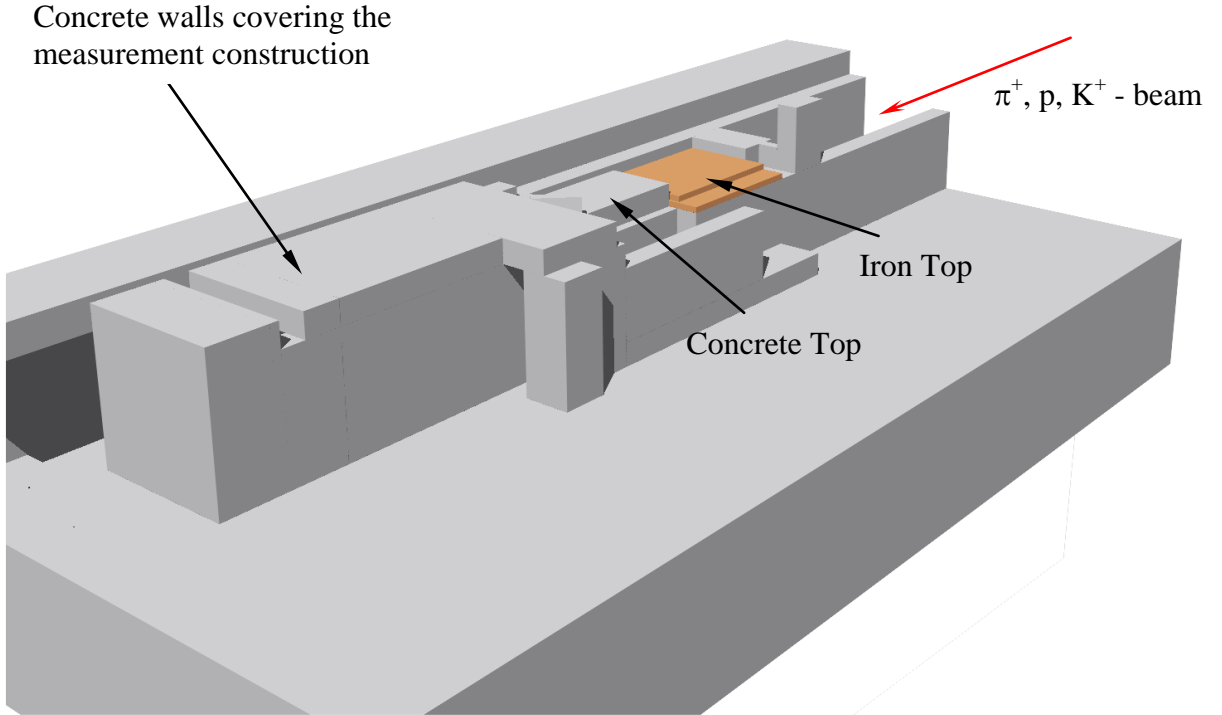


Figure 4.1: Simulated H6 area (grey structure consists of concrete).

All necessary materials of the H6 area are taken into account with their real composition, position and dimension. Inside the concrete part on the left side of Figure 4.1, the experimental set-up was installed. Instead of irradiating a cylindrical copper target, which is normally positioned below one of the measurement platforms (Iron Top or Concrete Top), a huge cast iron block was exposed to the primary beam particles. The internal structure of the beam line, including the cast iron absorber block and the experimental set-up is shown in Figure 4.2. The beam, which is displayed in the pictures as an arrow, enters the beam area by passing through an ionization chamber. Starting from the position of this chamber the hadron beam was simulated with the appropriate particle composition and direction.

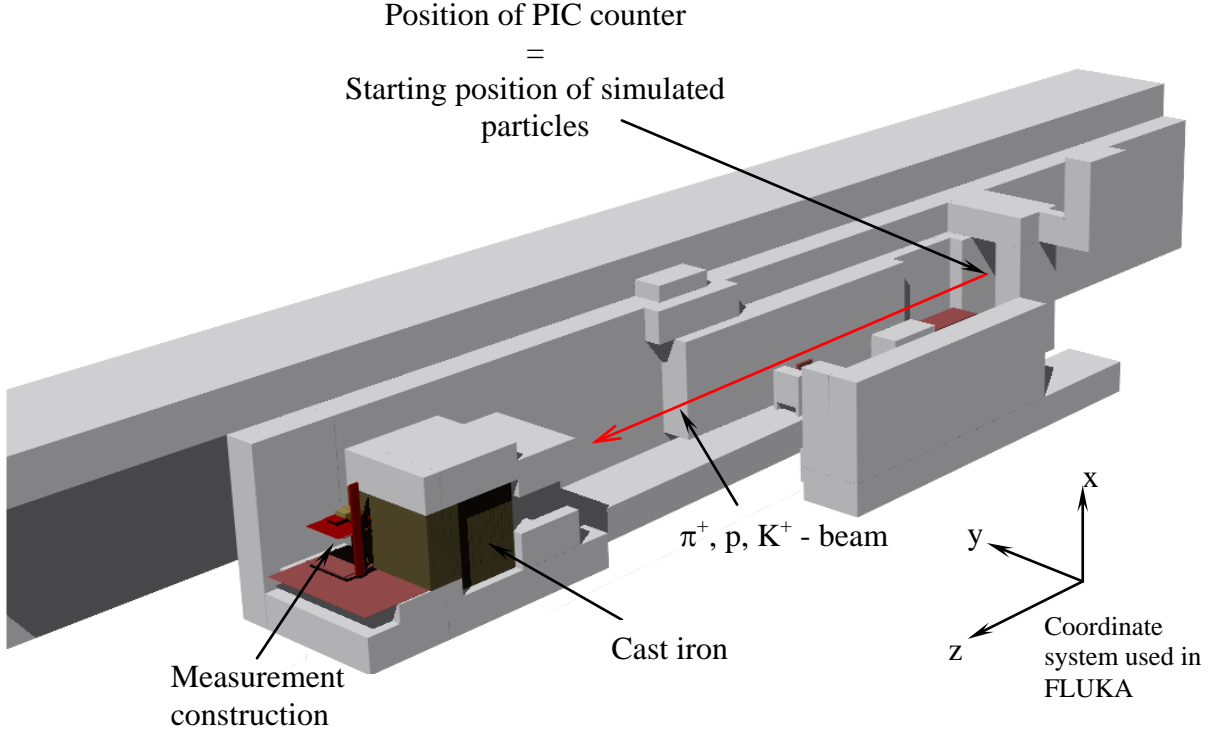


Figure 4.2: Simulated set-up for the ATLAS background benchmarking (240 cm cast iron, BGO at side position) created using FLUKACAD [Vin00] and AutoCAD. The outer shielding of the H6 area is partly removed to show the internal structure of the experimental set-up.

The simulated experimental set-up has to be comparable to the ATLAS environment. For the implementation of this aim the following experimental construction was chosen: a cast iron wall with a thickness of 200 cm (11λ) and 240 cm (14λ), respectively, was irradiated by a mixed positive charged hadron beam (π^+ , protons, K^+). The momentum of the beam was either 40 or 120 GeV/c. The iron represents the material of the forward ATLAS calorimeter. The beam energies are close although higher to the typical secondary particle energies in the forward region of ATLAS. Before the beam reaches the iron absorber it has to cross two plastic scintillators. These scintillators, which are installed in order to count the number of primary beam particles hitting the shielding, are also realized in the simulations (behind the concrete close to the absorber and, therefore, not visible in the Figure 4.2). Behind this cast iron wall a measurement set-up, including the BGO scintillator, was installed. Two positions for the BGO were chosen. The first position can be found between 6 and 10 cm (BGO crystal position) off beam axis and is called “mid position”. The second measurement position, called “side position”, is located between 56 and 60 cm (BGO crystal position) off beam axis. The simulation situation in Figure 4.2 shows the geometry for the iron shielding depth of 240cm. The measurement set-up in this picture is located at the “side position”. Figure 4.3 shows the situation close to the used measurement set-up. In this picture, the post belonging to the support was removed in order to show all simulated measurement devices.

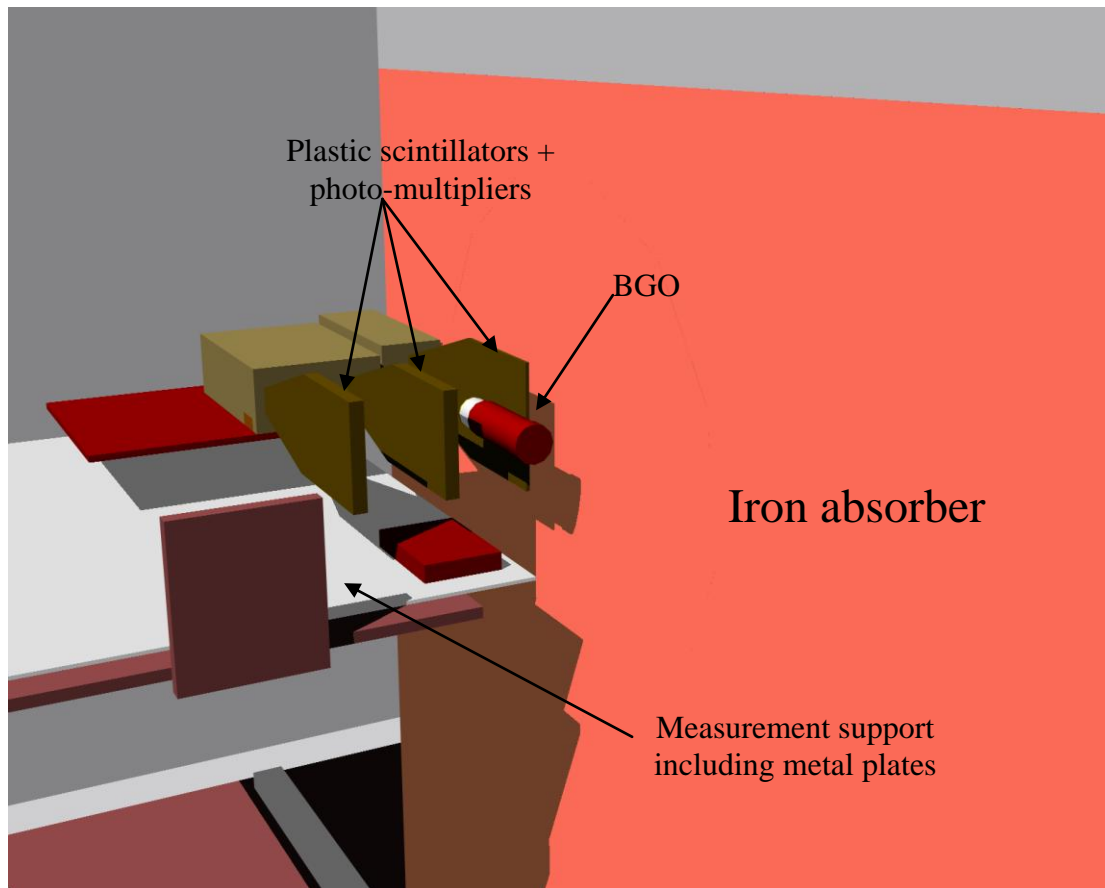


Figure 4.3: Simulated measurement construction including the BGO scintillator and 3 plastic scintillators.

The measurement construction consists of the described BGO scintillator and three plastic scintillators. In the measurements the three plastic scintillators were used in order to discriminate different particle types. But for the comparison with the simulation results only the total counting rate induced in the BGO was used. However, the material of the scintillator (including their photo-multipliers) influences the particle fluence entering the BGO crystal. This made a consideration of the device materials in the simulation necessary. In addition, the whole geometry close to the BGO was modeled very accurately in order to account the effect, induced by surrounding materials. Further details, concerning relevant simulation parameters, can be found in the list below.

- Distance between PIC counter (starting point of simulated beam) and first beam particle scintillator: 17.3 m
- Distance between first and second beam scintillator: 40 cm
- Distance between second beam scintillator and beginning of the iron absorber: 1.8 m
- Simulated parameters of the beam scintillators:
 - Material: polystyrene (plastic consisting of C and H in the rate 1:1)
 - Density: 1.05 g/cm³
 - Dimensions ($\Delta x : \Delta y : \Delta z$): 10 cm : 30 cm : 1 cm

- Simulated parameters of the cast iron absorber:
 - Density: 7.2 g/cm^3
 - Carbon contents: 5 wt-%
 - Dimensions ($\Delta x : \Delta y : \Delta z$) : (160 cm : 200 cm : 160 cm) + (160 cm : 240 cm : 40 or 80 cm)
 - Holes in the absorber close to the beam axis and close to the measurement construction were taken into consideration in the simulation.
- Simulated parameters of veto scintillators (polystyrene) including light guides:
 - “Charged scintillator” (next to iron wall):
 - ❖ distance to iron wall: 5.5 cm
 - ❖ dimensions: area = 586 cm^2 , width = 0.5 cm
 - “Muon scintillators”:
 - ❖ distance to iron wall: 16 and 29 cm, respectively
 - ❖ dimensions: area = 2 times (457 cm^2 , width = 2cm)
- Simulated parameters of concrete:
 - Density: 2.4 g/cm^3
 - Water contents: 5 wt-%
- Distance between BGO axis and iron wall: 9.0 cm
- Other materials around BGO detector: measurement set-up support including used plates consisted mainly of aluminum and iron.

4.5. Simulated beam conditions

For the performed measurements two different beam energies and, therefore, two different primary particle compositions were used. The beam momenta used were 40 GeV/c and 120 GeV/c. The production of the beam particles can be explained as follows: A proton beam with a momentum of 450 GeV/c is shot to a Be production target. The secondary produced particles leaving the target can be sorted out by momentum and particle composition. The possible decay of particles on their way from the production target to the ionization chamber (390 m), called PIC counter, has to be considered in order to determine the real particle composition at the PIC counter position. These compositions are used in the calculations. In the simulations, the beam was shot from the position of the PIC counter into the direction of the iron target. The simulated beam at this position was realized with an Gaussian distributed elliptical shape. The used $\sigma_{\text{horizontal}}$ and σ_{vertical} and the simulated beam compositions are listed for both energies in Table 4.1. More details about the beam can be found in [Amb99].

Table 4.1: Simulated beam particle compositions and intensity distributions at the position of the ionization chamber (PIC counter).

Composition	π^+	p	K^+	Beam intensity distribution	$\sigma_{\text{horizontal}}$	σ_{vertical}
	%	%	%		mm	mm
40 GeV/c	84.8	12.2	3.0		3.67	2.83
120 GeV/c	60.7	34.8	4.5			

The uncertainties of the nominal beam compositions and the influences originating from these uncertainties on the simulation results are discussed in Chapter 4.8.

4.6. Simulation procedure for obtaining results

The simulations of counting rates in the BGO were generally performed in 3 steps:

- 1) Simulation of the shower processes induced by the primary beam particles. Information about particles hitting the BGO is written to a file. This file contains details concerning position, direction, energy, statistical weight and information about the origin of the single particles.
- 2) The stored particles are shot in a second run in the BGO in order to simulate the energy deposition induced in the BGO crystal.
- 3) The obtained BGO energy deposition spectrum is converted into a real BGO spectrum in order to compare it with the BGO measurement result.

4.6.1. Simulation of the shower processes induced by the primary beam particles

For a correct calculation of the first steps, two different kinds of scenarios were investigated. The first covers all situations where the BGO detector is located close to the beam axis (“mid positions”). The second kind of scenario, which focuses on the situation where the BGO is located at side positions, has to be performed in a different way. These two positions were chosen to probe the low energy tail of the hadronic cascade at two very different lateral positions. They were also chosen to obtain complementary information on the background.

4.6.1.1. Simulations with the BGO at mid positions

For the BGO located in the mid position, only analog runs can be performed. The reason for this is as follows: late hadronic shower processes occur very close to the beam axis. These processes produce among other particles also π^0 's. The π^0 's decay almost at the position of their production into two high energy γ 's, which induce an electromagnetic shower in the absorber. Many low energy γ 's, electrons and positrons can be found at later stages of this EM shower. In case such a π^0 production happens deep in the absorber and close to the BGO, the crystal can be hit by many particles at the same time. To calculate the following energy deposition in the crystal correctly, all shower particles originating from the same primary beam particle, hitting the BGO, have to be simulated together in one stage. That means that particles originating from the same shower can induce at most one count. In a biased run the correlation between the primary beam particles and the shower particles entering the crystal is lost. Therefore, a biased simulation for this kind of situation would lead to incorrect results. Only if almost no “multi-events” occur, a biased execution of the first run is acceptable. In Figure 4.4 an electromagnetic shower induced by a hadronic interaction with following π^0 decay in mid position is shown. This picture shows an event consisting of many particles, hitting the BGO crystal (highlighted cylinder) together.

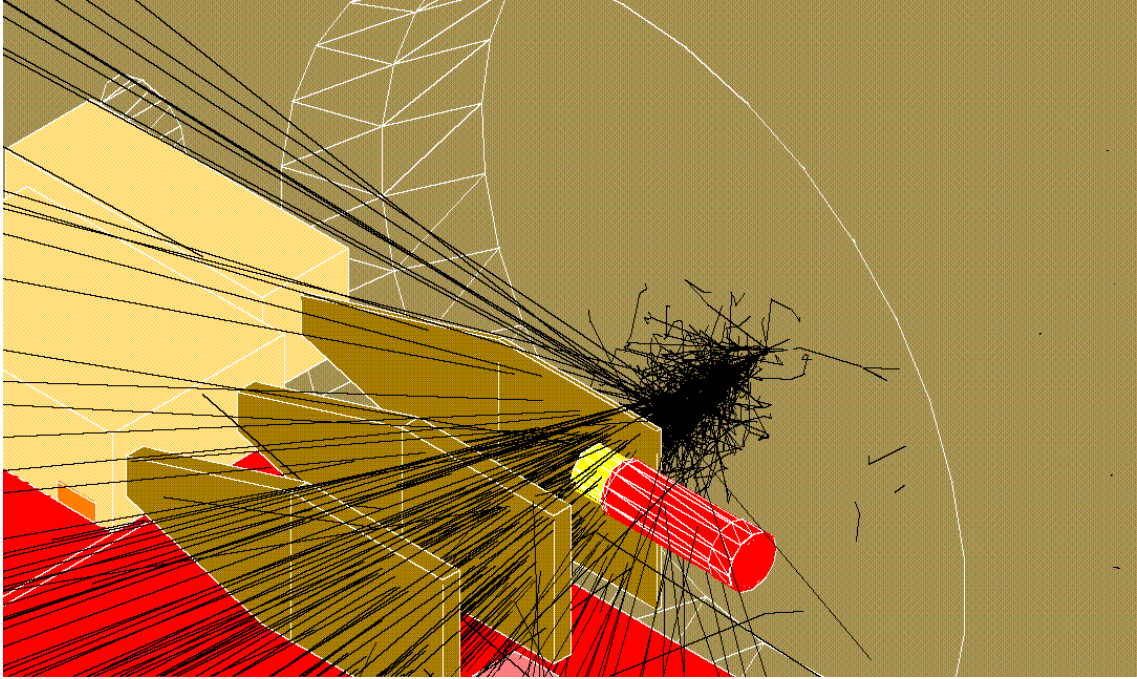


Figure 4.4: Electromagnetic shower induced by a hadronic interaction with subsequent π^0 decays. The last 20 cm of the inner part of the iron wall are removed in this picture in order to show the beginning of the shower. All FLUKA geometry pictures in this thesis were created using FLUKACAD / PIPSICAD [Vin00] and AutoCAD.

4.6.1.2. Simulations with the BGO at side positions

To obtain BGO counting rates, analog runs were performed also for the side positions. But the number of particles hitting the BGO crystal is far too small to obtain an energy dependent rate spectrum with acceptable statistics. Therefore, runs including sophisticated biasing techniques were carried out. This procedure is justified at side positions, because at these locations the amount of multi-events is negligible. Hence, the particles, including all necessary information, are stored on a file and are treated in the second run according to their statistical weight. The biasing areas in the iron absorber are shown in Figure 4.5. In order to show the different biasing regions, a cut through the absorber was performed in this picture. To increase the amount of particles reaching the BGO, a cone inside the absorber, containing regions with higher biasing importance, was implemented. The small end of this cone is hit by the beam. To bias the particle shower in direction BGO, the large end of the cone is shifted into the direction of the measurement construction. Furthermore, a general increase of the biasing importance with increasing absorber depth, starting at the beam entry position, was utilized. To prevent weight fluctuations of the particles entering the BGO detector, “Weight Windows” were implemented at the necessary positions.

In order to check the biased result, the simulated counting rate has to be compared with the pertinent analog rate.

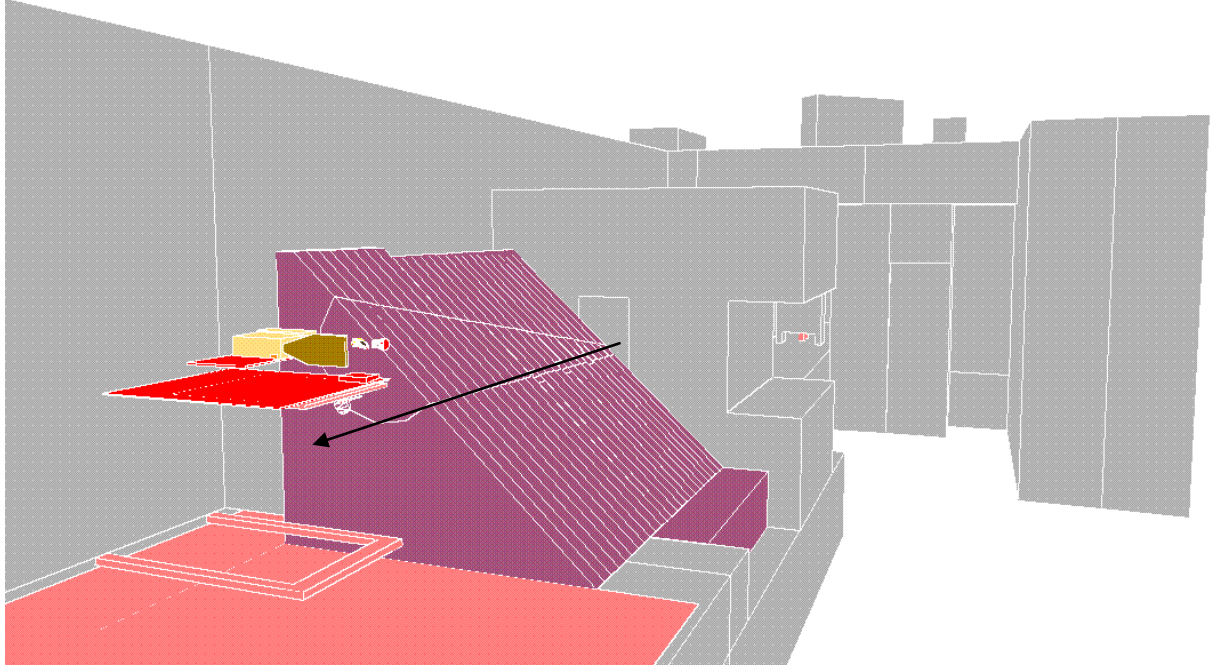


Figure 4.5: Cut through the cast iron block in order to show the biasing situation at side positions. The arrow shows the direction of the beam. Regions inside the cone have increased biasing importance. Parts of the construction, which would hide the view in the direction of the BGO were removed in this picture.

4.6.2. Simulation of energy deposition in the BGO crystal

The particles entering the BGO during the first run are loaded as primary particles in the second run. In this run, energy depositions, induced by each primary beam particle, are simulated by using the FLUKA input card “DETECT” [Fas99]. The result of this procedure is an energy dependent spectrum of counts, induced in the BGO (1024 energy dependent channels). The calculated spectrum is comparable with a real measurement taken with a BGO having constant energy resolution (see chapter 3.3.2.2). A cross section through the simulated BGO is shown in Figure 3.1. The shower, caused by a beam particle (already calculated in the first run), cannot produce more than one count. To take this into consideration one has to distinguish between a particle file, which was produced by an analog first run and a particle file, which was produced via a biased first run. In case of an analog first run, particles originating from the same primary particle have to be loaded together on the stack. This procedure guaranties that shower particles coming from the same primary beam particle cannot produce more than one entry in the histogram.

In case of a biased first run (no multi-events are expected) the particles have to be treated in the following way: The fact that each stored particle has different statistical weight has to be taken into account for the second run. A particle with a certain statistical weight has to be converted into a proper number of particles with a weight of 1.0. Therefore, higher weighted particles of the first run are converted into a larger number of particles, having a weight of 1.0, than lower weighted particles. With these

converted particles, the second run can be performed in a full analog mode. After the simulation of the energy deposition of each particle, the result (number of induced counts in the BGO crystal) has to be adapted to the number of primary beam particles and to the factor induced by the particle weight conversion. In order to get the number of counts per primary beam particle one has to divide the result of run 2 by the number of primary particles, times the multiplication factor induced by the weight adaptation. To clarify this procedure, we assume the following example: in the first run, the shower of three beam particles was calculated in biased mode. As result of this run a particle file is produced, which contains ten shower particles hitting the BGO. Four of them are calculated to have a statistical weight of 0.30, whereas the remaining six particles have a weight of 0.75. In the energy deposition run all particles with a weight of 0.3 are processed three times (weight multiplication with 10) and each particle of the second kind is processed seven times. For all particles of the second kind a statistical weight of 0.05 is still left and has also to be taken into consideration. The remaining weight of 0.05 of these particles gives another 6 particles of the second kind a 50 % chance to be started. The energy deposition run has to be done in a fully analog way (FLUKA card “DETECT” is used); therefore, all particles are given the weight 1.0. To obtain the entries in the histogram normalized to the number of real beam particles, the result has to be divided by 30 ($=3 \cdot 10$ (weight multiplication factor)).

4.6.3. Convoluting the BGO energy deposition spectrum with the BGO resolution function

The conversion from energy deposition into real BGO spectra was done with the method explained in Chapter 3.3.2.2. This technique takes the energy dependent resolution of the real measurement processes into account.

4.7. Calculated radiation conditions behind the different shielding constructions

4.7.1. Simulated fluences behind the shielding

The different particle fluences behind the simulated cast iron absorber, induced by a 40 or 120 GeV/c hadron beam, can be found in Figure 4.6 to 4.9. Photons and neutrons dominate the total fluence spectra. In general, close to the beam axis the photon fluence is much stronger than the one induced by neutrons. This difference is more distinct in case of higher primary beam energies and smaller iron wall depth. On the other hand the neutron fluence decreases in all situations more slowly with increasing distance to the beam axis. This leads to the following measurement situations: In “mid position” the number of photons entering the BGO is always more than a factor two higher than the comparable number of neutrons. At all “side positions” the situation is the opposite. The neutrons dominate the total fluences in a way that they add a two times higher contribution to the total fluence than all other particles together.

In general, the amount of other particles, emanated from the iron wall, is very small in comparison to the number of photons and neutrons. Only for the 200 cm iron wall set-up, irradiated by a 120 GeV/c hadron beam, all particle fluences are shown. In Figure 4.6 to 4.9 also electron fluences as a function of the distance to the beam axis are displayed. The decrease of this kind of fluence with increasing distance to the beam axis is even stronger than in the case of photons.

The behavior of the different fluences can be explained as follows: close to the beam axis high energy particle collisions occur. In these interactions π^0 's are produced, which decay into two γ 's. These two γ 's are the beginning of electromagnetic showers, which produce a huge amount of photons, electrons and positrons. Because of the lack of high energy particles in outer regions, the π^0 production fades with further distance to the hadronic shower axis (beam axis). Therefore, also the amount of photons, electrons and positrons decreases with increasing distance to the beam axis. The main reason that the electron fluences are in general much lower than the corresponding photon fluences can be found in a higher absorption probability for electrons than for photons in cast iron at low energies (< 10 MeV). Also the neutron-nucleus reactions, which produce gammas, increase the difference between the electron and photon fluences further. This effect is the dominating photon production process at the side measurement positions.

Neutrons are also mainly produced close to the beam axis. The survival probability of a particle, which undergoes a collision with an iron or carbon atom is much higher in case of a neutron than in case of a photon. Therefore, the weaker decrease of neutron fluences as a function of the distance to the beam axis is explainable.

Neutrons in the simulations were followed down to thermal energies. The transportation threshold for photons was set to 100 keV for analog runs and 200 keV for biased runs, respectively. The threshold of electrons and positrons were in general set to an energy of 200 keV.

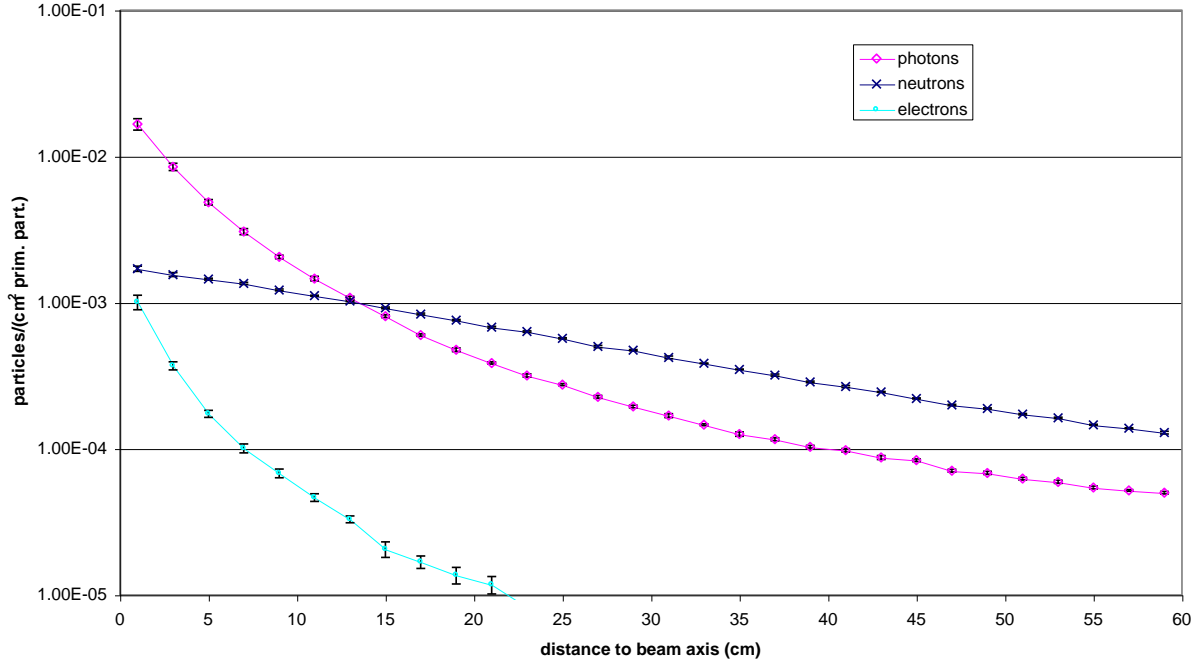


Figure 4.6: Fluences behind a 200 cm thick cast iron absorber, induced by the H6 hadron beam with a momentum of 40 GeV/c.

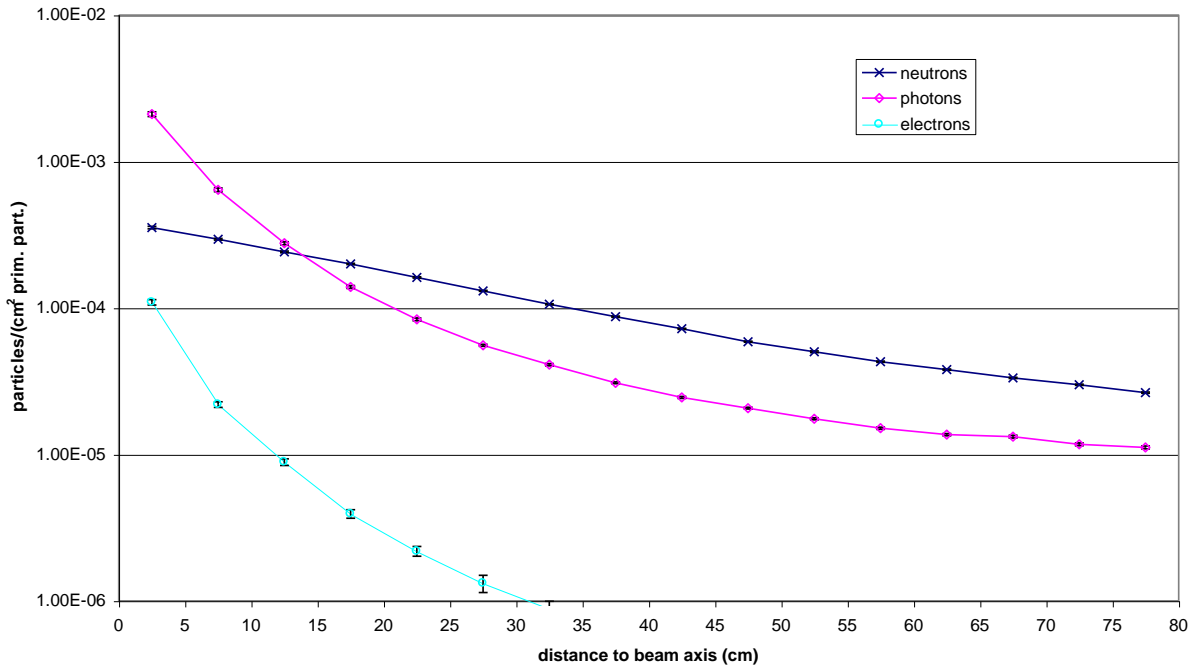


Figure 4.7: Fluences behind a 240 cm thick cast iron absorber, induced by the H6 hadron beam with a momentum of 40 GeV/c.

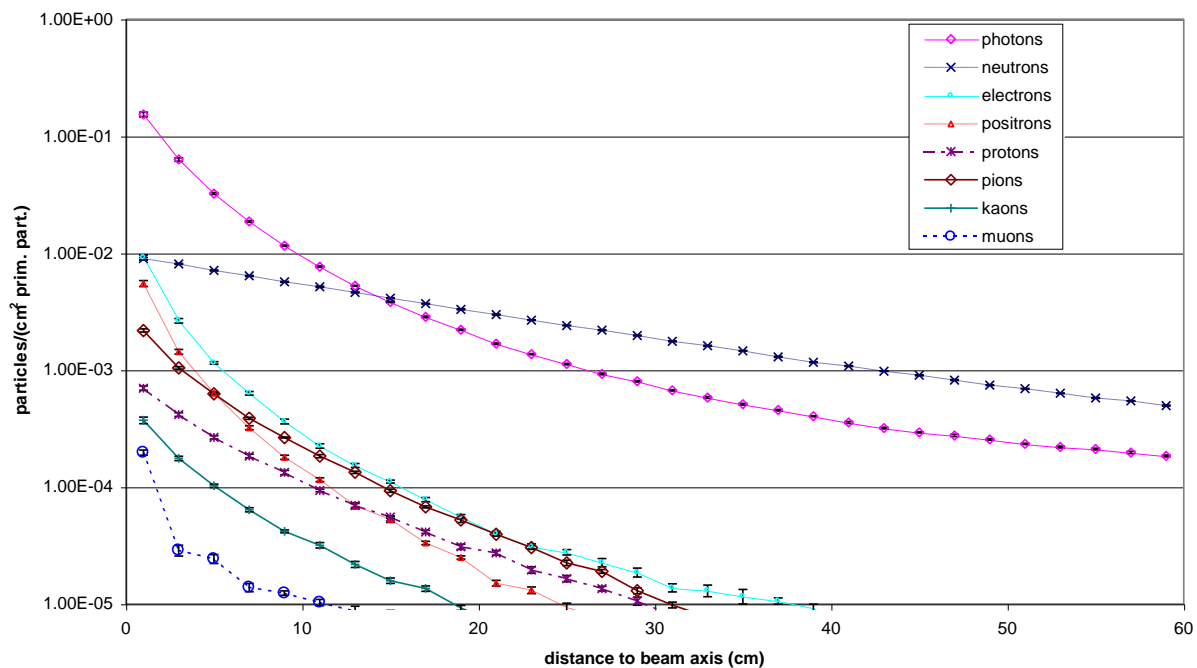


Figure 4.8: Fluences behind a 200 cm thick cast iron absorber, induced by the H6 hadron beam with a momentum of 120 GeV/c.

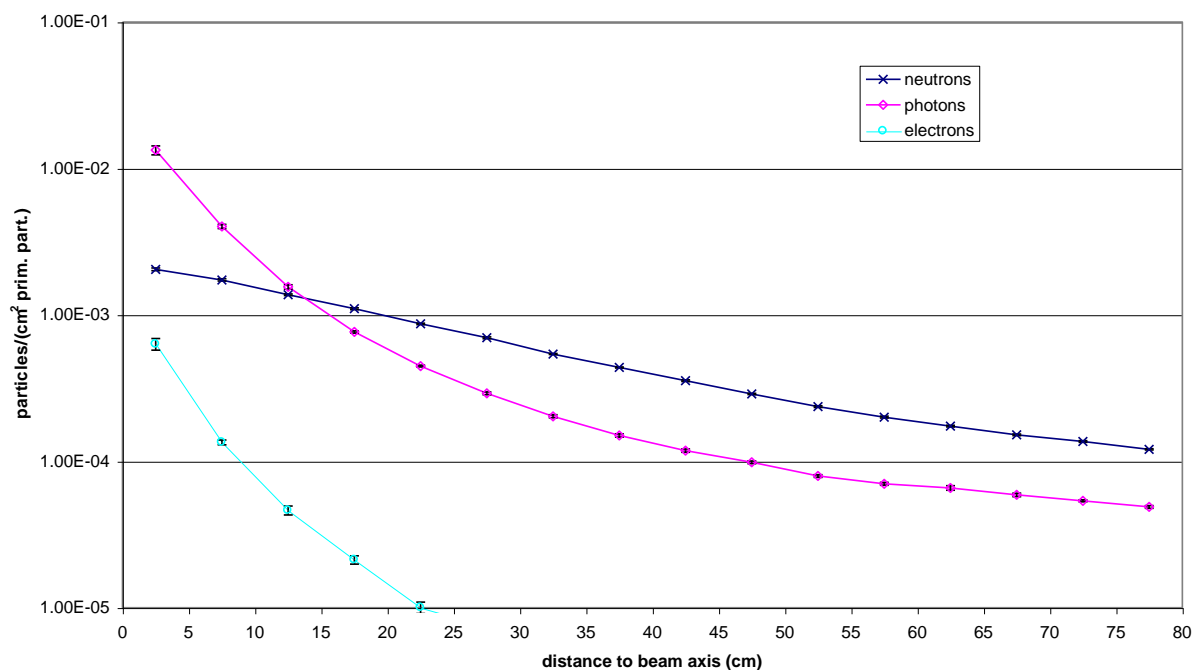


Figure 4.9: Fluences behind a 240 cm thick cast iron absorber, induced by the H6 hadron beam with a momentum of 120 GeV/c.

In order to describe the photon and neutron currents entering the BGO, the situation of “mid” and “side position” behind the 200 cm iron wall irradiated by the 40 GeV/c beam, is described in more detail. For this investigation the appropriate current spectra are shown in Figure 4.10 and 4.11. These figures show the photon and neutron currents, entering the BGO surroundings (aluminum cover of the crystal and connection between the PM and the crystal). The unit used to describe the particle fields yields the value “particles per primary particle and per MeV”. This way of presenting particle currents shows the particle density in dependence of the energy. The current density of all particles is, except for a few peaks, decreasing with increasing energy. In case of the simulated photons, two peaks are very significant. The first one, called annihilation peak, can be found at an energy of 511 keV. It is produced by a positron annihilation close to the BGO. Further details concerning this process can be found in Chapter 3.4.4. The second very significant gamma peak is produced via an absorption of mainly thermal neutrons in Fe-56. The subsequent (n, γ) process produces in the most cases a photon with an energy of 7631.18 or 7645.58 keV. FLUKA resolves these photons with a accuracy of 500 keV. This 500 keV window corresponds to the photon energy group number 8, which covers the energy range between 7.5 and 8.0 MeV. More details about the procedure concerning the production of neutron induced photons inside FLUKA, can also be found in Chapter 3.4.4 and in the Appendix A. This peak is very significant at all side positions. The reason for that fact can be explained with the domination of neutrons in total fluences in off-beam axis regions. At the mid position, this peak exists as well, but the part of photons produced by the EM showers, induced by π^0 decays, exceeds this effect.

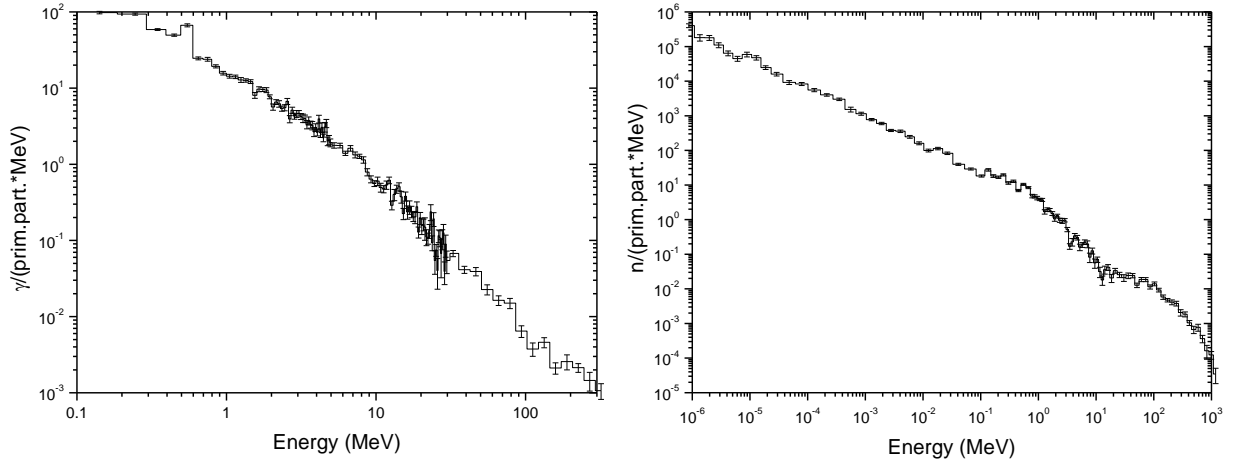


Figure 4.10: Photon (left) and neutron (right) current, entering the BGO surrounding material (aluminum cover of the crystal and connection between the PM and the crystal), located behind a 200 cm cast iron wall, which is irradiated by 40 GeV/c hadron beam. The BGO is mounted at “mid position”.

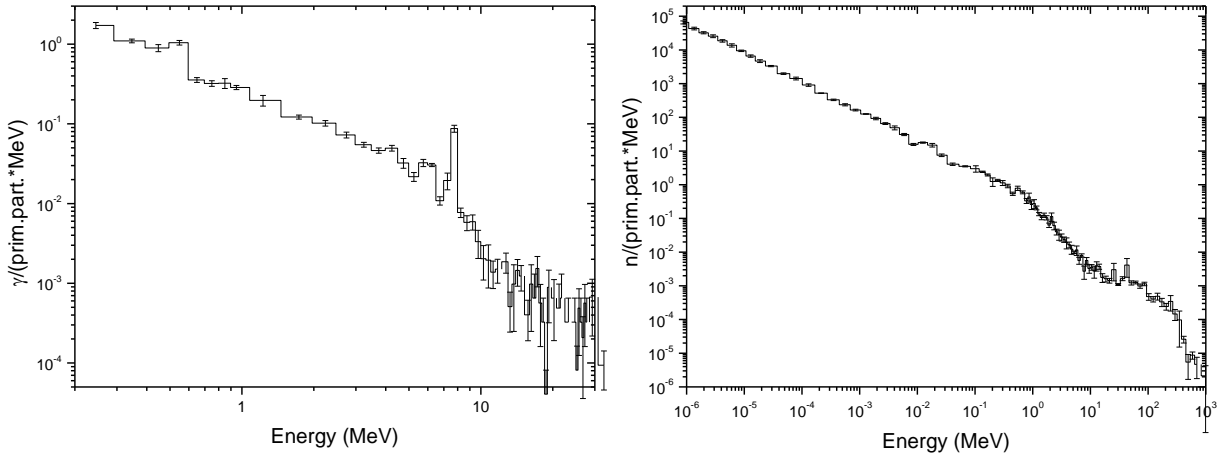


Figure 4.11: Photon (left) and neutron current (right) entering the BGO surrounding material (aluminum cover of the crystal and connection between the PM and the crystal), located behind a 200 cm cast iron wall, which is irradiated by a 40 GeV/c hadron beam. The BGO is mounted at “side position”.

Because of the logarithmic energy scale in Figure 4.10 and 4.11, one can very easily underestimate the contribution of high energy particles. In case, the particle density is strongly decreasing with increasing energy (e.g.: $1/E$), possible fluence structures in higher energy ranges become barely visible. Another possibility to display particle fluences are the so called “Lethargy plots”. These plots show on the ordinate the value $dN/d(\ln E)$ instead of dN/dE . Therefore, the above mentioned problems become less critical. In order to show more clearly why these kind of plots are more appropriate at higher energies, one has to express $dN/d(\ln E)$ in terms of dN/dE .

$$\frac{dN}{d(\ln E)} = \frac{dN}{dE} \cdot \frac{dE}{d(\ln E)} = \frac{dN}{dE} \cdot \frac{d(e^{\ln E})}{d(\ln E)} = \frac{dN}{dE} \cdot E \quad \text{Equation 4.1}$$

The factor E in Equation 4.1 explains why higher energy ranges become enhanced in the Lethargy plots compared to the particle current density plots. The same particle currents, as already shown in Figure 4.10 and 4.11, are pictured in Lethargy plot style in Figure 4.12 and 4.13.

Especially for the neutron situation at mid position, but also at side position, a broad peak with a maximum at about 90 MeV becomes visible. In the comparable neutron density plot, this circumstance can be only recognized as a shoulder without any structure. This peak is called “quasi-elastic peak” and its appearance can be seen as a convergence of two effects:

- 1) In most materials, the neutron total cross section reaches a minimum or a lower plateau at about 200 MeV. The cross section beyond this energy stays either at a constant level until around 1 GeV or it increases slightly.

- 2) The produced neutron spectrum, originating from high energy collisions, has a rapidly falling function of energy in this energy region.

The first observation means that the neutron attenuation length reaches a maximum at around 200 MeV. If we envisage neutrons entering an absorber then the fluence around 200 MeV is attenuated very little, compared with the fluence at e.g. 20 MeV. Both the neutron production and the total cross section of neutrons decrease up to an energy of 200 MeV. But at an energy range between about 50 and 100 MeV a very rapidly decrease of the cross section can be observed. This produces a peak or shoulder within that energy range¹. More details concerning this effect can be found in [Pra98].

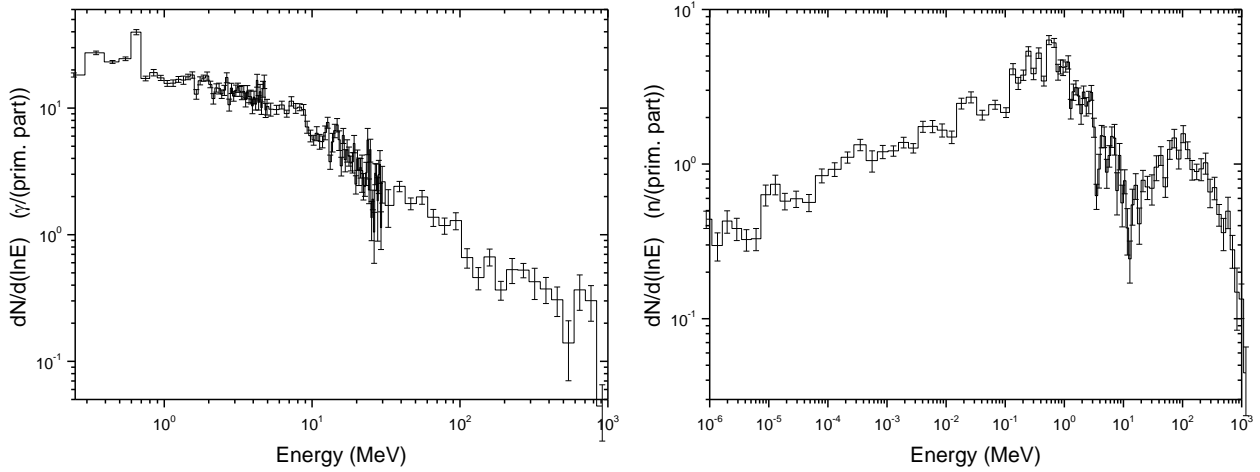


Figure 4.12: Photon (left) and neutron (right) Lethargy plot of the current, entering the BGO surrounding material (aluminum cover of the crystal and connection between the PM and the crystal), located behind a 200 cm cast iron wall, which is irradiated by a 40 GeV/c hadron beam. The BGO is mounted at “mid position”.

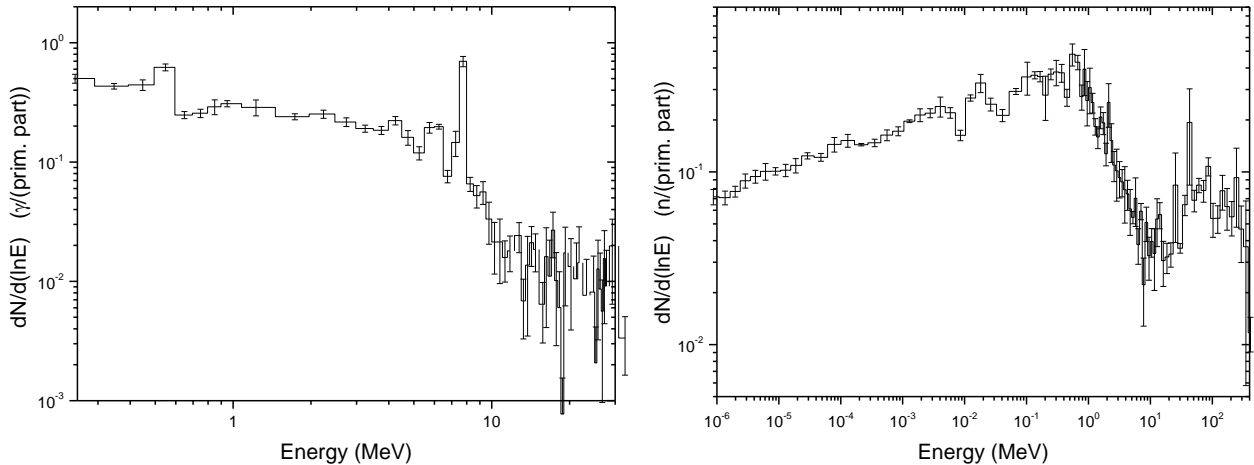


Figure 4.13: Photon (left) and neutron (right) Lethargy plot of the current, entering the BGO surrounding material (aluminum cover of the crystal and connection between the PM and the crystal), located behind a 200 cm cast iron wall, which is irradiated by a 40 GeV/c hadron beam. The BGO is mounted at “side position”.

¹ Private discussion with A. Ferrari, CERN SL Division

In order to get a better understanding which energy range provides the main contribution to the total current, an integration over the energy has to be performed. In Table 4.2 the comparison between the different particle current contributions can be found. For both positions, a comparison between integrated currents below and above 1 MeV is shown. Also the average energy of the particles, entering the BGO surroundings, is listed for photons and neutrons at mid and side position, located behind the 200 cm iron absorber. At the first glance it is quite astonishing that the average neutron energy, especially at mid position, is above 20 MeV. But, although the main part of the neutron current can be found below 1 MeV, the neutrons with energies close to 100 MeV and higher shift the average energy into such high ranges.

Table 4.2: Neutron and photon current (particle/prim. particle), including average particle energies, entering the BGO at mid and side position behind the iron block. The 200 cm iron wall is irradiated with a 40 GeV/c hadron beam.

Mid	<1 MeV	>1MeV	Total	Average energy
Neutrons	$21.5 \cdot 10^{-3}$	$7.8 \cdot 10^{-3}$	$29.4 \cdot 10^{-3}$	21.1 MeV
Photons	$60.6 \cdot 10^{-3}$	$17.5 \cdot 10^{-3}$	$78.1 \cdot 10^{-3}$	6.03 MeV
Side				
Neutrons	$2.71 \cdot 10^{-3}$	$0.49 \cdot 10^{-3}$	$3.20 \cdot 10^{-3}$	7.89 MeV
Photons	$1.05 \cdot 10^{-3}$	$0.02 \cdot 10^{-3}$	$1.07 \cdot 10^{-3}$	2.34 MeV

The integrated current contributions to the total photon and neutron fluxes, respectively, are shown in Figure 4.14 and 4.15. The threshold for photons in the simulation, dealing with the mid position scenario, was set to 100 keV. The comparable value for gammas, emitted at the side position, is set to 200 keV (biased mode). Hence, the figures, concerning the integrated photon currents, begin at these energies. Neutrons are simulated down to thermal energies and therefore the integrated values take also particles within these energy ranges into account. At the side position, around 99 % of all photons have an energy below 10 MeV. This agrees also with the fact that the main part of photons are produced by interactions, induced by neutrons below 20 MeV. These reactions produce hardly photons above 10 MeV. For the mid position scenario, around 10 % of the produced gammas have energies above 10 MeV. These photons originate mainly from π_0 decays and can reach therefore quite high energies.

About 60 % of the neutrons, entering the BGO at the side position, have energies below 100 keV. The comparable value for the mid position is found to be 40 %. In both cases, a quite strong contribution of neutrons with energies higher than 20 MeV can be found (mid: ~10 %, side: ~5 %). At the measurement position close to the beam axis, neutrons with energies of even several GeV occur.

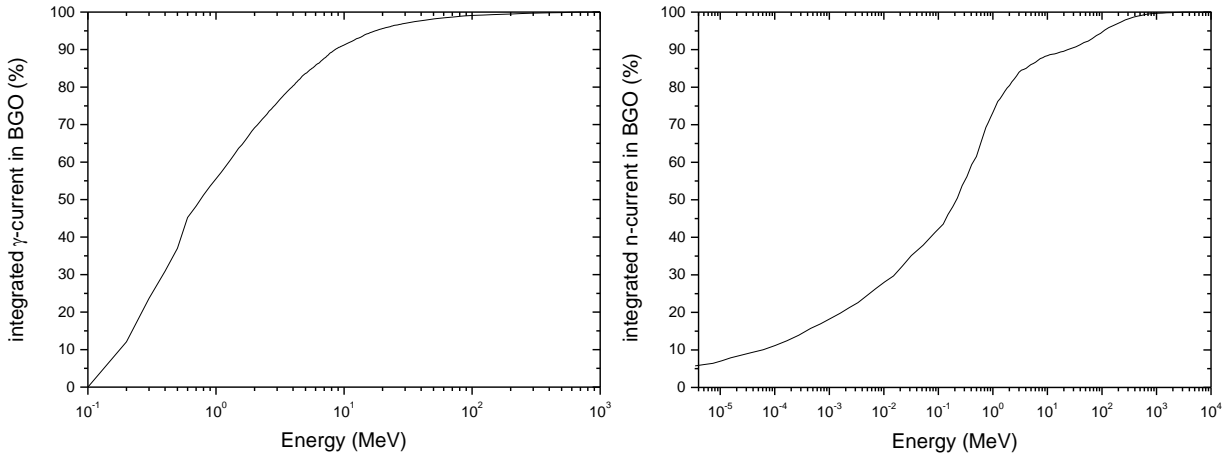


Figure 4.14: Relative integrated photon (left) and neutron current contribution (right) in %, entering the BGO surrounding material (aluminum cover of the crystal and connection between the PM and the crystal), located behind a 200cm cast iron wall, which is irradiated by a 40 GeV/c hadron beam. The BGO was mounted at “mid position”.

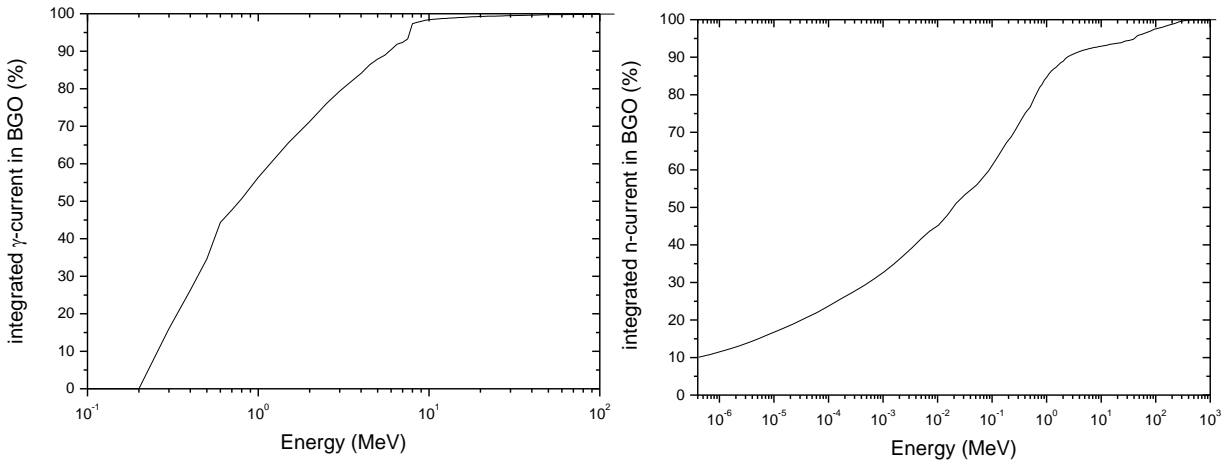


Figure 4.15: Relative integrated photon (left) and neutron current contribution (right) in %, entering the BGO surrounding material (aluminum cover of the crystal and connection between the PM and the crystal), located behind a 200 cm cast iron wall, which is irradiated by a 40 GeV/c hadron beam. The BGO was mounted at “side position”.

4.7.2. Characterization of events hitting the BGO

To characterize the radiation condition at the different measurement positions, one has also to investigate details concerning the number of particles which originate from the same primary beam particle and therefore enter the BGO together. At both positions, one can say that the main part of the primary beam particles do not induce an event. The reason why the number of particles hitting the BGO is critical for the final results is the following. The real BGO cannot resolve the number of particles entering the device together. The electronics coupled to the BGO sees only the sum of the energy deposition, which is induced in the crystal within a certain time window. In Figure 4.16, a classification concerning the events induced in the BGO at mid and side position is shown. The one concerning the mid position, shows a high “multi-event” rate. That means that very often several particles, originating from the same primary beam particle, hit the BGO at the same. It can even happen that more than 20 particles, mostly photons, enter the BGO together. The average number of particles, entering the BGO per event in mid position, is 2.6. The situation at the side position is completely different. Due to the lack of high energy collisions, followed by π^0 decays close to the BGO position, mostly single particle events occur. The average number of particles, entering the BGO per event in this situation is 1.05. This fact and the low reaction probability of the entering particles in BGO crystal ($\gamma \sim 40\%$, $n \sim 10\%$) justifies biased shower calculations at the side positions.

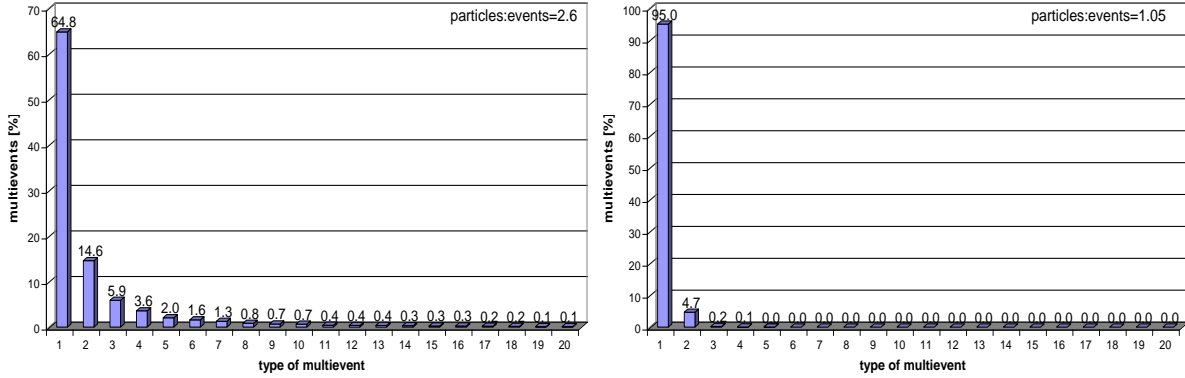


Figure 4.16: Classification of the events, hitting the BGO behind the 200 cm cast iron absorber in mid (left picture) and side (right picture) position. The momentum of the beam particles is 40 GeV/c.

In order to provide an overview of all simulated situations, the average number of particles entering the BGO per event, is listed in Table 4.3. At all mid positions, a high multi-event rate is found.

Table 4.3: Average number of particles per event hitting the BGO for the different measurement situations.

Situation	Particles per event	Situation	Particles per event
200-40-mid	2.59	200-120-side	1.09
200-40-side	1.05	240-120-mid	2.57
240-40-mid	2.05	240-120-side	1.05
240-40-side	1.06		

4.7.3. Hadronic origin of particles entering the BGO

In Table 4.4 the origin of photons and neutrons entering the BGO is shown. The first column describes the situation of photons behind the cast iron wall of 2m, which is irradiated by a 40 GeV/c hadron beam. The BGO is located in mid position. Almost 80 % of all photons entering the BGO originate from π^0 decays. The remaining 20 % are produced by neutron induced reactions or other inelastic hadronic interactions. The situation at the side position is different. Only 26 % of the γ 's have a π^0 decay origin. In comparison to the mid position, the π^0 production center is so far away that in the most cases not more than one γ , produced by this electromagnetic shower reaches the BGO. The main part of the photons originates from (n, γ) or (n,n', γ) reactions. The situation concerning the hadronic origin of the neutrons is in both cases similar. Neutrons behind the iron absorber are mainly produced by other, more high energy neutrons. Only the contribution of high energy pions, which produce neutrons, is significantly higher at the mid position than at the comparable side positions. The main reason for that can be found in the mostly forward directed production yield of high energy pions.

Table 4.4: Hadronic origin of photons entering the BGO behind the 200 cm cast iron absorber in mid and side position. The momentum of the beam particles is 40 GeV/c.

Particle type of mother particles	Photons		Neutrons	
	Mid position [%]	Side position [%]	Mid position [%]	Side position [%]
proton	0.6	0.6	6.1	4.2
neutron	10.7	67.6	65.7	82.1
pos. pion	4.5	1.8	9.7	4.2
neg. pion	3.4	1.7	16.0	8.3
pos. kaon	0.3	0.1	0.9	0.4
neutral pion	77.9	26.5	0.0	0.0
others	2.6	1.7	1.6	0.8

4.7.4. Induced counting rates and spectra in the BGO

The energy dependent spectra and the counting rate for the different scenarios can be obtained via the procedure explained in chapter 4.6. Figure 4.17 and 4.18 show the simulated BGO spectra in the mid and side position behind a 200 cm cast iron wall, which is irradiated by a 40 GeV/c hadron beam. In the mid position, the counting rate spectrum is divided into 3 main contributions. These influences consist of counts induced by pure γ multi events, pure neutron multi events and mixed multi events. The strongest influence on the counting rate is caused by the pure multi- γ events, followed by mixed events. In the mixed events, photons are very often accompanied by neutrons. The neutrons, entering the BGO cover or the PM window, have a less than 10 % probability to interact in the BGO crystal. This implies that the counts, induced by mixed multi events, are dominated by photon interactions. Also, the shape of the mixed event spectrum is very similar to the pure photon spectrum. The influence of pure neutron events on the counting rate in this position is less than 10 %.

To obtain the spectrum at the side position the biased method was used. Also the counts in this situation are mainly affected by γ events. But the influence of neutrons at this location is much stronger than in the mid position. Around 30 % of the counts are caused by pure neutron events. The influence of the mixed events is small in this position. These events are not shown in the picture, because biased calculations do not produce multi-events. In both figures the neutron induced counts add strong peaks to the whole spectrum. The main reason for this fact is that FLUKA uses cross sections, which only provide average neutron energy depositions. Therefore, these peaks show average energy deposition values, which can be found in the FLUKA neutron cross section data sets (see Appendix A). In the simulation, a down-scattered neutron, starting from a given energy group, always induces a fixed average energy deposition. This amount of energy is an average value over all possible energy depositions, caused by neutrons of this energy group. Peaks, which are induced by simulated neutrons in the energy range of the Am-Be spectrum are already explained in Chapter 3.4.4. But the situation for the H6 scenarios changes in two ways:

- 1) The energy distribution within 0 and 11.03 MeV (upper Am-Be energy) of the H6 spectra and the Am-Be spectrum are very different. Hence, the simulated peak structure changes with the different spectrum. Some significant peaks, induced by the simulated Am-Be spectrum, have only limited importance for the H6 situation. Also the other way around is valid. As an example of this fact, the peaks in the H6 spectrum having an energy of 3.724 and 7.448 MeV, respectively, have to be mentioned. The peak at 3.724 MeV originates from a simulated reaction of a thermal neutron (group 72) with a Germanium nucleus. This value reflects the average energy deposition induced by thermal neutrons in Germanium. After performing this energy deposition, the neutron is not necessarily killed. It has a certain probability to survive in the Monte Carlo procedure. In case it survives, it has again the same chance to induce the previous mentioned amount of energy deposit. The resulting total deposited energy, induced by this neutron is then 7.448 MeV. In contrast, Am-Be source very rarely contains thermal neutrons. Therefore, these peaks do not appear in the spectrum computed by the Am-Be simulations.

- 2) Neutrons with energies higher than 11.03 MeV are not emitted by an Am-Be source. However, the neutrons emanated behind the iron wall in H6 also include energies beyond this limit. Therefore, new peaks induced by these higher neutron energies, are found in the energy deposition spectra of the H6 scenarios. A few examples of peaks induced by particles with energies higher than 11.03 MeV are discussed in Table 4.5.

Table 4.5: Details of simulated energy peaks induced by neutrons with energies above 11.03 MeV.

Deposited energy	Material	E_{\min} of neutron energy bin	E_{\max} of neutron energy bin	Neutron group number
MeV		MeV	MeV	
4.680	Ge	17.5	19.6	2
4.146	Ge	12.214	13.499	4
2.371	O	17.5	19.6	1
1.722 – 1.786	O	10.0	17.5	2 - 6

More details about the used method, regarding the simulation of low energy neutrons inside FLUKA, can be found in Chapter 3.4.4 and in Appendix A.

The accurate numbers concerning the contributions of the different multi events to the final counting rate in the situations 200cm-40GeV/c side and mid, can be found in Table 4.6. As already mentioned, the main influence on the counting rates come in both scenarios from photons. Pure particle events, which do not contain photons or neutrons, rarely exist by themselves. This corresponds also very well with the simulated fluences at the two measurement positions.

Table 4.6: Split counting rates of situations behind 200 cm iron, irradiated by 40GeV/c.

	Mid position	Side position
	%	%
Photon	54	63
Neutron	9	31
Mixed	36	6
others	< 1	< 0.1

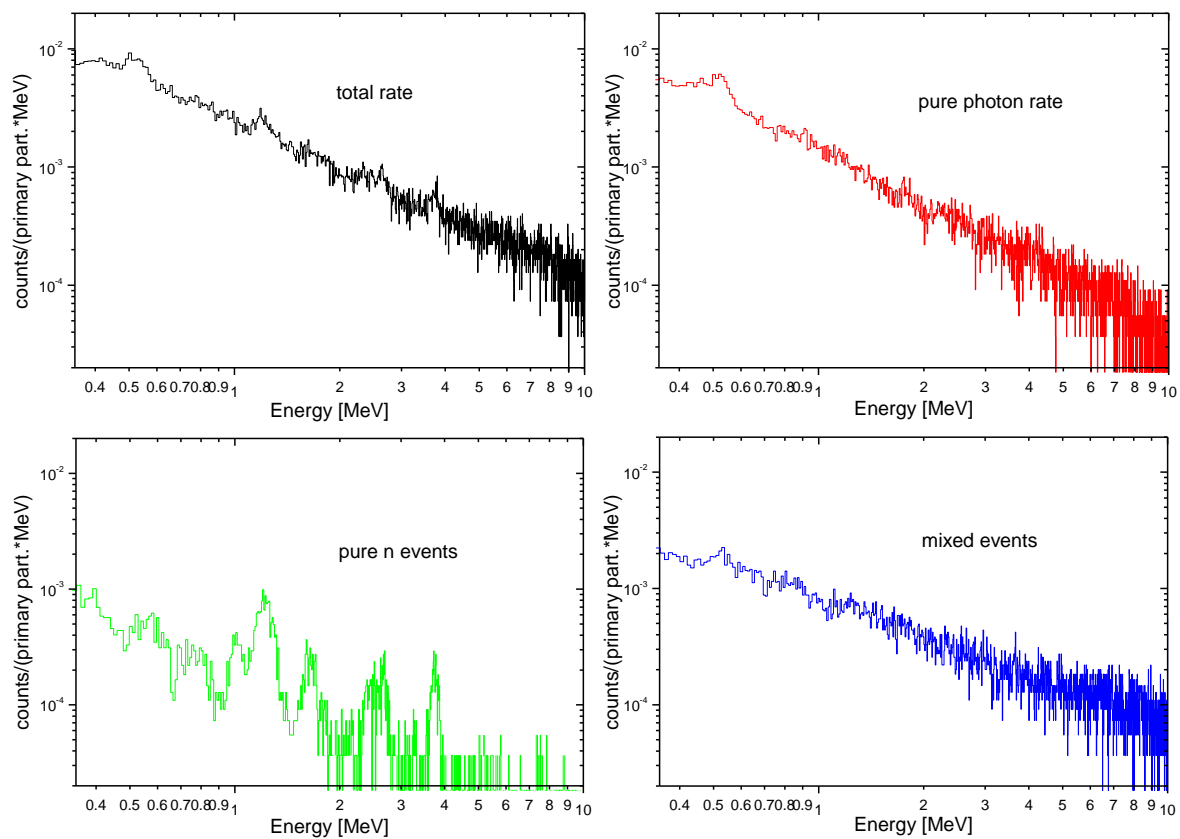


Figure 4.17: Different counting rates of the set-up "200cm 40GeV mid"

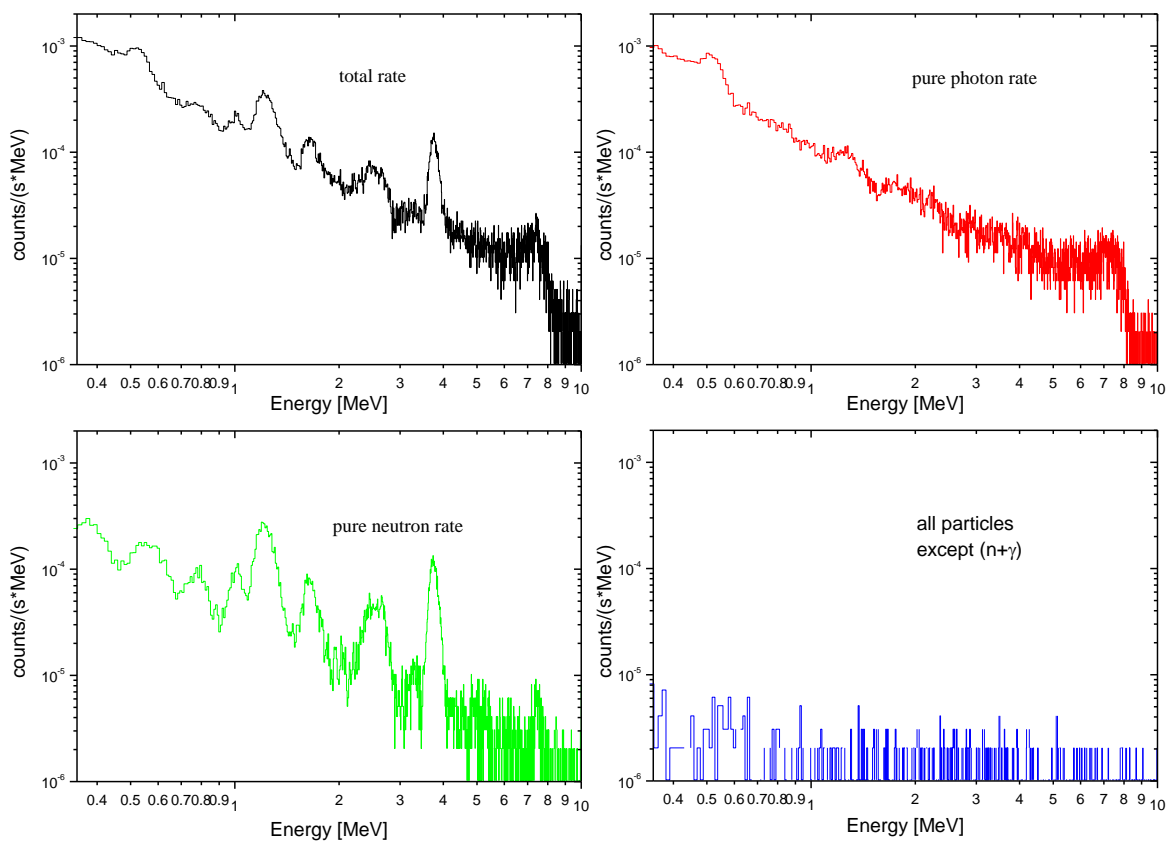


Figure 4.18: Different counting rates of the set-up "200cm 40GeV side"

4.8. Assessment of the systematic uncertainties of the measurements

The systematic uncertainty concerning the comparison between the simulation and the measurement has two contributions:

1. Systematic uncertainties which can be accessed with measurement results.
2. Systematic uncertainties which can be accessed only via simulation results.

In this thesis only the second point will be discussed. Information about the first contribution can be found in [Gsc00].

The systematic uncertainties, which are discussed in this section, are induced by limited knowledge of the following parameters:

1. Distance between beam axis and BGO crystal.
2. Carbon contents of the iron absorber.
3. Composition of the primary hadron beam.
4. Size of the BGO.
5. Depth of the iron absorber.
6. Absorber density.
7. Distance between BGO and iron absorber.

It should be mentioned that this chapter has to be seen rather as an assessment of the influences of different experimental parameters to the BGO counting rate. It is not an evaluation of the systematic uncertainties.

4.8.1. Variable distance between beam and BGO crystal

For a calculation of this uncertainty contribution, we have to discuss two different scenarios:

1. The first one deals with the situations, where the BGO crystal is located close to the beam axis. At these BGO positions, the fluence of the particles cannot be considered having a linear dependency on the distance. Furthermore, the multi-event rate is increasing in a non linear way with decreasing distance to the beam axis. Therefore, the counting rate is not directly coupled to the fluence rate. The only way to calculate the uncertainty in this case, is to run additional FLUKA calculations with variable distances between the BGO and the beam axis.
2. The second kind of scenarios deals with situations where the distance between beam and BGO crystal is sufficiently large ($>56\text{cm}$) to survey the fluence for calculating the systematic uncertainties. In this case, the multi-event rate is close to one and does not vary over the range of the BGO crystal. Therefore, the fluences and the BGO counting rates are directly coupled to each other.

4.8.1.1. Uncertainty evaluation for mid positions:

For an uncertainty calculation concerning the mid situations, simulations were performed where the distance between BGO and beam was varied by 1.0 cm in horizontal and vertical direction. The value of 1.0 cm can be seen as the horizontal and vertical measurement uncertainty, concerning the distance between the BGO and the beam axis. In order to assess a systematic uncertainty, which is induced by this variation, we have to take also the statistical uncertainties of the additional runs into account. The uncertainties of the results, concerning the ± 1.0 cm situations establish a range around the calculated nominal counting rate. This range is seen as the 1σ uncertainty, induced by a variation of 1.0 cm in horizontal and vertical direction. The counting rates, which are needed for the uncertainty calculation, are listed in Table 4.7.

Table 4.7: BGO counting rates as a function of the distance to the beam axis. The values of all three scenarios, including their statistical uncertainties, are listed.

	$\Delta(x,y) = (+1,+1)$		Nominal position		$\Delta(x,y) = (-1,-1)$	
	Value	$\Delta \%$	Value	$\Delta \%$	Value	$\Delta \%$
40 GeV/c						
200 cm	$62.5 \cdot 10^{-4}$	4.5	$71.8 \cdot 10^{-4}$	1.6	$66.4 \cdot 10^{-4}$	3.0
240 cm	$14.3 \cdot 10^{-4}$	6.2	$15.7 \cdot 10^{-4}$	3.4	$17.2 \cdot 10^{-4}$	4.9
120 GeV/c						
240 cm	$71.2 \cdot 10^{-4}$	4.4	$78.6 \cdot 10^{-4}$	2.8	$80.2 \cdot 10^{-4}$	4.6

The low increase of the rate at “240cm 120GeV/c mid” and the decrease at “200cm 40GeV/c mid” with the BGO closer to the beam axis can be explained with the behavior of the multi-event rate. This value increases strongly with decreasing distance to the beam axis. As an example, the γ multi-event situation at “200 cm 40 GeV/c mid” can be found in Table 4.8. The increase of the number of γ 's in the multi-events is stronger than the increase of the pertinent fluences. Therefore, a lower counting rate at closer distance to the beam axis is understandable.

Table 4.8: Photon multi event situation at the situation “200 cm 40 GeV/c mid”.

	$\Delta(x,y) = (+1,+1)$	Nominal position	$\Delta(x,y) = (-1,-1)$
Average γ multi event rate	2.71	3.23	4.14

With the values of Table 4.7 the uncertainty range around the nominal values can be assessed via the explained method. The minimal and maximal results, induced by a distance variation of 1.0 cm, can be found in Table 4.9. The uncertainties of the nominal counting rates are listed in Table 4.10.

Table 4.9: Utmost range of the counting rate induced by the discussed distance variation.

	$\Delta(x,y) = (+1,+1)$	$\Delta(x,y) = (-1,-1)$
	%	%
40 GeV/c		
200 cm	$59.7 \cdot 10^{-4}$	$68.4 \cdot 10^{-4}$
240 cm	$13.4 \cdot 10^{-4}$	$18.0 \cdot 10^{-4}$
120 GeV/c		
240 cm	$68.3 \cdot 10^{-4}$	$83.9 \cdot 10^{-4}$

Table 4.10: Uncertainty of the nominal counting rate induced by the discussed distance variation.

	$\Delta(x,y) = (+1,+1)$	$\Delta(x,y) = (-1,-1)$
	%	%
40 GeV/c		
200 cm	-16.8	-4.6
240 cm	-14.6	+14.6
120 GeV/c		
240 cm	-13.2	+6.7

4.8.1.2. Uncertainties for side positions

To evaluate the uncertainties for the side situations, the investigation of the fluence in dependence of the distance is sufficient. The influence of the fluences to the rate in the BGO can be calculated via the separated rate results, which are induced by pure γ -events, pure n_0 -events and mixed events. For the uncertainties induced by mixed events, the particles were treated like γ 's, because the γ 's dominate the induced BGO counting rate in these situations. Therefore, with the knowledge of the variation concerning the different fluence contributions and the knowledge of the counting rate contributions, one can calculate the uncertainty with Equation 4.2.

$$\Delta rate = \sum_i \frac{\Delta fl_i}{fl_i} \cdot C_i \quad \text{Equation 4.2}$$

Δfl_i Variation of single fluence
 fl_i Single fluence
 C_i Individual counting rate induced by this fluence

For the evaluation of the influence of the distance variation to the γ and n fluences (see Figure 4.6 – 4.9), a polynomial fit through three points around the BGO position was performed. The fit procedure (x in cm) yields the following results:

200cm 40GeV/c side:

$$\begin{aligned}\gamma: & \text{fluence} = 3.8119 \cdot 10^{-4} - 1.048 \cdot 10^{-5} \cdot x + 8.25 \cdot 10^{-8} \cdot x^2 \\ n: & \text{fluence} = -1.4894 \cdot 10^{-4} + 1.43 \cdot 10^{-5} \cdot x - 1.625 \cdot 10^{-7} \cdot x^2\end{aligned}$$

200cm 120GeV/c side:

$$\begin{aligned}\gamma: & \text{fluence} = 7.4185 \cdot 10^{-4} - 1.24 \cdot 10^{-5} \cdot x + 5.0 \cdot 10^{-8} \cdot x^2 \\ n: & \text{fluence} = -4.5 \cdot 10^{-3} + 1.968 \cdot 10^{-4} \cdot x - 1.9 \cdot 10^{-6} \cdot x^2\end{aligned}$$

240cm 120GeV/c side

$$\begin{aligned}\gamma: & \text{fluence} = 4.6864 \cdot 10^{-4} - 1.2496 \cdot 10^{-5} \cdot x + 9.68 \cdot 10^{-8} \cdot x^2 \\ n: & \text{fluence} = 1.19 \cdot 10^{-3} + 2.808 \cdot 10^{-5} \cdot x - 1.9 \cdot 10^{-7} \cdot x^2\end{aligned}$$

240cm 40GeV/c side

$$\begin{aligned}\gamma: & \text{fluence} = 9.94525 \cdot 10^{-5} - 2.548 \cdot 10^{-6} \cdot x + 1.88 \cdot 10^{-8} \cdot x^2 \\ n: & \text{fluence} = 2.63681 \cdot 10^{-4} - 6.45 \cdot 10^{-6} \cdot x + 4.54 \cdot 10^{-8} \cdot x^2\end{aligned}$$

These equations are only valid close to the BGO position. In all four cases the gradient of these curves at 57 cm (for the 200 cm situations) and at 57.5 cm (for the 240 cm situations), respectively has to be evaluated. The uncertainty concerning the distance to the beam axis is assumed to be 1.5 cm. The resulting fluence variations for all side situations can be found in Table 4.11.

Table 4.11: Fluence variations induced by distance variations (BGO–beam) of 1.5 cm.

	$\Delta\gamma$	Δn
	%	%
40 GeV/c		
200 cm	± 3.2	± 4.7
240 cm	± 3.9	± 4.4
120 GeV/c		
200 cm	± 5.1	± 5.4
240 cm	± 3.0	± 4.7

In all four cases, the ratio between the photon-induced rate and the neutron-induced rate is very close to 2:1. The consecutive uncertainties of the total counting rates, which were calculated by using Equation 4.2, are shown in Table 4.12.

Table 4.12: Uncertainties of the total counting rates induced by a BGO distance variation (1.5 cm) to the beam axis.

	40 GeV/c		120 GeV/c	
	200 cm	240 cm	200 cm	240 cm
Uncertainty (%)	3.7	4.1	5.2	3.6

4.8.2. Influence of the carbon contents in the iron absorber

The composition of the cast iron block, which is hit by the hadron beam and which is therefore responsible for all shower processes inducing the counts in the BGO, is also an important issue of the systematic uncertainty. The nominal composition of the cast iron absorber is stated in Table 4.13

Table 4.13: Nominal cast iron composition.

	Fe	C
wt-%	95	5

For the determination of a systematic uncertainty, induced by a variation of the carbon contents in the absorber, FLUKA runs with both 4 and 6 wt-% C contents were performed. Finally, the different fluences in the range of the BGO regions are compared in order to calculate the influence of variable carbon contents in the absorber. The fact that the average number of particles in the multi-events does not vary with the Carbon contents of the used iron, justifies the comparison between the different fluences also in the mid-positions. The multi events are mainly produced by π^0 decays. These particles are produced in high energy collisions (> 200 MeV), which can be described as particle-nucleon collisions. For the incoming high energy particle, the nuclei are seen as a compound of almost free nucleons. Therefore, the macroscopic cross section for a π^0 production is only dependent on the number of nucleons per cm^3 and independent from the actual nucleus. At the side position almost no multi-events occur. Hence, a comparison of the fluences concerning the side positions is justified as well.

To asses a systematic fluence uncertainty, which is induced by the variation of the carbon contents, we have to take also the statistical uncertainties concerning these variation-runs into account. The statistical uncertainties of the two runs cover a range, of a plausible variation of the carbon contents in the absorber. The impact of the single fluences on the BGO-rate can be calculated via separated runs for pure γ -events, pure n_0 -events and mixed events. For the uncertainty calculation, the mixed events are treated like γ 's, because the γ 's in these events dominate the counting rate in the BGO. The procedure is similar to the one already applied in the previous subchapter. The fluences behind the different iron absorber at the range of the BGO crystal are listed for the different carbon contents in Table 4.14.

Table 4.14: Fluences at BGO position as a function of the carbon contents.

	94Fe6C		95Fe5C		96Fe4C	
	Part./cm ²	Δ %	Part./cm ²	Δ %	Part./cm ²	Δ %
200cm 40GeV/c mid						
γ	$3.02 \cdot 10^{-3}$	8.7	$3.06 \cdot 10^{-3}$	4.7	$3.01 \cdot 10^{-3}$	5.3
n	$1.25 \cdot 10^{-3}$	1.4	$1.35 \cdot 10^{-3}$	1.6	$1.36 \cdot 10^{-3}$	1.9
240cm 40GeV/c mid						
γ	$6.21 \cdot 10^{-4}$	7.6	$6.41 \cdot 10^{-4}$	2.9	$6.03 \cdot 10^{-4}$	11.2
n	$2.72 \cdot 10^{-4}$	2.5	$2.95 \cdot 10^{-4}$	1.2	$3.10 \cdot 10^{-4}$	6.5
240cm 120GeV/c mid						
γ	$4.21 \cdot 10^{-3}$	4.6	$4.01 \cdot 10^{-3}$	3.2	$4.10 \cdot 10^{-3}$	2.9
n	$1.65 \cdot 10^{-3}$	2.1	$1.73 \cdot 10^{-3}$	1.8	$1.77 \cdot 10^{-3}$	1.8
200cm 40GeV/c side						
γ	$4.90 \cdot 10^{-5}$	4.7	$5.19 \cdot 10^{-5}$	1.3	$5.33 \cdot 10^{-5}$	1.5
n	$1.25 \cdot 10^{-4}$	1.3	$1.38 \cdot 10^{-4}$	0.9	$1.58 \cdot 10^{-4}$	1.7
240cm 40GeV/c side						
γ	$1.59 \cdot 10^{-5}$	5.9	$1.51 \cdot 10^{-5}$	1.9	$1.61 \cdot 10^{-5}$	6.9
n	$3.79 \cdot 10^{-5}$	4.1	$4.29 \cdot 10^{-5}$	0.9	$4.75 \cdot 10^{-5}$	1.4
240cm 120GeV/c side						
γ	$6.35 \cdot 10^{-5}$	1.3	$7.02 \cdot 10^{-5}$	2.3	$7.85 \cdot 10^{-5}$	3.8
n	$1.83 \cdot 10^{-4}$	0.9	$2.00 \cdot 10^{-4}$	1.4	$2.16 \cdot 10^{-4}$	0.9
200cm 120GeV/c side						
γ	$1.89 \cdot 10^{-4}$	3.8	$1.97 \cdot 10^{-4}$	2.3	$2.10 \cdot 10^{-4}$	1.3
n	$4.90 \cdot 10^{-4}$	0.9	$5.44 \cdot 10^{-4}$	1.4	$5.95 \cdot 10^{-4}$	0.9

With Table 4.14 the systematic uncertainty of the different fluences can be evaluated. In Table 4.15 the fluence uncertainties of all situations are listed.

Table 4.15: Systematic fluence uncertainties induced by a variation of the carbon contents within 4 and 6 wt-%.

	200cm 40GeV/c mid		240cm 40GeV/c mid		240cm 120GeV/c mid		200cm 120GeV/c side	
	94Fe6C	96Fe4C	94Fe6C	96Fe4C	94Fe6C	96Fe4C	94Fe6C	96Fe4C
γ	-9.8%	+7.2%	-16.5%	+4.7%	-0.7%	+9.7%	-7.6%	+8.1%
n	-8.9%	+3.0%	-10.2%	+5.1%	-6.9%	+4.0%	-10.7%	+10.3%
	200cm 40GeV/c side		240cm 40GeV/c side		240cm 120GeV/c side			
	94Fe6C	96Fe4C	94Fe6C	96Fe4C	94Fe6C	96Fe4C		
γ	-10.0%	+5.2%	-0.7%	+13.9%	-10.7%	+16.1%		
n	-10.9%	+16.7%	-15.4%	+6.6%	-9.5%	+9.0%		

The necessary counting rate contributions of the different kinds of particles are listed in Table 4.16.

Table 4.16: Counting rate contributions of photon, neutron and mixed events.

γ (%)	n (%)	mix (%)
200cm 40GeV/c mid		
54.6	9.0	36.4
240cm 40GeV/c mid		
58.9	11.4	29.7
240cm 120GeV/c mid		
47.2	10.2	42.6
all side positions		
(γ+mix):n = 2:1		

By applying the values in Table 4.16 and 4.15 to Equation 4.2 the systematic uncertainties concerning a variation of the carbon contents in iron is obtained. The calculated values for all situations are listed in Table 4.17

Table 4.17: Evaluated uncertainties induced by a carbon variation of ± 1 wt-%.

200cm 40GeV/c mid		240cm 40GeV/c mid		240cm 120GeV/c mid		200cm 40GeV/c side	
94Fe6C	96Fe4C	94Fe6C	96Fe4C	94Fe6C	96Fe4C	94Fe6C	96Fe4C
-11.2	+7.9	-15.8	+4.8	-1.3	+9.1	-10.4	+8.9
		240cm 40GeV/c side		240cm 120GeV/c side		200cm 120GeV/c side	
		94Fe6C	96Fe4C	94Fe6C	96Fe4C	94Fe6C	96Fe4C
		-5.6	+11.5	-10.3	+13.7	-8.6	+8.8

4.8.3. Influence of the composition of the primary hadron beam

During our measurements we dealt with two primary hadron beams with different momentum and particle composition, respectively. The values concerning momentum and particle composition of the two hadron beams are listed in Table 4.18.

Table 4.18: Momentum and particle composition of the used primary beam compositions.

40 GeV/c			120 GeV/c		
π^+	Protons	K^+	π^+	Protons	K^+
84.9	12.2	2.9	60.7	34.8	4.5

The rate uncertainties, induced by a limited knowledge of the beam composition were calculated in the following way:

40 GeV/c: The necessary ratios between p/π^+ and K^+/p , including the measured uncertainties can be found in [Amb99]. The uncertainties of both ratios were increased to 3 % in order to cover inaccuracies of the beam compositions in the

simulation. For example: At the time the calculations were performed, the ratio between protons and pions was not better known than 0.12 (instead of 0.1188). In case of a variation concerning the particle ratios, we obtain the compositions stated in Table 4.19.

120 GeV/c: This case is not covered by [Amb99]. The ratio between protons and pions was obtained from². It is a calculated value and no uncertainties were quoted. The value of this ratio fits very well the shape of the energy dependent p/π^+ curve, obtained by [Amb99]. Also the ratio between kaons and protons were obtained by interpolation of data taken from [Amb99]. For the uncertainties of these values, the uncertainties from the ratios at 135 GeV/c were taken and increased as follows. The uncertainty for the ratio p/π^+ was increased from 1.4% to 2%. The fact that the value for the K^+/p ratio was obtained by interpolation, made an increase of this value from 1.8 to 3 % necessary. In case of a variation concerning the particle ratios, we obtain the compositions stated in Table 4.19.

Table 4.19: Beam composition as a function of the different ratio variations.

Variation of different ratios	40 GeV/c			Variation of different ratios	120 GeV/c		
	π^+	Protons	K^+		π^+	Protons	K^+
$p/\pi^+ -3\%$	85.23	11.88	2.89	$p/\pi^+ -2\%$	61.19	34.39	4.42
$p/\pi^+ +3\%$	84.45	12.50	3.05	$p/\pi^+ +2\%$	60.24	35.24	4.53
$K^+/p -3\%$	84.86	12.20	2.94	$K^+/p -3\%$	60.79	34.86	4.34
$K^+/p +3\%$	84.71	12.17	3.12	$K^+/p +3\%$	60.63	34.77	4.60

In order to obtain the influence of the beam composition variation, separated runs containing only pions, protons and kaons were performed. Each of these runs yields a neutron and gamma fluence distribution, which depends on the distance to the beam axis.

To calculate the different fluences obtained by a certain beam composition, Equation 4.3 has to be applied:

$$fluence_i = \pi_r \cdot \pi_{fli} + p_r \cdot p_{fli} + K_r \cdot K_{fli} \quad \text{Equation 4.3}$$

$fluence_i$...	Neutron or photon fluence
π_r ...	Ratio of pions in hadron beam
K_r ...	Ratio of kaons in hadron beam
p_r ...	Ratio of protons in hadron beam
π_{fli} ...	Neutron or photon fluence induced by pions
K_{fli} ...	Neutron or photon fluence induced by kaons
p_{fli} ...	Neutron or photon fluence induced by protons

² Private discussion with Konrad Elsner, CERN SL Division

With Equation 4.3 the alteration of the fluences induced by different beam compositions can be calculated. The fact that the received counting rate in the BGO is composed of counts induced by photons, counts induced by neutrons and of counts induced by a mixture of particles hitting the BGO together, allows to use Equation 4.4 for the calculation of the counting rate uncertainties. The necessary values concerning the different counting rates can be found in Table 4.16. The fact that the different fluences are correlated with each other implies rather a linear than a quadratic uncertainty summation.

$$\sigma \text{ rate} = \sum_i \frac{\sigma fl_i}{fl_{nom i}} \cdot rate_i \quad \text{Equation 4.4}$$

$rate_i$... BGO rate induced by particle sort i (gamma, neutron and mixed events)

σfl_i ... Fluence uncertainty, induced by variation of the beam contents

$fl_{nom i}$... Nominal photon or neutron fluence

Because of the domination of gamma reactions in case of mixed events, this part of the uncertainty is calculated with the uncertainty of the gamma fluence. In Table 4.20 the different, primary particle dependent fluences of all situations can be found. With these fluences, the fluence for variable beam compositions can be determined.

Table 4.20: Photon and neutron fluence behind the iron shielding (at BGO position) as a function of the primary beam particles. The listed uncertainty is the statistical uncertainty of the single runs.

Prim. particles	γ fluence	Δ %	n_0 fluence	Δ %
200cm 40GeV/c mid				
K^+	$7.05 \cdot 10^{-3}$	3.1	$2.51 \cdot 10^{-3}$	2.5
π^+	$3.19 \cdot 10^{-3}$	4.3	$1.35 \cdot 10^{-3}$	1.0
Proton	$1.57 \cdot 10^{-3}$	4.2	$1.04 \cdot 10^{-3}$	2.1
200cm 40GeV/c side				
K^+	$8.95 \cdot 10^{-5}$	3.7	$2.10 \cdot 10^{-4}$	2.9
π^+	$5.31 \cdot 10^{-5}$	2.5	$1.32 \cdot 10^{-4}$	1.9
Proton	$4.88 \cdot 10^{-5}$	3.1	$1.33 \cdot 10^{-4}$	1.33
240cm 40GeV/c mid				
K^+	$1.84 \cdot 10^{-3}$	7.6	$7.34 \cdot 10^{-4}$	5.0
π^+	$7.65 \cdot 10^{-4}$	12.7	$3.35 \cdot 10^{-4}$	6.6
Proton	$2.20 \cdot 10^{-4}$	6.6	$2.29 \cdot 10^{-4}$	3.4
240cm 40GeV/c side				
K^+	$3.13 \cdot 10^{-5}$	5.9	$7.79 \cdot 10^{-5}$	2.5
π^+	$1.43 \cdot 10^{-5}$	9.0	$3.78 \cdot 10^{-5}$	7.0
Proton	$1.39 \cdot 10^{-5}$	3.9	$4.20 \cdot 10^{-5}$	1.5
240cm 120GeV/c mid				
K^+	$9.58 \cdot 10^{-3}$	5.4	$3.59 \cdot 10^{-3}$	1.1
π^+	$4.87 \cdot 10^{-3}$	10.0	$2.05 \cdot 10^{-3}$	5.3
Proton	$2.97 \cdot 10^{-3}$	7.5	$1.45 \cdot 10^{-3}$	1.5
240cm 120GeV/c side				
K^+	$1.45 \cdot 10^{-4}$	3.3	$3.45 \cdot 10^{-4}$	0.9
π^+	$8.65 \cdot 10^{-5}$	7.4	$2.34 \cdot 10^{-4}$	5.4
Proton	$7.50 \cdot 10^{-5}$	6.1	$1.95 \cdot 10^{-4}$	1.5
200cm 120GeV/c side				
K^+	$3.38 \cdot 10^{-4}$	4.5	$7.44 \cdot 10^{-4}$	2.1
π^+	$2.00 \cdot 10^{-4}$	5.9	$5.03 \cdot 10^{-4}$	3.0
Proton	$1.74 \cdot 10^{-4}$	4.9	$3.84 \cdot 10^{-4}$	2.5

The values of Table 4.20 are applied to Equation 4.3 in order to calculate the photon and neutron fluences for the various situations. These values, depending on the primary beam compositions, are listed in Table 4.21.

Table 4.21: Photon and neutron fluences at the BGO position. The nominal fluence values reflect the fluence situations induced by nominal beam composition. The other numbers represent the fluences in case of the listed beam composition variation.

	Nominal	$p/\pi^+ -3 \%$	$p/\pi^+ -3 \%$	$K^+/p -3 \%$	$K^+/p +3 \%$
200cm 40GeV/c mid					
γ	$31.043 \cdot 10^{-4}$	$31.091 \cdot 10^{-4}$	$31.052 \cdot 10^{-4}$	$31.058 \cdot 10^{-4}$	$31.133 \cdot 10^{-4}$
n	$13.458 \cdot 10^{-4}$	$13.467 \cdot 10^{-4}$	$13.466 \cdot 10^{-4}$	$13.463 \cdot 10^{-4}$	$13.485 \cdot 10^{-4}$
200cm 40GeV/c side					
γ	$5.363 \cdot 10^{-5}$	$5.364 \cdot 10^{-5}$	$5.367 \cdot 10^{-5}$	$5.365 \cdot 10^{-5}$	$5.371 \cdot 10^{-5}$
n	$13.438 \cdot 10^{-5}$	$13.437 \cdot 10^{-5}$	$13.450 \cdot 10^{-5}$	$13.442 \cdot 10^{-5}$	$13.456 \cdot 10^{-5}$
240cm 40GeV/c mid					
γ	$7.297 \cdot 10^{-4}$	$7.313 \cdot 10^{-4}$	$7.297 \cdot 10^{-4}$	$7.301 \cdot 10^{-4}$	$7.322 \cdot 10^{-4}$
n	$3.336 \cdot 10^{-4}$	$3.339 \cdot 10^{-4}$	$3.339 \cdot 10^{-4}$	$3.338 \cdot 10^{-4}$	$3.346 \cdot 10^{-4}$
240cm 40GeV/c side					
γ	$1.474 \cdot 10^{-5}$	$1.474 \cdot 10^{-5}$	$1.477 \cdot 10^{-5}$	$1.475 \cdot 10^{-5}$	$1.478 \cdot 10^{-5}$
n	$3.948 \cdot 10^{-5}$	$3.946 \cdot 10^{-5}$	$3.955 \cdot 10^{-5}$	$3.949 \cdot 10^{-5}$	$3.956 \cdot 10^{-5}$
	Nominal	$p/\pi^+ -2 \%$	$p/\pi^+ -2 \%$	$K^+/p -3 \%$	$K^+/p +3 \%$
240cm 120GeV/c mid					
γ	$44.208 \cdot 10^{-4}$	$44.248 \cdot 10^{-4}$	$44.143 \cdot 10^{-4}$	$44.116 \cdot 10^{-4}$	$44.260 \cdot 10^{-4}$
n	$19.105 \cdot 10^{-4}$	$19.117 \cdot 10^{-4}$	$19.085 \cdot 10^{-4}$	$19.075 \cdot 10^{-4}$	$19.122 \cdot 10^{-4}$
240cm 120GeV/c side					
γ	$8.513 \cdot 10^{-5}$	$8.513 \cdot 10^{-5}$	$8.511 \cdot 10^{-5}$	$8.502 \cdot 10^{-5}$	$8.519 \cdot 10^{-5}$
n	$22.542 \cdot 10^{-5}$	$22.549 \cdot 10^{-5}$	$22.531 \cdot 10^{-5}$	$22.520 \cdot 10^{-5}$	$22.555 \cdot 10^{-5}$
200cm 120GeV/c side					
γ	$1.975 \cdot 10^{-4}$	$1.979 \cdot 10^{-4}$	$1.961 \cdot 10^{-4}$	$1.959 \cdot 10^{-4}$	$1.983 \cdot 10^{-4}$
n	$5.440 \cdot 10^{-4}$	$5.446 \cdot 10^{-4}$	$5.432 \cdot 10^{-4}$	$5.436 \cdot 10^{-4}$	$5.450 \cdot 10^{-4}$

With the values of Table 4.21, the possible beam-composition dependent variations of the fluence results can be determined. These variations, applied together with the single counting rate contributions (Table 4.16) on Equation 4.4, yield the uncertainties of the counting rates.

The rate uncertainties, which are induced by the limited knowledge of the primary beam compositions, are smaller than 0.3 % for all 40 GeV/c situations.

The rate uncertainties, which are induced by the limited knowledge of the primary beam compositions, are smaller than 0.2 % for all 120 GeV/c situations.

4.8.4. Influences of the size of the BGO crystal

The uncertainty of the size of the cylindrical BGO crystal can be assumed with less than 0.1 mm in height and diameter. For figuring out the variation of the rate in the BGO induced by a variation of the dimensions, one has to know the following values:

1. The current entering the nominal BGO crystal.
2. The average particle track-length through the nominal BGO crystal.
3. The current entering the enlarged BGO crystal.
4. The average particle track-length through the enlarged BGO crystal.
5. The number of events induced by the various particle sorts.

A picture and a description of the used BGO can be found in Chapter 3.2. The dimensions of the BGO crystal are 38 mm in height and diameter. In the following procedure, the crystal parameters height and diameter are increased by 0.1 mm. The investigated particles are photons. This result will be extrapolated to neutrons afterwards. The single steps will be realized for the BGO behind 200 cm iron at the side position. The primary particles have a momentum of 40 GeV/c.

1. Calculation of the γ current entering the BGO crystal

The current in the nominal BGO ($A = 68.05 \text{ cm}^2$) can be received from FLUKA simulations concerning this situation. The integrated number of entering photons, having an energy of 350 keV and 9000 keV, can be quoted to:

$$\text{Current} = 8.89 \cdot 10^{-4} \text{ } \gamma / (\text{primary particle})$$

We need for 2. the average number of necessary primary particles to induce one γ at the BGO crystal. This is calculated with the reciprocal current, which yields a value of **1125 primary particles**.

2. Calculation of the average γ track-length through the nominal BGO

For the calculation of the average track-length through the BGO we need the volume of the crystal and the fluence at BGO range. The fluence at BGO range can be obtained from the radial dependent calculation for the 200 cm scenario at 40 GeV/c (see Chapter 4.6). The proper value can be found between 56 and 58 cm off beam axis. The fact that the average track-length can be calculated with

$$\text{track-length} = \text{fluence} \cdot \text{volume} \tag{Equation 4.5}$$

opens the possibility to obtain the average track length of one γ per primary particle. With this value and the number of necessary primary particles to obtain one γ at the BGO, one can calculate the average track length of a photon through the BGO. The necessary values for calculating this average track-length are:

1. The fluence between 56 and 58 cm off axis (fl): **$5.19 \cdot 10^{-5} \text{ } \gamma / \text{primary particle}$**
2. The volume of the BGO crystal (V): **43.10 cm^3**
3. The necessary numbers of primary particles to obtain one photon, which enters the BGO crystal (Nr): **1125 primary particles**

From these values, the average track-length is calculated to be:

$$\text{track-length} = fl \cdot V \cdot Nr = \mathbf{2.5165 \text{ cm}} \quad \text{Equation 4.6}$$

With the values, obtained from the procedure above and the rate induced in the nominal BGO by γ 's only, one can calculate the average detection probability for one γ entering the nominal BGO crystal. The probability is:

$$P = \frac{\gamma_{\text{rate}}}{\text{current}} = \frac{3.84 \cdot 10^{-4}}{8.89 \cdot 10^{-4}} = \mathbf{0.432} \quad \text{Equation 4.7}$$

The probability can also be calculated with:

$$P = 1 - e^{-\lambda \cdot \text{Track-length}} \quad \text{Equation 4.8}$$

With Equation 4.7 and 4.8 the material dependent absorption coefficient (λ) can be extracted.

$$\lambda = \mathbf{0.2248 \text{ cm}^{-1}}$$

3. Calculation of the γ current entering the enlarged BGO crystal

For the calculation of the current entering the enlarged BGO crystal we need the following values:

1. The average current/cm² entering the nominal BGO crystal ($c_{av} = \mathbf{1.3064 \cdot 10^{-5}}$).
2. The surface of the enlarged BGO crystal ($A_{enl} = \mathbf{68.41 \text{ cm}^2}$).

The current in the enlarged BGO crystal (C_{enl}) is therefore:

$$C_{enl} = c_{av} \cdot A_{enl} = \mathbf{8.937 \cdot 10^{-4} \text{ } \gamma / (primary \text{ particle})} \quad \text{Equation 4.9}$$

Also in this case we will need the necessary number of primary particles to generate one γ at the BGO position. This number (Nr_{enl}) is **1119**.

4. Calculation of the average γ track-length through the enlarged BGO

To calculate this value we need also the volume of the enlarged BGO crystal. The volume (V_{enl}), which is defined by an increase of the crystal diameter and height by 0.1 mm, can be calculated to a value of 43.44 cm³. To obtain the average track-length through the enlarged crystal, the same procedure as already used in 2. can be applied also here:

$$\text{Track-length}_{enl} = fl \cdot V_{enl} \cdot Nr_{enl} = \mathbf{2.5228 \text{ cm}} \quad \text{Equation 4.10}$$

With the current in the enlarged crystal and the average track-length of a γ through this crystal, we can calculate the rate, which is induced by the existing radiation field in the enlarged BGO:

$$rate = C_{\text{mod}} \cdot (1 - e^{-\lambda \cdot \text{track-length}_{\text{enl}}}) \quad \text{Equation 4.11}$$

The value for the new rate is: **$3.868 \cdot 10^{-4}$ counts/primary particle**

Therefore, the resulting uncertainty is calculated as: $\sigma = +0.8\%$. The resulting uncertainty in case of an 0.1 mm reduction of the BGO dimensions can be calculated in the same way and results to -0.8% . The same procedure can be performed for neutrons as well. The effect is smaller due to the lower absolute cross section for neutrons. Hence, the absolute variation of rate, induced by a variation of the BGO dimensions is evaluated to be $\pm 0.8\%$.

4.8.5. Influence of variable absorber depth

For the calculation of the effect induced by a variation of the absorber depth, different procedures adapted to the different situations were used. The uncertainty assessments are split in cases concerning different primary beam momenta.

40 GeV/c:

Calculation for the cases at 200 and 240cm side:

The counting rates at the side positions behind 160 cm, 200 cm and 240 cm were calculated with FLUKA and are shown in Table 4.22.

Table 4.22: FLUKA counting rate results per primary beam particle at the side position as a function of the absorber depth.

40 GeV/c	
Absorber depth	Counting rate
cm	counts/prim.particle
160	$18.4 \cdot 10^{-4}$
200	$6.05 \cdot 10^{-4}$
240	$1.9 \cdot 10^{-4}$

With these 3 points the gradient of the rate at 200 and 240 cm can be calculated. To obtain these values at 200 and 240 cm an exponential decay fit was used. The fit through these 3 points yields Equation 4.12.

$$rate = -2.003 \cdot 10^{-5} + 1.86 \cdot 10^{-3} e^{\left(-\frac{(x-160)}{36.67882}\right)} \quad \text{Equation 4.12}$$

x ... Depth of the absorber in cm

The gradient of this curve at the absorber depth of 200 cm is $-1.704 \cdot 10^{-5}$ counts/cm. In case of a depth variation of the 200 cm absorber by 3mm the resulting uncertainty can be assessed to $\pm 0.8 \%$.

The gradient at a iron depth of 240cm can be calculated to $-5.726 \cdot 10^{-6}$ counts/cm. Therefore, the resulting uncertainty induced by a depth variation of 3 mm at 240 cm can be calculated to $\pm 0.9 \%$.

Calculation for the cases at 200 and 240 cm mid:

No data are available for the scenario “160cm 40GeV/c mid”. However, the rate between 200 cm and 240 cm mid position decreases 1.4 times faster than the comparable side position rates. This fact provides us with the possibility to assess the gradients of the mid-rates via a multiplication of the rate gradient at the side positions with this factor.

Hence the values for the uncertainties can be stated to:

200cm: uncertainty (mid) = uncertainty (200 side) $\cdot 1.4 = 0.8 \%$ $\cdot 1.4 = \mathbf{1.1 \%$

240cm: uncertainty (mid) = uncertainty (240 side) $\cdot 1.4 = 0.9 \%$ $\cdot 1.4 = \mathbf{1.3 \%$

120 GeV/c:

Calculation for the cases at 200 and 240 cm side:

The counting rates at the side position behind 160 cm, 200 cm and 240 cm were calculated with FLUKA and are shown in Table 4.23.

Table 4.23: FLUKA simulation results concerning the counting rates at various side positions as a function of the absorber depth.

120 GeV/c	
Absorber depth	Counting rate
cm	Counts/p.p
160cm	$60.8 \cdot 10^{-4}$
200cm	$26.0 \cdot 10^{-4}$
240cm	$7.9 \cdot 10^{-4}$

Also for these situations an exponential decay fit between the 3 points of Table 4.22 was used in order to assess a rate gradient at 200 and 240 cm. The obtained fit result is shown in Equation 4.13.

$$rate = -1.17 \cdot 10^{-3} + 7.25 \cdot 10^{-3} e^{\left(-\frac{(x-160)}{61.18964}\right)} \quad \text{Equation 4.13}$$

x ... Depth of the absorber in cm

The gradient of this curve at the absorber depth of 200 cm is $-6.16 \cdot 10^{-5}$ counts/cm. In case of a depth variation of the 200 cm absorber by 3 mm the resulting uncertainty can be assessed to $\pm 0.7 \%$.

The gradient at an iron depth of 240 cm can be calculated to $-3.21 \cdot 10^{-5}$ counts/cm. Therefore, the resulting uncertainty induced by a depth variation of 3 mm at this depth can be calculated to: $\pm 1.2\%$

Calculation for 240 cm mid:

No calculations for the “200cm 120 GeV/c mid” situation were carried out. Therefore, an assessment of the uncertainty comparable to the situation of the 40 GeV/c is not possible.

But, if we perform a general comparison between the situation “240cm 120GeV/c mid” and the situation “200cm 40GeV/c mid” we find a lot of similarities. A list of these similarities can be found in Table 4.24.

Table 4.24: Comparison between the radiation conditions of the situations “200cm 40 GeV/c mid” and “240cm 120 GeV/c mid”.

	200 cm 40 GeV/c mid	240 cm 120 GeV/c mid
Counting rate/(prim.particle)	$71.8 \cdot 10^{-4}$	$78.6 \cdot 10^{-4}$
Average γ 's per γ multi event	3.23	3.18
Fluence factor: γ/n	2.27	2.32

The simulated rate agrees within 10%. The radial dependent fluence is also very similar. The γ multi event rate at both BGO positions agrees within 2 %. Both shower processes are apparently in a very similar state. Therefore, it is justified to take for the uncertainty of this situation the uncertainty values of the situation “200cm 40GeV/c mid”. This uncertainty yields a value of **1.1 %** in case of a 3 mm variation.

4.8.6. Influence of the absorber density:

For the calculation of the influence of the absorber density variation on the counting rate the results from Chapter 4.8.6 can be modified in the following way. Small variations of density have the same effect as a variation of the depth while keeping the surface density (g/cm^2) the same. Incoming particles see the same amount of particles. The effect that the distance between the beam impact point and the detector increases can be neglected for small variations. Therefore, the rate gradients for the different points, calculated in the previous chapter can be used. The density of the absorber is supposed to be accurate within 0.5%. The calculated uncertainties can be found in Table 4.25.

Table 4.25: Uncertainties induced by an absorber density variation of 0.5 %.

	40 GeV/c				120 GeV/c		
	200cm mid	200cm side	240cm mid	240cm side	200cm side	240cm mid	240cm side
Δ %	3.9	2.8	5.1	3.6	2.4	2.8	3.6

4.8.7. Influence of the distance between BGO and iron absorber

The distance between the iron absorber used and the BGO crystal is known within ± 1 mm. The way to assess the uncertainty induced by this variation is as follows. If one assumes an isotropic source at the end of the absorber, perpendicular to the midpoint of the BGO (worst case concerning uncertainty), the fluence received at the BGO midpoint changes in a quadratic manner with the distance. The nominal distance between the absorber and the BGO is 90 mm. Therefore, the uncertainty induced by a variation of 1 mm is less than 2.2%.

4.8.8. Summary of the systematic uncertainties:

In Table 4.26 all uncertainties are shown. The square root of the quadratic sums of the single values yields the final uncertainties which are listed in Table 4.27.

Table 4.26: Summary of the systematic uncertainties.

	A	B	C	D	E	F	G
200cm 40GeV/c mid	-16.8/-4.6	-11.2/+7.9	± 0.3	± 0.8	± 1.1	± 3.9	± 2.2
200cm 40GeV/c side	± 2.4	-10.4/+8.9	± 0.3	± 0.8	± 0.8	± 2.8	± 2.2
240cm 40GeV/c mid	-14.6/+14.6	-15.8/+4.8	± 0.3	± 0.8	± 1.3	± 5.1	± 2.2
240cm 40GeV/c side	± 2.7	-5.6/+11.5	± 0.3	± 0.8	± 0.9	± 3.6	± 2.2
200cm 120GeV/c side	± 3.5	-8.6/+8.8	± 0.3	± 0.8	± 0.7	± 2.4	± 2.2
240cm 120GeV/c mid	-13.2/+6.7	-1.3/+9.1	± 0.2	± 0.8	± 1.1	± 2.8	± 2.2
240cm 120GeV/c side	± 2.4	-10.3/+13.7	± 0.2	± 0.8	± 1.2	± 3.6	± 2.2

- A... Variable distance between beam and BGO crystal
 B... Variable carbon contents of the iron absorber
 C... Variable composition of the primary hadron beam
 D... Size of the BGO
 E... Uncertainty of the measured depth of the iron absorber
 F... Variation of the absorber density
 G... Variation of distance between BGO and iron absorber

Table 4.27: Final systematic uncertainty of the different simulated cases.

200cm 40GeV/c mid	200cm 40GeV/c side	240cm 40GeV/c mid	240cm 40GeV/c side	200cm 120GeV/c side	240cm 120GeV/c mid	240cm 120GeV/c side
-20.7	-9.9	-22.3	-7.6	-9.9	-13.8	-11.5
+9.2	+11.3	+16.4	+12.6	+10.1	+11.9	+14.6

4.9. Summary of this chapter

In this chapter, all details of the ATLAS equivalent setup were discussed. The set-up consisted of a cast iron block, having a depth of either 2.0 or 2.4 m. This construction is irradiated by a hadron beam, having a momentum of 40 or 120 GeV/c. The measurements behind the iron set-up were performed with a BGO scintillator, located at two different distances to the beam axis. These scenarios were reproduced in the FLUKA simulations. The simulation procedure, which yields measurement comparable results, was discussed extensively. Furthermore, the differences between the two simulated measurement positions, namely the one close to the beam axis (mid position) and the one further away from the beam axis (side position), were explained explicitly.

For all situations, the radial dependence of the fluence were presented. In all cases, the photon fluence was the dominant part of the radiation field close to the beam axis. However, a strong decrease of the photon fluence with increasing distance to the beam axis was found. This result is explained with an increased π^0 production rate, close to the beam axis. The neutron fluence was recognized to be the dominant contribution of the radiation field at positions 60 cm off beam axis.

The scenario defined by the 200 cm iron wall, which was irradiated by 40 GeV/c hadrons, was investigated concerning currents entering the BGO. The contribution of particles with energies below 1 MeV was in all cases higher than 60 %. But in the mid position, also events in the GeV range occurred, albeit rarely.

The events hitting the BGO were classified. In all mid positions many events occur, in which more than one particle hit the BGO together (multi-events). If the BGO is located at side positions, particles hitting the BGO are mostly unaccompanied.

In terms of the origin of photons entering the BGO, it was found that photons close to the beam axis are mainly produced by π^0 decays. At a position 60 cm off beam axis, photons originate mainly from neutron-induced interactions.

The counts, which are induced in the BGO, are produced mostly by photons. However, at side positions the contribution of neutron counts increase to a level of about 30 %.

Finally, systematic uncertainties due to a limited knowledge of several parameters were assessed. The uncertainty induced by these effects is mostly below 20 %.

CHAPTER 5

5. Analysis and discussion of the results

5.1. Introduction

This chapter presents the most important part of the thesis. In these pages, the H6 simulations are compared with the measurements. This comparison is carried out in several ways, namely:

- A comparison concerning the total rate.
- A comparison concerning the energy deposition spectra.
- A comparison concerning the average deposited energy in the detector.
- A comparison between rates, induced only by photons.

The results of these comparisons will be illustrated and discussed in some detail. Furthermore, a discussion concerning the equivalence between the H6 measurements and the ATLAS experiment is presented. As final conclusion we recommend a modification of the uncertainty factor of the ATLAS background simulations.

5.2. Comparison between measured and simulated results

5.2.1. Comparison of the total counting rates

The total rate, induced in the BGO crystal, is mainly influenced by photon and neutron fluences. The previous mentioned Monte Carlo neutron procedure inside FLUKA, which is explained in Chapter 3.4.4 and 4.7.4, should not affect the total counting rate. If the total cross section for the single nuclei are correct, a correct total counting rate of the integrated spectra can be expected. In general, the probability of obtaining a faulty rate result rises with decreasing energy-threshold width. The following counting rate comparisons between the measurements and the simulations are performed within an energy range from 0.35 to 9.0 MeV.

In order to obtain the simulated counting rate results, the three step scenario (which is explained in the beginning of Chapter 4.6) was carried out at all different positions and energies. The result of this rate benchmark is shown in Table 5.1. The simulation uncertainties in this table covers only statistical influences of the simulation. Uncertainties induced by influences of different measured parameter, which were implemented in the simulations, are shown in Table 4.27. More details about these uncertainties can be found in Chapter 4.8. The uncertainties of the measurement results include statistic and systematical influences. The uncertainty of the ratio comparison includes all possible uncertainties. Detailed information about the measurements of this benchmark can be found in [Gsc00].

Table 5.1: Comparison between simulated and measured counting rates (energy range: 350 keV - 9 MeV)

	Simulated rate per beam particle	Measured rate per beam particle	ratio M/S	-Δ ratio	+Δ ratio
40GeV/c					
200cm mid	$(7.18 \pm 0.11) \cdot 10^{-3}$	$(7.62 \pm 0.04) \cdot 10^{-3}$	1.06	-0.22	+0.10
200cm side	$(6.05 \pm 0.28) \cdot 10^{-4}$	$(6.8 \pm 0.2) \cdot 10^{-4}$	1.12	-0.14	+0.14
240cm mid	$(1.58 \pm 0.05) \cdot 10^{-3}$	$(2.30 \pm 0.04) \cdot 10^{-3}$	1.46	-0.33	+0.25
240cm side	$(1.86 \pm 0.15) \cdot 10^{-4}$	$(2.3 \pm 0.1) \cdot 10^{-4}$	1.24	-0.15	+0.19
120GeV/c					
200cm side	$(2.60 \pm 0.14) \cdot 10^{-3}$	$(2.63 \pm 0.04) \cdot 10^{-3}$	1.01	-0.12	+0.12
240cm mid	$(7.86 \pm 0.22) \cdot 10^{-3}$	$(9.35 \pm 0.17) \cdot 10^{-3}$	1.19	-0.17	+0.15
240cm side	$(7.87 \pm 0.87) \cdot 10^{-4}$	$(9.7 \pm 0.6) \cdot 10^{-4}$	1.24	-0.21	+0.24

A weighted average of the ratios between the measurements and the simulations yields a value of: **1.13 ± 0.06**

Although strong neutron contributions can be found at several measurement positions, one can conclude that the integrated simulated rates agree very well with the measurements. The main reasons that the total simulated energy deposition counts, induced by neutrons, agree for the H6 scenarios much better than in case of the Am-Be measurement, can be found in the following points:

- The energy range for the integration of the total counts is bigger (0.35 – 9 MeV versus 0.4 – 6.5 MeV).
- At H6, neutrons produce more high energy counts in the BGO. These energy depositions induce in reality and in the simulation an energy deposition far beyond the 350 keV threshold. Therefore, the distortion induced by this 350 keV threshold becomes less critical.

In Figure 5.1, the spectral comparison between all simulation results and the appropriate measurements is shown. The dotted lines always indicate the measurement results concerning energy deposition in the BGO crystal. In all mid positions, the contribution of neutrons is reduced. Therefore, the shape of the pertinent spectra agrees better than at the side positions. The strong “hills” in the simulated spectra are an artifact of the Monte Carlo procedure inside FLUKA, dealing with neutron interactions and energy depositions. The detailed description concerning this fact can be found in Chapters 3.4.4, 4.7.4 and in Appendix A. The calculated spectra for all side scenarios were produced with the biased method. There are two reasons that the biased procedure can be used for these situations. The first implies that the number of multi events (almost only double events) is always close to a level of 5 %. The second deals with the probability that both particles of a double event react together. Most double events at side positions consist of one photon and one neutron. The average probability that the neutron reacts is less than 10 %. The reaction probability of a photon is about 40 %.

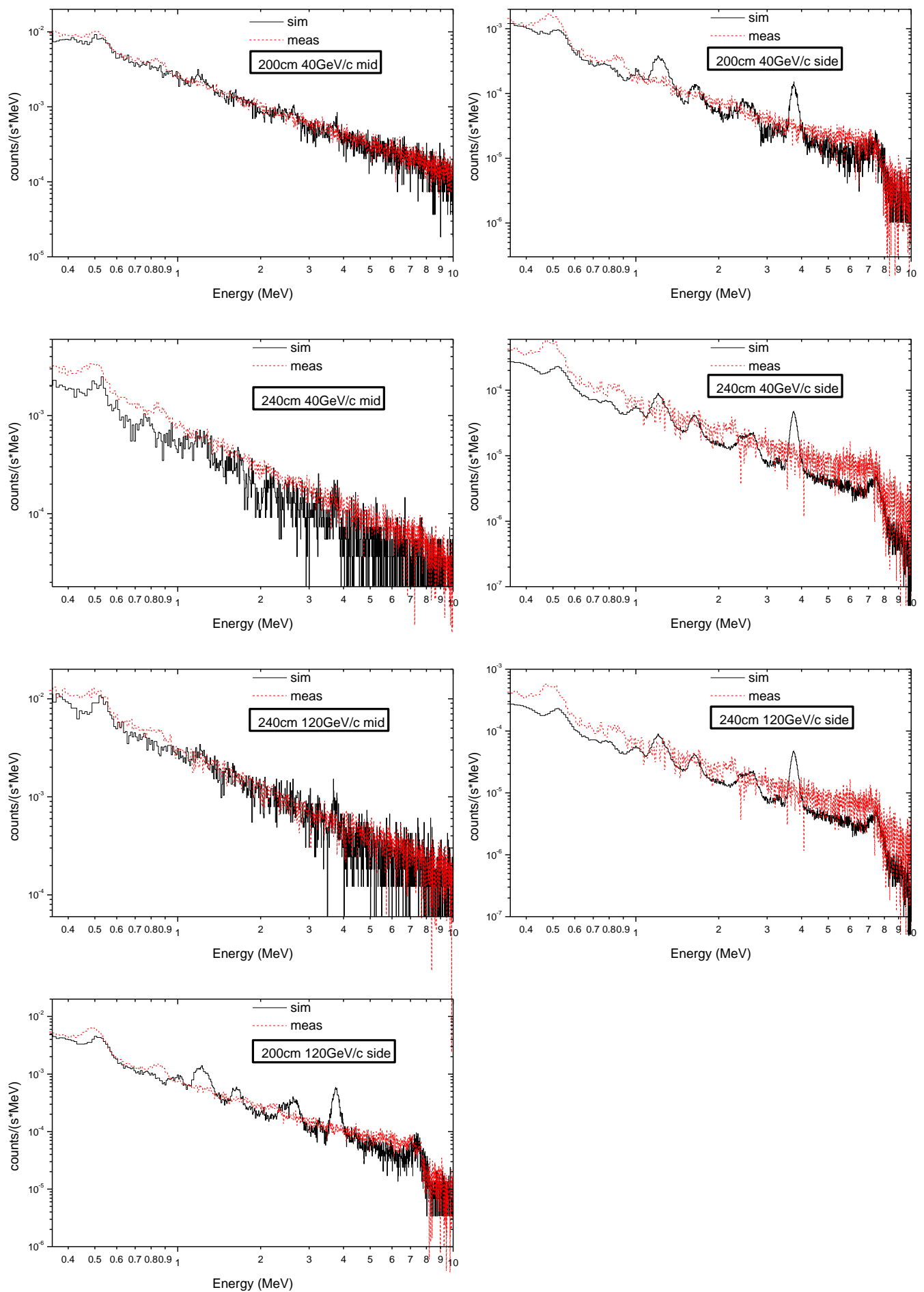


Figure 5.1: Comparison between measured and simulated spectra.

5.2.2. Comparison between the average energy deposition

In order to investigate the simulated average energy deposition induced by an event, all seven situations were compared with the measurements. The procedure which leads to the desired values is described by Equation 5.1.

$$\langle E_{dep} \rangle = \frac{\sum_{i=E_{min}}^{E_{max}} C_i \cdot E_i}{\sum_{i=E_{min}}^{E_{max}} C_i} \quad \text{Equation 5.1}$$

C_i ... Counting rate in energy channel i
 E_i ... Energy of the single channel i
 E_{min} ... Minimum energy of the investigated energy range
 E_{max} ... Maximum energy of the investigated energy range

Each event in the BGO is multiplied with its energy. The sum of all these numbers is divided by the counting rate in order to obtain the average energy deposited in the BGO. In order to assess the uncertainty of this value, only rate uncertainties, having an influence on the shape of the spectra, are regarded. Uncertainties like dead time corrections (measurement) or limited BGO position knowledge are not taken into account. The applied values for ΔC_i are 1 % for the measurements and 10 % for the simulations.

The big advantage in contrast to the spectra comparison can be found in the fact that the neutron induced peaks do not distort the result. The reason is that the peaks in the simulation reflect already an average energy deposit. If we calculate the average value of these peaks, we obtain the correct value for the average energy deposition induced by neutrons. The result for the measured average energy deposition induced by neutrons is the sum over all n- induced interactions in the crystal. Hence, despite the neutron peaks in the simulation, the result of the measurement is comparable with the simulated values. In Table 5.2, the comparison for all the different scenarios is shown.

Table 5.2 : Comparison between the averaged simulated and measured energy depositions in the BGO crystal (energy range: 350 keV - 9 MeV)

	Simulated average energy deposition	Measured average energy deposit	Ratio M/S
	MeV/event	MeV/event	
40GeV/c			
200cm mid	2.057±0.174	2.045 ± 0.018	0.996 ± 0.085
200cm side	1.618±0.041	1.615 ± 0.004	0.997 ± 0.025
240cm mid	1.824±0.073	1.923 ± 0.009	1.055 ± 0.042
240cm side	1.530±0.021	1.666 ± 0.003	1.089 ± 0.015
120GeV/c			
200cm side	1.805±0.091	1.572 ± 0.009	0.871 ± 0.044
240cm mid	2.058±0.183	2.051 ± 0.020	0.997 ± 0.089
240cm side	1.687±0.051	1.649 ± 0.006	0.978 ± 0.030

5.2.3. Comparison of the measured and simulated photon rate

For a comparison between simulated and measured photon rates, one has to find a way to produce a measured rate value, which represents events induced by photons only. In order to obtain such a value, the simulated pure neutron (n-rate) and mixed multi event counts (mme-rate) have to be subtracted from the measurement (total-rate). The remaining fraction can be assumed to be a counting rate, induced only by pure photon events (photon-rate).

$$\text{photon-rate}_{\text{meas}} = \text{total-rate}_{\text{meas}} - (\text{n-rate} + \text{mme-rate})_{\text{sim}} \quad \text{Equation 5.2}$$

n-rate ... Rate induced by pure neutron events

mme-rate ... Rate induced by multi-events, consisting of different kind of particles

The uncertainty induced by this procedure can be assessed as follows: the rate disagreement between the Am-Be measurement and the simulation is less than 30 %. Although the neutron error of the H6 simulation procedure is assumed to be better (explained in Chapter 5.2.1), we state the neutron induced uncertainty for these calculations at a 30 % level.

$$\sigma_n = \text{n-rate}_{\text{sim}} \cdot 0.3 \quad \text{Equation 5.3}$$

For the uncertainty induced by the subtraction of the mixed multi events, one has to take the following circumstances into account:

- 1) The interaction probability in the BGO crystal is at least 4 times higher for photons than for neutrons. Therefore, about each fourth mixed multi event which causes a count in the BGO is induced completely or partly by a neutron.
- 2) At mid positions, about 75 % of the mixed multi-events contain neutrons. At the side positions, this values increases to a level of 90 %.

Therefore, the induced uncertainty of the mixed multi-event counts can be calculated to:

$$\sigma_{\text{multi mid}} = (\text{mme-rate})_{\text{sim}} \cdot 0.3 \cdot 0.25 \cdot 0.75 \quad \text{Equation 5.4}$$

$$\sigma_{\text{multi side}} = (\text{mme-rate})_{\text{sim}} \cdot 0.3 \cdot 0.25 \cdot 0.90 \quad \text{Equation 5.5}$$

The results of the photon rate comparisons, including their uncertainties, are listed in Table 5.3. The weighted average value of the comparison yields: **1.25 ± 0.10** .

The main reason that the disagreement between measurement and simulation is bigger for the pure photon comparison than in the case of the total rate comparison can be found in the subtraction procedure itself. From the measurement and the simulation

the same number is subtracted. The result in both cases are two smaller numbers. But these numbers have still the same rate differences as the original numbers. A relative comparison between these numbers leads, therefore, to a larger disagreement.

Table 5.3: Comparison between simulated and measured photon counting rates (energy range: 400 keV - 9 MeV)

	γ -rate per primary particle $\cdot 10^{-4}$						Ratio between meas./simulation		
	Simulation			Measurement					
	value	$-\Delta$	$+\Delta$	value	$-\Delta$	$+\Delta$	value	$-\Delta$	$+\Delta$
40GeV/c									
200cm mid	35.9	-7.5	+3.3	41.1	-6.7	+3.6	1.15	-0.30	+0.15
200cm side	3.5	-0.4	+0.4	4.1	-0.6	+0.6	1.17	-0.21	+0.23
240cm mid	8.0	-1.8	+1.4	15.8	-1.4	+1.2	1.96	-0.48	+0.36
240cm side	1.0	-0.1	+0.2	1.4	-0.2	+0.2	1.40	-0.26	+0.30
120GeV/c									
200cm side	13.9	-1.6	+1.6	14.33	-2.6	+2.6	1.03	-0.22	+0.22
240cm mid	35.1	-4.9	+4.3	48.3	-6.5	+5.8	1.38	-0.27	+0.24
240cm side	5.0	-0.8	+0.9	6.1	-1.1	+1.2	1.22	-0.30	+0.32

5.3. Comparison between the shielding conditions at H6 and ATLAS:

5.3.1. Prediction of ATLAS background fluences with H6 results:

In order to compare our experimental set-up (240 cm cast iron) with the ATLAS calorimeter situation, we use the calculated H6 fluence results for an assessment concerning fluence conditions in ATLAS. The corresponding point in ATLAS can be found at $\eta \sim 2.7$. The position of interest is defined by the first layer of the muon chamber, which is located behind the forward calorimeter. We will show in the following the similarities of the two shielding conditions.

To perform this procedure, the following information is necessary:

1. A correlation between η and the momentum of the particles hitting the ATLAS calorimeter in the range of interest. This value can be calculated by using information concerning the transverse momentum of the secondary particles in ATLAS. The transverse momentum of secondary particles, produced in p-p collisions at LHC energies, can be quoted as $\langle p_T \rangle = 0.46 \text{ GeV/c}$ [Atc96].
2. The amount of particles entering the surrounding material structure of the p-p collision. Also this information can be found in [Atc96]. The necessary formula to calculate this value is:

$$\frac{dN}{d\eta} = 7.47 \quad \text{Equation 5.6}$$

To correct this factor, concerning additional particles produced via neutron and K^0 production, this number is multiplied by 1.15. A calculation of the secondary particle production rate per second, requires also the knowledge of the number of inelastic p-p collisions per second ($8 \cdot 10^8$).

3. For an ATLAS fluence comparison with H6 results, the photon fluence behind the H6 shielding is required. In order to obtain these values, the simulated total fluences results of simulations at 120, 40, 20, 10 and 5 GeV/c were extrapolated to the desired momenta. The radial shape dependence of the extrapolated results was assumed to be similar to the result of 5 GeV/c. A final fit, concerning the radial dependency, can be found in Figure 5.3. In all these simulations pions were chosen as primary particles.

In H6 calculations the fluences behind the iron wall were counted within a radius of 80 cm around the beam axis. Within a radius of 70 cm around the beam axis, more than 90 % of the emitted fluence can be expected. The fluence emerging outside this radius is neglected. Hence, all possible primary “particle lines” in ATLAS within 70 cm around the line, defined by $\eta = 2.7$, are assumed to contribute to the fluence in the position of the first muon chamber at $\eta = 2.7$. The pertinent η range, which correlates with the 70 cm circle around $\eta = 2.7$, ranges from 2.15 to 4.10. All particles, which

enter this η -range within the stated circle are assumed to contribute (with a specific primary momentum) to the shower processes, producing the final photon fluence result (see Figure 5.2) at $\eta=2.7$. With the known transverse momentum (see point 1), one can calculate the momentum range covered by the primary particles. This range goes from 2.0 to 14.2 GeV/c. The different momentum- and distance-dependent fluence contributions are taken from the H6 simulation results. With these fluences, the expected fluence in ATLAS is calculated.

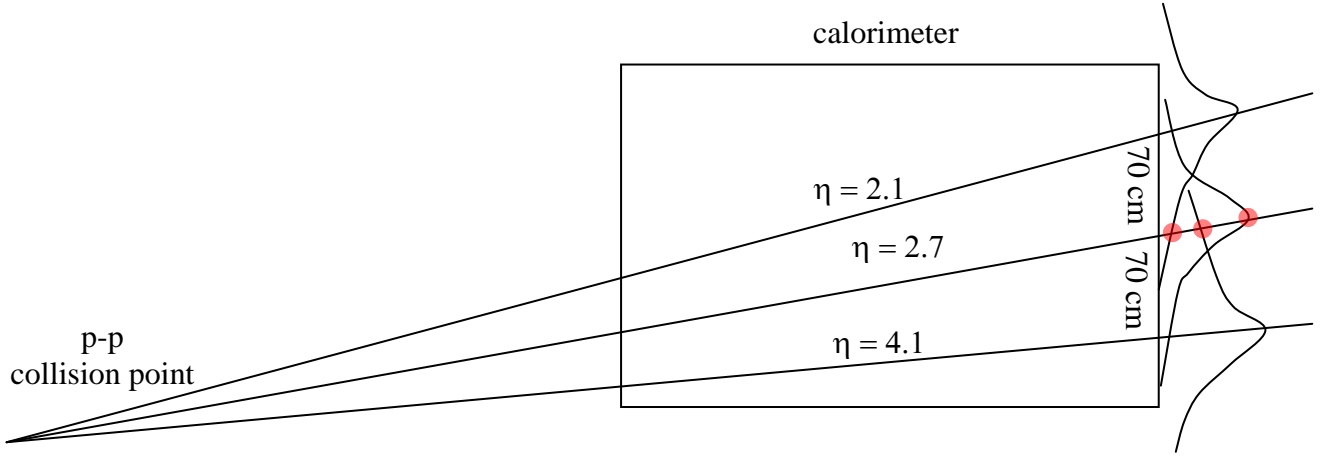


Figure 5.2: Schematic picture comparing H6 to ATLAS. The red spots indicate the fluence contributions coming from the different “primary particle lines”. The fluence contributions are taken from H6 simulations.

The integration (R_{total}) of all (local varying) fluence contributions within a circle of 70 cm around the position, which is defined by the chamber position and $\eta = 2.70$, yields the following result:

$$R_{\text{total}} = \iint_{\text{circle}} \frac{dN}{dA} \cdot 8 \cdot 10^8 \cdot F_{th} \cdot \text{fluence}(\vec{r}) \cdot dA(\vec{r}) = 7.3 \text{ kHz/cm}^2 \quad \text{Equation 5.7}$$

$F_{th} \dots$ (= 1.1) is a factor which concerns different photon thresholds applied in the H6 and the ATLAS calculations.

The first term of the integral, multiplied with dA , yields the number of primary particles per p-p collision, which have a flight direction from the collision point to dA . The fluence term of Equation 5.7 yields the contribution of one primary particle, having the previous mentioned flight direction, to the final fluence result at $\eta = 2.70$.

In order to calculate this integral, a Fortran routine was programmed. To explain the calculation procedure of this program, the following steps have to be mentioned:

- The program divides the circle in parts with an area smaller than 0.1 mm^2 . For each of these sectors the corresponding η including its $\Delta\eta$ is calculated. The number of primary particles (per p-p collision), having a flight direction from the collision point to the actual sector, is computed. In order to obtain this number

Equation 5.6 together with additional information concerning η , $\Delta\eta$ and the area of the sector are used. In this stage of the program, also the momentum of the primary particles entering this small η sector, is calculated.

- Each sector in the circle has a well defined distance to the point, which is defined by the position of the muon chamber ($\eta=2.7$). This distance is calculated. With this value, the fluence contribution, originating from this sector, to the total fluence at $\eta=2.7$ is calculated.
- A summation of all sectors is carried out. In order to obtain the final result (photons per second) a multiplication with several factors (collision rate, threshold factor) is performed.

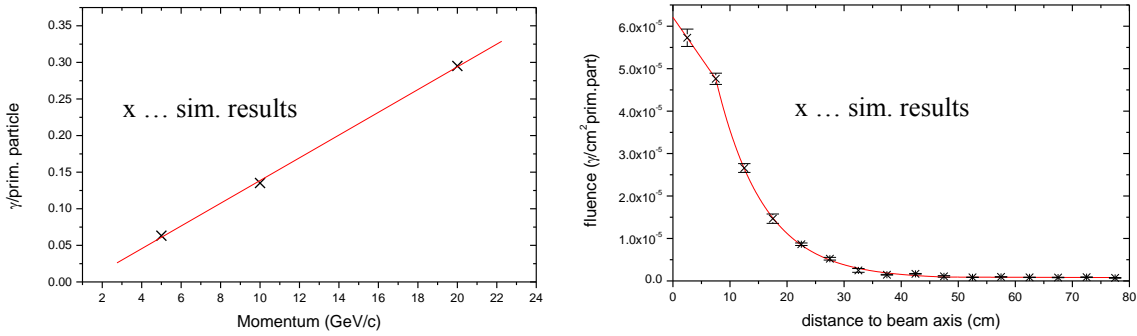


Figure 5.3: Necessary H6 results in order to perform the comparison procedure. Left: total photon fluence (including fit) emerging behind the 2.4 m cast iron block as a function of the primary beam momentum. Right: fluence (including fit) behind the H6 shielding as a function of the distance to the beam axis (primary beam momentum = 5 GeV/c).

The momentum dependent fluence results were extrapolated by using a linear fit. At higher energies than ~ 25 GeV, this linearity is no longer valid.

In order to fit the distance depending spectra, the curve has to be split in 3 ranges:

- 0.0 - 7.5 cm : a linear fit with falling slope was applied to cover the range close to the beam axis.
- 7.5 - 47.5 cm: a second order exponential decay fit was used to fit the medium range.
- 47.5 - 77.5cm: in this range a linear fit with falling slope was used.

5.3.2. ATLAS background fluence results:

From the ATLAS simulations [BAT94a], we know that the muon chamber rate at the examined position is estimated to have the value of 0.21 kHz/cm^2 . In order to obtain the ATLAS background fluence, the following points have to be considered:

- The averaged muon detector efficiency for photons used is $8 \cdot 10^{-3}$.
- The total photon fluence in ATLAS at the comparison position is dominated by a contribution coming directly from the beam line. The fluence, originating from the absorber, is only about between 1/6 and 1/3 of the total fluence estimate.
- 25 % of the residual photon fluence originates from (n,γ) reactions induced by neutrons reflected by the ATLAS hall wall. In H6 this effect is negligible.
- The absorption length of the ATLAS calorimeter construction is 14.5λ . The comparable H6 value is only 14λ . This difference yields a 22 % effect.

The result for the ATLAS fluence at a comparable position has to be calculated via a consideration of the afore mentioned points. Finally, it can be stated to:

$$f_{l_{est.}} = \frac{2.1 \cdot 10^{-3}}{8 \cdot 10^{-3}} \cdot B \cdot 0.75 \cdot 1.22 = 4.0 - 8.0 \frac{\text{kHz}}{\text{cm}^2}$$

$f_{l_{est.}}$... Estimated ATLAS fluence

B ... Factor induced by beam line (1/6 – 1/3)

We conclude: The calculated result for ATLAS using the H6 fluences is within the estimated ATLAS background fluence range. Therefore, the H6 experimental set-up can be seen to be similar to the ATLAS set-up scenario.

5.4. Conclusion for the ATLAS background uncertainty

The uncertainty factor of the FLUKA simulations concerning the ATLAS background scenario were stated to a value of 2.5. However, this benchmark work demonstrated that FLUKA predicts the radiation background on average better than 20 %.

The most relevant results in terms of the ATLAS background are:

1. The total rate comparison between the simulation and the measurement: This value reflects a benchmark concerning the number of particles produced in a shower process within up to 14 hadronic absorption lengths. The average result agrees with measurements to better than 15 % (see Table 5.1).
2. The comparison concerning the average induced energy in the BGO crystal: This value concerns energy attenuation in a quantitative level. The simulation of remnants produced by high-energy particles agree in terms of energies mostly better than 5 % (see Table 5.3).

The uncertainty factor reflects uncertainties about general shower processes in the absorber and (n,γ) reactions at the end of the showering processes. In order to obtain

correct simulation results for all H6 situations, the shower processes has to be simulated correctly. This item is sufficiently demonstrated by this benchmark work. The second concern, the reliability of the simulated (n,γ) reactions, is very well verified in the side position scenarios. At these positions more than 2/3 of the photons, entering the BGO originate from neutron induced interactions (see Table 4.4). Therefore, also the (n,γ) processes were tested successfully by these studies. Based on these benchmarks, a reduction of the uncertainty factor, regarding the reliability of FLUKA under ATLAS conditions, is recommended. An average safety factor, which focuses on the shower process accuracy at ATLAS conditions should be stated to have a value of **1.2**.

5.5. Summary of this chapter

In this chapter an accurate comparison between the ATLAS equivalent measurement and simulation results was performed. This comparison was carried out in four different ways, namely:

- A comparison concerning the total rate.
- A comparison concerning the energy deposition spectra.
- A comparison concerning the average deposited energy in the detector.
- A comparison between rates, induced only by photons.

In the comparison concerning the total rate, the average ratio between the measured and the simulated result is 1.13 ± 0.06 .

The comparison of the spectra yields, except for the explainable neutron peaks, a very good agreement between the measurement and the simulation. Critical lines, like the one induced by the e^+ annihilation, can be found in both measurement and simulation. The sharp edge at an energy of around 8 MeV, found at all side positions, is reproduced correctly in the simulation.

The comparison concerning the average deposited energy in the crystal shows an amazing agreement. At most positions, the level of this agreement is better than 5 %.

The ratio between the simulated photon rate and the measured value shows an agreement at the level of 1.25 ± 0.10 . The fact that the agreement of the total rate is better than the one of the pure photon rate is due to the subtraction procedure used for neutrons.

A procedure which verified the similarity between the ATLAS shielding and the used H6 shielding was performed. It indicates that the two settings are closely comparable.

As a result of this benchmark, a reduction of the uncertainty factor, concerning the ability of FLUKA to calculate shower processes, is recommended. The new level should be set at a value of 1.2.

CHAPTER 6

6. Conclusion

In the framework of this thesis, FLUKA benchmarks concerning two different kinds of simulations were performed. The main body of this thesis dealt with the simulation work concerning a benchmark procedure related to the ATLAS background situation. However, before this task was carried out, a first order benchmark concerning the simulation of the BGO-response to different radioactive sources was realized.

In order to perform this procedure, three different gamma sources (Cs-137, Mn-54 and Co-60) and a neutron source (Am-Be) were used to irradiate the BGO detector.

In terms of the simulation result of the gamma response, the following conclusion can be drawn: The energy deposition in the BGO crystal was simulated in full detail. Physical effects, like pair production, Compton scattering and photo-effect, were reproduced in the simulation with high accuracy. The comparison of the simulated rate with the measured one yields an agreement mostly better than 2 %. Regarding the comparison of the simulated spectra with their measured counterparts one can say that the agreement is good in all energy regions. Effects, like photo peaks, Compton edges or single- and double-escape peaks coincide in all details with the measured values.

The simulation of the energy deposition induced by neutrons, can be summarized as follows: The integrated rate between 400 keV and 6.5 MeV agrees within a level of 30 % with the measurement. This disagreement between the measured and the simulated rate can be explained by the fact that FLUKA uses cross sections, which only provide average neutron energy depositions.

The benchmark procedure, related to the ATLAS background situation, was carried out in four different ways, namely:

- A comparison concerning the total rate.
- A comparison concerning the energy deposition spectra.
- A comparison concerning the average deposited energy in the detector.
- A comparison between rates, induced only by photons.

In the comparison concerning the total rate, the average ratio between the measured and the simulated result is 1.13 ± 0.06 .

The comparison of the spectra yields, except for the explainable neutron peaks, a very good agreement between the measurement and the simulation. Critical lines, like the one induced by the e^+ annihilation, can be found in both spectra. The sharp edge at an energy of around 8 MeV, found at all side positions, is reproduced correctly in the simulation.

The comparison regarding the average deposited energy in the crystal shows a good agreement. At most positions, the level of this agreement is better than 5 %.

The ratio between the simulated photon rates and the measured values shows an agreement at the level of 1.25 ± 0.10 . The fact that the agreement of the total rate is better than the one of the pure photon rate can be explained by the method for neutron subtraction.

A procedure which verified the similarity between the ATLAS shielding and the used H6 shielding was successfully performed.

As a result of this benchmark, a reduction of the uncertainty factor, concerning the ability of FLUKA to calculate shower processes, is recommended. The new level should be set at a value of **1.2**.

Appendix A

BGO neutron cross section data used in FLUKA

The neutrons simulated in FLUKA, having energies between 10^{-11} and 19.6 MeV, are split in 72 energy dependent groups. Below this 19.6 MeV threshold the neutrons do no longer have a certain energy but they belong to a specified energy group. The limits of the single groups are listed below.

Low energy neutron group limits

Group no.	Upper energy	Group no.	Upper energy	Group no.	Upper energy
	GeV		GeV		GeV
1	1.9600E-02	25	1.6530E-03	49	7.1018E-06
2	1.7500E-02	26	1.4957E-03	50	4.8809E-06
3	1.4918E-02	27	1.3534E-03	51	3.3546E-06
4	1.3499E-02	28	1.2246E-03	52	2.3054E-06
5	1.2214E-02	29	1.1080E-03	53	1.5846E-06
6	1.1052E-02	30	1.0026E-03	54	1.0446E-06
7	1.0000E-02	31	9.0718E-04	55	6.8871E-07
8	9.0484E-03	32	8.2085E-04	56	4.5400E-07
9	8.1873E-03	33	7.4274E-04	57	2.7537E-07
10	7.4082E-03	34	6.0810E-04	58	1.6702E-07
11	6.7032E-03	35	4.9787E-04	59	1.0130E-07
12	6.0653E-03	36	4.0762E-04	60	6.1442E-08
13	5.4881E-03	37	3.3373E-04	61	3.7267E-08
14	4.9659E-03	38	2.7324E-04	62	2.2603E-08
15	4.4933E-03	39	2.2371E-04	63	1.5535E-08
16	4.0657E-03	40	1.8316E-04	64	1.0677E-08
17	3.6788E-03	41	1.4996E-04	65	7.3375E-09
18	3.3287E-03	42	1.2277E-04	66	5.0435E-09
19	3.0119E-03	43	8.6517E-05	67	3.4662E-09
20	2.7253E-03	44	5.2475E-05	68	2.3824E-09
21	2.4660E-03	45	3.1828E-05	69	1.6374E-09
22	2.2313E-03	46	2.1852E-05	70	1.1254E-09
23	2.0190E-03	47	1.5034E-05	71	6.8257E-10
24	1.8268E-03	48	1.0332E-05	72	4.1400E-10
			Lower energy limit:1.0000E-14 GeV		

At each scattering process the neutron has also a well-defined probability to produce secondary neutrons and photons. If a photon is produced, the energy of this gamma is selected within a given photon energy group structure. The neutron-induced photons have in general energies between 0 and 20 MeV. Also this energy range is divided into 22 energy dependent groups, which are listed below. The actual energy group chosen for the produced gamma is selected via given probability distributions, which

are assigned to the scattering nuclei and to the energy groups of the scattered neutron. Once this group is selected, the photon energy is chosen randomly within the actual group limits. Finally, the photon is passed through to the EM part inside FLUKA.

Energy limits of neutron induced photons

Group no.	Upper energy GeV	Group no.	Upper energy GeV
1	2.0000E-02	12	4.5000E-03
2	1.4000E-02	13	4.0000E-03
3	1.2000E-02	14	3.5000E-03
4	1.0000E-02	15	3.0000E-03
5	8.0000E-03	16	2.5000E-03
6	7.5000E-03	17	2.0000E-03
7	7.0000E-03	18	1.5000E-03
8	6.5000E-03	19	1.0000E-03
9	6.0000E-03	20	4.0000E-04
10	5.5000E-03	21	2.0000E-04
11	5.0000E-03	22	1.0000E-04
Lower limit: 1.0000E-05 GeV			

The lists below show the properties of Oxygen, Germanium and Bismuth used in FLUKA. These values are energy group dependent and can be interpreted as follows:

- SIGT:** Total cross section of the material (σ_{total}).
- SIGST:** Cross section for non absorption of the neutron (σ_{nonabs}). Also new produced neutrons are taken into account. In case of a production of more than one neutron this value can exceed the total cross section of this material within the stated energy group.
- PNUP:** Up-scattering probability. No up- scattering processes are taken into account. This value is therefore for all materials and energies 0.0.
- PNABS:** ($=\sigma_{\text{nonabs}}/\sigma_{\text{total}}$) Probability of non absorption.
- GAMGEN:** Average number of gammas produced.
- EDEP:** Average energy depositions at each scattering process induced by the neutron within the actual group. In case the neutron is not down-scattered or absorbed the energy deposition is counted more often than one time.
- PNEL:** Probability of non-elastic scattering.
- PXN:** Probability of all non-elastic reactions, producing neutrons.
- PNGAM:** Probability of gamma production.

FLUKA cross section data used for Oxygen

GROUP	SIGT	SIGST	PNUP	PNABS	GAMGEN	EDEP	PNEL	PXN	PNGAM
	barn	barn				GeV/col			
1	1.63E+00	1.55E+00	0	0.946	0.1812	2.37E-03	0.3539	0.2999	0
2	1.73E+00	1.55E+00	0	0.8957	0.3451	1.73E-03	0.3733	0.269	0
3	1.63E+00	1.42E+00	0	0.8702	0.3905	1.77E-03	0.3974	0.2676	0
4	1.59E+00	1.36E+00	0	0.8515	0.4027	1.79E-03	0.4114	0.2628	0
5	1.66E+00	1.39E+00	0	0.8382	0.3821	1.72E-03	0.3792	0.2174	0
6	1.35E+00	1.11E+00	0	0.8285	0.4566	1.72E-03	0.4206	0.2491	0
7	1.22E+00	9.84E-01	0	0.8074	0.4288	1.61E-03	0.4352	0.2425	0
8	1.25E+00	1.07E+00	0	0.8539	0.4583	1.33E-03	0.4729	0.3268	0
9	1.19E+00	1.06E+00	0	0.8903	0.3359	1.19E-03	0.3639	0.2542	0
10	1.15E+00	9.72E-01	0	0.8478	0.1604	1.34E-03	0.2687	0.1165	0
11	9.79E-01	8.44E-01	0	0.8624	0.0081	1.08E-03	0.1413	0.0036	0
12	1.37E+00	1.34E+00	0	0.9762	0	5.53E-04	0.0238	0	0
13	1.33E+00	1.24E+00	0	0.9284	0	6.50E-04	0.0716	0	0
14	1.31E+00	1.22E+00	0	0.9359	0	5.22E-04	0.0641	0	0
15	1.84E+00	1.73E+00	0	0.9389	0	4.36E-04	0.0611	0	0
16	2.60E+00	2.57E+00	0	0.9887	0	3.09E-04	0.0113	0	0
17	3.09E+00	3.09E+00	0	0.9992	0	2.89E-04	0.0007	0	0
18	2.15E+00	2.15E+00	0	0.9998	0	2.94E-04	0.0002	0	0
19	1.12E+00	1.12E+00	0	1	0	2.80E-04	0	0	0
20	1.07E+00	1.07E+00	0	1	0	2.66E-04	0	0	0
21	6.19E-01	6.19E-01	0	1	0	2.49E-04	0	0	0
22	1.39E+00	1.39E+00	0	1	0	2.24E-04	0	0	0
23	2.17E+00	2.17E+00	0	1	0	1.84E-04	0	0	0
24	1.76E+00	1.76E+00	0	1	0	1.92E-04	0	0	0
25	2.12E+00	2.12E+00	0	1	0	1.69E-04	0	0	0
26	2.37E+00	2.37E+00	0	1	0	1.29E-04	0	0	0
27	4.09E+00	4.09E+00	0	1	0	1.12E-04	0	0	0
28	2.95E+00	2.95E+00	0	1	0	1.33E-04	0	0	0
29	5.42E+00	5.42E+00	0	1	0	1.16E-04	0	0	0
30	5.59E+00	5.59E+00	0	1	0	1.07E-04	0	0	0
31	2.95E+00	2.95E+00	0	1	0	9.31E-05	0	0	0
32	2.72E+00	2.72E+00	0	1	0	8.06E-05	0	0	0
33	2.86E+00	2.86E+00	0	1	0	6.41E-05	0	0	0
34	3.54E+00	3.54E+00	0	1	0	4.26E-05	0	0	0
35	1.03E+01	1.03E+01	0	1	0	3.59E-05	0	0	0
36	4.83E+00	4.83E+00	0	1	0	5.02E-05	0	0	0
37	3.55E+00	3.55E+00	0	1	0	3.99E-05	0	0	0
38	3.47E+00	3.47E+00	0	1	0	3.11E-05	0	0	0
39	3.51E+00	3.51E+00	0	1	0	2.47E-05	0	0	0
40	3.57E+00	3.57E+00	0	1	0	1.99E-05	0	0	0
41	3.61E+00	3.61E+00	0	1	0	1.60E-05	0	0	0
42	3.67E+00	3.67E+00	0	1	0	1.20E-05	0	0	0

43	3.74E+00	3.74E+00	0	1	0	7.76E-06	0	0	0
44	3.80E+00	3.80E+00	0	1	0	4.67E-06	0	0	0
45	3.83E+00	3.83E+00	0	1	0	2.99E-06	0	0	0
46	3.85E+00	3.85E+00	0	1	0	2.05E-06	0	0	0
47	3.86E+00	3.86E+00	0	1	0	1.41E-06	0	0	0
48	3.87E+00	3.87E+00	0	1	0	9.64E-07	0	0	0
49	3.88E+00	3.88E+00	0	1	0	6.62E-07	0	0	0
50	3.88E+00	3.88E+00	0	1	0	4.55E-07	0	0	0
51	3.88E+00	3.88E+00	0	1	0	3.13E-07	0	0	0
52	3.88E+00	3.88E+00	0	1	0	2.15E-07	0	0	0
53	3.89E+00	3.89E+00	0	1	0	1.45E-07	0	0	0
54	3.89E+00	3.89E+00	0	1	0	9.54E-08	0	0	0
55	3.89E+00	3.89E+00	0	1	0	6.29E-08	0	0	0
56	3.89E+00	3.89E+00	0	1	0	3.99E-08	0	0	0
57	3.89E+00	3.89E+00	0	1	0	2.42E-08	0	0	0
58	3.89E+00	3.89E+00	0	1	0	1.47E-08	0	0	0
59	3.89E+00	3.89E+00	0	1	0	8.90E-09	0	0	0
60	3.89E+00	3.89E+00	0	1	0	5.40E-09	0	0	0
61	3.89E+00	3.89E+00	0	1	0	3.27E-09	0	0	0
62	3.89E+00	3.89E+00	0	1	0	2.10E-09	0	0	0
63	3.89E+00	3.89E+00	0	1	0	1.45E-09	0	0	0
64	3.89E+00	3.89E+00	0	1	0	9.95E-10	0	0	0
65	3.89E+00	3.89E+00	0	1	0	6.84E-10	0	0	0
66	3.89E+00	3.89E+00	0	1	0	4.70E-10	0	0	0
67	3.89E+00	3.89E+00	0	1	0	3.24E-10	0	0	0
68	3.89E+00	3.89E+00	0	1	0	2.23E-10	0	0	0
69	3.89E+00	3.89E+00	0	1	0	1.54E-10	0	0	0
70	3.89E+00	3.89E+00	0	1	0	1.01E-10	0	0	0
71	3.90E+00	3.89E+00	0	1	0	6.25E-11	0	0	0
72	4.00E+00	4.00E+00	0	1	0.0001	1.78E-11	0	0	0

FLUKA cross section data used for Germanium

GROUP	SIGT	SIGST	PNUP	PNABS	GAMGEN	EDEP	PNEL	PXN	PNGAM
	barn	barn				GeV/col			
1	3.20E+00	3.20E+00	0	0.9994	0	5.84E-03	0.3259	0.3253	0.0006
2	3.59E+00	3.59E+00	0	0.9994	0	4.68E-03	0.3278	0.3274	0.0004
3	3.66E+00	3.66E+00	0	0.9997	0	4.39E-03	0.3318	0.3314	0.0004
4	3.71E+00	3.71E+00	0	0.9996	0	4.15E-03	0.3349	0.3346	0.0004
5	3.82E+00	3.82E+00	0	0.9997	0	3.62E-03	0.3427	0.3424	0.0003
6	3.87E+00	3.87E+00	0	0.9997	0	3.28E-03	0.3497	0.3494	0.0003
7	3.91E+00	3.91E+00	0	0.9997	0	2.96E-03	0.3569	0.3566	0.0003
8	3.93E+00	3.93E+00	0	0.9997	0	2.68E-03	0.3638	0.3634	0.0003
9	3.95E+00	3.95E+00	0	0.9996	0	2.41E-03	0.37	0.3696	0.0004
10	3.96E+00	3.96E+00	0	0.9995	0	2.16E-03	0.3763	0.3758	0.0005
11	3.92E+00	3.91E+00	0	0.9993	0	1.89E-03	0.3869	0.3862	0.0007
12	3.86E+00	3.86E+00	0	0.9988	0	1.66E-03	0.398	0.3968	0.0012
13	3.81E+00	3.81E+00	0	0.9981	0	1.49E-03	0.409	0.407	0.0019
14	3.73E+00	3.72E+00	0	0.9974	0	1.26E-03	0.4076	0.4051	0.0026
15	3.62E+00	3.61E+00	0	0.997	0	1.03E-03	0.398	0.395	0.003
16	3.52E+00	3.51E+00	0	0.9966	0	8.58E-04	0.3889	0.3855	0.0034
17	3.43E+00	3.41E+00	0	0.9961	0	7.22E-04	0.3806	0.3767	0.0039
18	3.34E+00	3.33E+00	0	0.9955	0	6.17E-04	0.3729	0.3684	0.0045
19	3.28E+00	3.26E+00	0	0.9951	0	5.38E-04	0.358	0.3531	0.0049
20	3.23E+00	3.22E+00	0	0.995	0	4.75E-04	0.3355	0.3304	0.005
21	3.20E+00	3.18E+00	0	0.9948	0	4.19E-04	0.3141	0.3089	0.0052
22	3.17E+00	3.15E+00	0	0.9947	0	3.76E-04	0.2978	0.2924	0.0053
23	3.17E+00	3.15E+00	0	0.9946	0	3.39E-04	0.28	0.2746	0.0054
24	3.23E+00	3.21E+00	0	0.9946	0	2.92E-04	0.2507	0.2454	0.0054
25	3.30E+00	3.29E+00	0	0.9947	0	2.51E-04	0.2228	0.2175	0.0053
26	3.42E+00	3.40E+00	0	0.9949	0	2.03E-04	0.1834	0.1783	0.0051
27	3.55E+00	3.53E+00	0	0.995	0	1.72E-04	0.1565	0.1515	0.005
28	3.69E+00	3.67E+00	0	0.9952	0	1.50E-04	0.137	0.1321	0.0048
29	3.83E+00	3.82E+00	0	0.9953	0	1.38E-04	0.126	0.1214	0.0047
30	3.98E+00	3.96E+00	0	0.9953	0	1.22E-04	0.1072	0.1025	0.0047
31	4.14E+00	4.12E+00	0	0.9951	0	1.03E-04	0.0812	0.0763	0.0049
32	4.32E+00	4.29E+00	0	0.9949	0	9.14E-05	0.0644	0.0593	0.0051
33	4.57E+00	4.55E+00	0	0.9946	0	7.47E-05	0.0394	0.034	0.0053
34	4.90E+00	4.87E+00	0	0.9947	0	5.79E-05	0.0172	0.0119	0.0053
35	5.23E+00	5.20E+00	0	0.9948	0	5.41E-05	0.0155	0.0103	0.0052
36	5.58E+00	5.55E+00	0	0.9948	0	5.12E-05	0.0145	0.0092	0.0052
37	5.88E+00	5.85E+00	0	0.9948	0	4.89E-05	0.0136	0.0084	0.0052
38	6.18E+00	6.15E+00	0	0.9948	0	4.70E-05	0.0129	0.0077	0.0052
39	6.49E+00	6.46E+00	0	0.9949	0	4.56E-05	0.0123	0.0072	0.0051
40	6.77E+00	6.74E+00	0	0.9947	0	4.56E-05	0.0118	0.0065	0.0053
41	7.06E+00	7.02E+00	0	0.9946	0	4.60E-05	0.0114	0.0059	0.0054
42	7.47E+00	7.43E+00	0	0.9943	0	4.71E-05	0.0106	0.0049	0.0057

43	8.12E+00	8.07E+00	0	0.9937	0	5.12E-05	0.0072	0.001	0.0063
44	8.97E+00	8.91E+00	0	0.9927	0	5.86E-05	0.0075	0.0002	0.0073
45	9.83E+00	9.75E+00	0	0.9916	0	6.72E-05	0.0085	0.0001	0.0084
46	1.08E+01	1.07E+01	0	0.9907	0	7.48E-05	0.0093	0	0.0093
47	1.10E+01	1.09E+01	0	0.9888	0	8.98E-05	0.0112	0	0.0112
48	1.19E+01	1.18E+01	0	0.9873	0	1.03E-04	0.0127	0	0.0127
49	3.07E+01	3.05E+01	0	0.9937	0	5.08E-05	0.0062	0	0.0062
50	6.54E+00	6.35E+00	0	0.9705	0	2.53E-04	0.0295	0	0.0295
51	9.86E+00	9.38E+00	0	0.951	0	3.74E-04	0.049	0	0.049
52	3.95E+00	3.73E+00	0	0.9447	0	5.37E-04	0.0553	0	0.0553
53	4.46E+00	4.20E+00	0	0.9414	0	5.96E-04	0.0586	0	0.0586
54	4.99E+00	4.60E+00	0	0.9226	0	7.77E-04	0.0774	0	0.0774
55	9.65E+00	8.58E+00	0	0.8897	0	1.00E-03	0.1103	0	0.1103
56	1.14E+01	9.56E+00	0	0.8401	0	1.63E-03	0.1599	0	0.1599
57	8.57E+00	6.33E+00	0	0.7387	0	2.66E-03	0.2612	0	0.2612
58	4.05E+01	3.58E+01	0	0.8831	0	1.19E-03	0.1168	0	0.1168
59	1.52E+01	1.33E+01	0	0.8758	0	1.27E-03	0.1242	0	0.1242
60	2.43E+00	2.35E+00	0	0.9677	0	3.11E-04	0.0322	0	0.0322
61	2.44E+00	2.36E+00	0	0.9695	0	2.88E-04	0.0305	0	0.0305
62	2.46E+00	2.38E+00	0	0.9661	0	3.18E-04	0.034	0	0.034
63	2.48E+00	2.38E+00	0	0.9612	0	3.62E-04	0.0388	0	0.0388
64	2.50E+00	2.39E+00	0	0.9549	0	4.20E-04	0.0451	0	0.0451
65	2.53E+00	2.39E+00	0	0.9469	0	4.93E-04	0.053	0	0.053
66	2.55E+00	2.39E+00	0	0.9374	0	5.81E-04	0.0626	0	0.0626
67	2.59E+00	2.40E+00	0	0.9262	0	6.85E-04	0.0738	0	0.0738
68	2.63E+00	2.40E+00	0	0.9126	0	8.11E-04	0.0874	0	0.0874
69	2.67E+00	2.40E+00	0	0.8967	0	9.58E-04	0.1033	0	0.1033
70	2.74E+00	2.40E+00	0	0.8749	0	1.16E-03	0.1251	0	0.1251
71	2.84E+00	2.40E+00	0	0.8452	0	1.44E-03	0.1548	0	0.1548
72	4.03E+00	2.41E+00	0	0.5982	0	3.72E-03	0.4018	0	0.4018

FLUKA cross section data used for Bismuth

GROUP	SIGT	SIGST	PNUP	PNABS	GAMGEN	EDEP	PNEL	PXN	PNGAM
	barn	barn				GeV/col			
1	5.82E+00	8.96E+00	0	1.5388	1.223	3.20E-04	0.4367	0.4344	0.0001
2	5.47E+00	7.82E+00	0	1.431	1.4026	3.60E-04	0.4766	0.4758	0.0001
3	5.36E+00	7.68E+00	0	1.433	1.3216	4.18E-04	0.488	0.4874	0.0002
4	5.26E+00	7.57E+00	0	1.439	1.2609	4.04E-04	0.4987	0.4981	0.0003
5	5.11E+00	7.27E+00	0	1.4229	1.0236	3.94E-04	0.5178	0.5172	0.0004
6	5.13E+00	6.97E+00	0	1.3575	1.0115	3.88E-04	0.5227	0.5223	0.0004
7	5.24E+00	6.41E+00	0	1.225	1.1314	3.56E-04	0.522	0.5217	0.0003
8	5.40E+00	5.86E+00	0	1.0839	1.327	2.67E-04	0.5068	0.5065	0.0002
9	5.65E+00	5.70E+00	0	1.0093	1.3182	2.58E-04	0.4748	0.4746	0.0002
10	5.98E+00	5.98E+00	0	0.9999	1.1508	2.19E-04	0.4379	0.4377	0.0001
11	6.38E+00	6.38E+00	0	0.9999	1.0056	1.39E-04	0.4073	0.4072	0.0001
12	6.84E+00	6.84E+00	0	0.9999	0.8815	8.68E-05	0.3809	0.3807	0.0002
13	7.23E+00	7.23E+00	0	0.9998	0.7859	2.55E-05	0.3592	0.359	0.0002
14	7.60E+00	7.60E+00	0	0.9998	0.6633	1.20E-05	0.3322	0.332	0.0003
15	7.74E+00	7.73E+00	0	0.9997	0.547	1.99E-05	0.3066	0.3063	0.0003
16	7.91E+00	7.91E+00	0	0.9996	0.4373	2.24E-05	0.2734	0.2731	0.0004
17	7.87E+00	7.86E+00	0	0.9996	0.3421	3.30E-05	0.2427	0.2423	0.0004
18	7.95E+00	7.95E+00	0	0.9995	0.2508	2.66E-05	0.2012	0.2007	0.0005
19	7.84E+00	7.84E+00	0	0.9994	0.1781	3.02E-05	0.1641	0.1635	0.0006
20	7.41E+00	7.40E+00	0	0.9994	0.1328	2.31E-05	0.1341	0.1334	0.0006
21	7.02E+00	7.02E+00	0	0.9994	0.1182	1.76E-05	0.1192	0.1186	0.0006
22	6.65E+00	6.65E+00	0	0.9994	0.1088	1.47E-05	0.1072	0.1066	0.0006
23	6.12E+00	6.12E+00	0	0.9993	0.0967	1.56E-05	0.0962	0.0956	0.0007
24	5.62E+00	5.61E+00	0	0.9993	0.0754	2.25E-05	0.0814	0.0807	0.0007
25	5.39E+00	5.39E+00	0	0.9993	0.0554	1.77E-05	0.06	0.0593	0.0007
26	5.19E+00	5.19E+00	0	0.9993	0.0469	3.22E-06	0.037	0.0363	0.0007
27	5.02E+00	5.02E+00	0	0.9994	0.0389	5.61E-06	0.0328	0.0321	0.0006
28	5.04E+00	5.03E+00	0	0.9995	0.0301	8.63E-06	0.0284	0.0279	0.0005
29	4.99E+00	4.99E+00	0	0.9995	0.0226	6.44E-06	0.0194	0.0189	0.0005
30	5.03E+00	5.03E+00	0	0.9995	0.0109	1.70E-05	0.0115	0.011	0.0005
31	5.03E+00	5.02E+00	0	0.9995	0.002	6.93E-06	0.0007	0.0002	0.0005
32	5.18E+00	5.18E+00	0	0.9995	0.0018	6.20E-06	0.0005	0	0.0005
33	5.66E+00	5.66E+00	0	0.9995	0.0016	5.41E-06	0.0005	0	0.0005
34	6.14E+00	6.13E+00	0	0.9996	0.0015	4.50E-06	0.0004	0	0.0004
35	6.78E+00	6.78E+00	0	0.9996	0.0014	3.73E-06	0.0004	0	0.0004
36	7.40E+00	7.39E+00	0	0.9996	0.0014	3.10E-06	0.0004	0	0.0004
37	7.17E+00	7.17E+00	0	0.9996	0.0015	2.58E-06	0.0004	0	0.0004
38	9.71E+00	9.70E+00	0	0.9997	0.0012	2.14E-06	0.0003	0	0.0003
39	1.05E+01	1.05E+01	0	0.9996	0.0014	1.77E-06	0.0004	0	0.0004
40	9.96E+00	9.96E+00	0	0.9995	0.0018	1.46E-06	0.0005	0	0.0005
41	9.94E+00	9.93E+00	0	0.9996	0.0013	1.21E-06	0.0004	0	0.0004
42	1.06E+01	1.06E+01	0	0.9998	0.001	9.43E-07	0.0003	0	0.0003

43	1.08E+01	1.08E+01	0	0.9991	0.0031	6.28E-07	0.0008	0	0.0008
44	1.19E+01	1.19E+01	0	0.9987	0.0048	3.83E-07	0.0013	0	0.0013
45	1.11E+01	1.10E+01	0	0.9993	0.0026	2.49E-07	0.0007	0	0.0007
46	1.48E+01	1.48E+01	0	0.9997	0.0012	1.69E-07	0.0003	0	0.0003
47	1.76E+01	1.76E+01	0	0.9997	0.001	1.20E-07	0.0003	0	0.0003
48	9.21E+00	9.20E+00	0	0.9993	0.0026	8.16E-08	0.0007	0	0.0007
49	1.16E+01	1.16E+01	0	0.9985	0.0055	5.56E-08	0.0015	0	0.0015
50	1.05E+01	1.05E+01	0	0.9996	0.002	3.87E-08	0.0005	0	0.0005
51	2.62E+01	2.61E+01	0	0.9986	0.0053	2.43E-08	0.0014	0	0.0014
52	1.06E+01	1.06E+01	0	0.9989	0.0044	1.90E-08	0.0012	0	0.0012
53	1.05E+01	1.05E+01	0	1	0.0002	1.23E-08	0.0001	0	0.0001
54	4.92E+01	4.88E+01	0	0.9924	0.0286	7.98E-09	0.0076	0	0.0076
55	7.63E+00	7.63E+00	0	0.9996	0.0013	5.34E-09	0.0004	0	0.0004
56	8.72E+00	8.72E+00	0	0.9999	0.0004	3.41E-09	0.0001	0	0.0001
57	9.03E+00	9.03E+00	0	0.9999	0.0003	2.07E-09	0.0001	0	0.0001
58	9.16E+00	9.15E+00	0	0.9999	0.0003	1.26E-09	0.0001	0	0.0001
59	9.22E+00	9.22E+00	0	0.9999	0.0003	7.64E-10	0.0001	0	0.0001
60	9.26E+00	9.26E+00	0	0.9999	0.0004	4.64E-10	0.0001	0	0.0001
61	9.28E+00	9.28E+00	0	0.9999	0.0005	2.83E-10	0.0001	0	0.0001
62	9.29E+00	9.29E+00	0	0.9999	0.0006	1.84E-10	0.0002	0	0.0002
63	9.30E+00	9.29E+00	0	0.9998	0.0007	1.28E-10	0.0002	0	0.0002
64	9.30E+00	9.30E+00	0	0.9998	0.0008	8.97E-11	0.0002	0	0.0002
65	9.30E+00	9.30E+00	0	0.9997	0.001	6.42E-11	0.0003	0	0.0003
66	9.31E+00	9.30E+00	0	0.9997	0.0012	4.69E-11	0.0003	0	0.0003
67	9.31E+00	9.30E+00	0	0.9996	0.0014	3.58E-11	0.0004	0	0.0004
68	9.31E+00	9.31E+00	0	0.9995	0.0017	2.88E-11	0.0005	0	0.0005
69	9.31E+00	9.31E+00	0	0.9994	0.0021	2.46E-11	0.0005	0	0.0005
70	9.31E+00	9.31E+00	0	0.9993	0.0026	2.30E-11	0.0007	0	0.0007
71	9.32E+00	9.31E+00	0	0.9991	0.0033	2.40E-11	0.0009	0	0.0009
72	9.36E+00	9.33E+00	0	0.9968	0.0121	7.16E-11	0.0032	0	0.0032

Appendix B

Revision history

In this sub chapter the revisions performed in order to improve the code are listed. This list is a quotation, taken from the source routine “mainmvax.f” of FLUKA.

- May 1981: Development version used only by the authors.
- Aug. 1981: Version tested internally in CERN RP-group.
- Aug. 1982: Version put on limited release together with the preliminary Fluka82 manual.
- June 1983: First release of the code and the manual.
- Dec.1983: Known bugs are corrected, Fermi-momentum for nucleons in nuclei are added, “eventq” (= Dual Parton Model +Quasi-two particle resonance-decay model) recommended and used as default option, extending the energy range.
- July 1984: Elastic cross-section routine, track length, boundary crossing and collision estimators added. Batch statistics implemented.
- Sept. 1984: EM-shower in “Kaskad” created trouble in geometries involving certain vacuum configurations. That has been corrected. This revision contains some features not documented in the writeup. They can be used by studying the input defined in the main program.
- Nov. 1985: Preliminary version of FLUKA86 verified running with a Fortran77 compiler. Known bugs were corrected (the only serious one was the low energy photon cross section); faster ionization energy deposition was implemented; “matregs” card in Cartesian geometry and EGS-link were added; em-cascade energy deposition can now be treated by EGS; simple calorimeter option added; leading particle biasing (possibility to input the radiation length manually) was added. Possibility for scoring the em-cascade energy only (particle type 211) was added. Energy deposited in black holes is also scored regionwise.
- Jan. 1986: First release of FLUKA86 diffractive events included in the eventq-model. First version of a new beam definition (emittance and beamvert cards) was implemented.
- Jan. 1987: First release of FLUKA87 including a new version of the eventq. Photo-production of the hadrons and nucleus-nucleus collisions were implemented. Furthermore, true compounds, magnetic fields, ionization energy fluctuations (Landau & Gaussian), boundary crossing, track-length and collision estimators for electrons, photons and positrons modified the low energy treatment.

From this point on all the work has been carried out by A.Fasso`, A.Ferrari, J.Ranft and P.R.Sala.

- May 90: Implementation of the VMS version: magnetic field transport extended to electrons and positrons, new model for multiple scattering both for hadrons and leptons, general revision and update of the event generator.
- Nov. 90: Low energy neutrons transport added with capture gamma generation, simple model for gamma production from nuclear deexcitation, natural isotopic composition of materials included, new scoring features added (USRBIN, USRBDX, USRTRACK, USRCOLL, DETECT), significant further revision of both electron/positron and photon transport performed, extensive improvements to the combinatorial geometry package with new bodies, a new tracking strategy (with large speed improvements for complex geometries) and a partial introduction of the “Dnear” facility in the transport of particles. New powerful biasing techniques added. Photoelectric effect completely changed: angular distribution for photoelectron added, edge fine structure taken into account, fluorescence X-rays produced on request.
- July 91: Final revision and update of the multiple scattering with benchmarks. dE/dx completely re-written to remove many crude approximations. Delta-ray production added. Transport threshold is now as low as the user wants it to be (inelastic interactions stop anyway at 50 MeV). Angular distribution for e^+, e^- bremsstrahlung added in EMF. Radiative energy losses for e^+, e^- changed to be consistent with Berger & Seltzer data.
- Oct. 91: New bremsstrahlung for e^+, e^- : LPM effect included, Berger & Seltzer data used also for differential cross sections. p, n inelastic cross sections updated for $10 < E < 200$ MeV. Preequilibrium model added to treat p, n interactions from the Coulomb barrier (p) or from 10-20 MeV (n) up to 260 MeV. Initialization time tabulation of cross sections for all particles introduced: accurate treatment of energy dependence of cross section for charged particles also introduced through the fictitious sigma method. Stopping π -capture introduced in the preequilibrium framework. Complete time dependence for each cascade component and full event-by-event scoring added for detailed calorimetric simulations.
- Dec. 91: Pair production by photons modified by introducing the proper angular distribution. Preequilibrium and evaporation improved. The electromagnetic part is now called EMF (Electro-Magnetic-Fluka) to stress that it is mostly new and only a minority of the code still comes from EGS4.
- Aug. 92: New dE/dx written completely from scratch; ranging of stopping charged particles was improved. Birk’s law introduced for calorimetric

- calculations. Weight windows introduced. Decay and inelastic length biasing introduced. Calorimetry-like scoring improved. Rough transport of D,T,3-He and Alphas introduced. Full revision of magnetic field transport, now based on a much more precise algorithm.
- Dec. 92: Bremsstrahlung and pair production by charged particles heavier than electrons (continuous or explicit treatment) completed. Full dump file introduced. Weight window profiles for low energy neutrons introduced.
- Oct. 93: High energy event generator upgraded. High energy fission introduced. Muon photonuclear interactions introduced. Diffractive inelastic interactions completely revised. New Compton effect with inclusion of binding effects.
- Jan. 94: Repetitive (lattice) geometry introduced. Geometry debugger introduced, geometry and magnetic field tracking revised and extended. Fluorescence updated. Photon polarization introduced in Compton, Rayleigh and photoelectric scattering. "Single chain" events introduced. "Experimental" link with DTUNUC introduced and tested.
- Aug. 94: PEANUT was completed (up to about 1 GeV for p,n, π 's and gammas for GDR and quasideuteron). Elastic scattering of p, n and π 's on hydrogen were introduced, removing of the problems of the Julich-KFA routines. Level densities improved. Leading particle biasing in EMF improved and extended to all particles.
- Mar. 95: dE/dx refined and extended with the inclusion of tabulated data for mean excitation energy and density effect. Fully new treatment of transverse p_t and of all DPM business, including a substantially improved version of Bamjet and a completely new driver model (Hdhdev instead of Hadevv) for managing two chain events. Fermi break-up introduced for light ($A < 17$) nuclei deexcitation.
- July 95: Single scattering introduced for e^+/e^- . Negative muon capture introduced within the PEANUT framework.
- June 96: Energy loss fluctuations introduced via the cumulated formalism both for heavy charged particles and for e^+/e^- . Fano correction for heavy charged particle multiple scattering introduced. Actual muon decay distribution introduced. Account for pion/muon polarized decays introduced. New defaults for several applications introduced. De-excitation gamma generation improved and benchmarked. PEANUT raised to 1.8 GeV for nucleons and pions, and up to 0.6 GeV for K^+/K^0 . $K_{\mu 3}$ and K_{l3} decays of $K^{+/-}$, K_{long} introduced with the proper matrix element.
- Jan 97: PEANUT raised to 2.4 GeV for nucleons and 1.6 GeV for pions. Residual nuclei production by low energy neutrons introduced. Nucleon decays introduced into PEANUT.

- Oct. 97: Neutrino interactions (all from tape, quasi-elastic CC and NC internally generated) added into PEANUT. Fission, including secondary production added inside the low energy neutron part. Pointwise hydrogen cross-sections. New evaporation with strongly improved treatment in all conditions particularly for residual nuclei introduced.
- Mar. 98: New chain fragmentation/hadronization tentatively in use. New diffraction according to rigorous scaling.
- Apr. 99: Cerenkov photon production and transport introduced. Full transport of heavies (d, t, 3-He and alphas, still no interactions) introduced. Heavy dE/dx effective Z effects including straggling implemented. Decay neutrino direction biasing implemented.
- Jun. 00: Coupling with NUX for full online neutrino interactions completed. PEANUT raised to 3.5 GeV for both pions and nucleons. Full transport of heavies "heavier" than alphas introduced. Heavy dE/dx effective Z effects improved with new data. Interactions still come through the interface with DPMJET.

Appendix C

Glossary

Analog Monte Carlo:

The analog Monte Carlo method is based on the fact that one executes a probability experiment (like interactions in particle physics) equal to a real process. All possible reactions are treated with their real physical probabilities.

Current:

The number of the particles crossing a surface element. In comparison to the fluence, no weighting with the angle of the crossing particle is performed. This value can be seen as a simple counting unit.

Error:

The error is the difference between a simulation (measurement) result and the pertinent real value.

Fluence:

$dN/dA_{\text{perp.}}$: the number of particles crossing a surface element divided by the fraction of this element, which is perpendicular orientated to the particle direction. This value can be also evaluated by $dN/(dA \cdot \cos\Theta)$. Θ is the angle between the normal to the surface and the particle direction.

Kerma:

"Kinetic energy released in material". This value yields the energy transfer to charged particles per unit mass of the irradiated medium. In comparison to dE/dx , the kerma factor takes also energy deposits induced by secondary particles into account. A good example can be found in case of thermal neutrons. These particles have a very low dE/dx but a high Kerma. This value is frequently used in the radiation protection field.

MDT:

Monitored Drift Tube: the most used muon chamber type in ATLAS.

Mid position:

Position of the BGO in the H6 measurement. This position is characterized by the distance between the BGO crystal and the beam axis. The BGO crystal, having a cylindrical shape of 3.8 cm in diameter and height respectively, is located between 6 cm and 10 cm off beam-axis.

Non-analog Monte Carlo:

In the non-analog Monte Carlo method the probability of special physical processes is modified. These modification techniques are called biasing techniques. The outcome of this procedure is the increase of the number of desired simulation events. On the other hand events out of interest are suppressed. Example: increased or decreased killing or secondary production probability of a particle, which undergoes a reaction.

Side position:

Position of the BGO in the H6 measurement. This position is characterized by the distance between the BGO crystal and the beam axis. The BGO crystal, having a cylindrical shape of 3.8 cm in diameter and height respectively, is located between 56 cm and 60 cm off beam-axis.

Uncertainty:

The uncertainty of a simulation (measurement) is a parameter, associated with the result of the simulation (measurement). It characterizes the possible dispersion of the simulated (measured) values around the real value.

Bibliography

- [Aar84]: P. A. Aarnio, J. Ranft and G. R. Stevenson: *A long write up of the FLUKA82 program*, CERN Divisional Report TIS-RP/106-Rev. (1984)
- [Aar84a]: P. A. Aarnio, J. Ranft and G. R. Stevenson: *First update of FLUKA82, including particle production with a multi-chain fragmentation model (EVENTQ)*, CERN TIS-RP/129 (1984)
- [Aar86]: P.A. Aarnio, A. Fassò, H.-J. Moehring, J. Ranft, G.R. Stevenson: *FLUKA86 user's guide*, CERN Divisional Report TIS-RP/168 (1986)
- [Aar87]: P.A. Aarnio, J. Lindgren, J. Ranft, A. Fassò, G.R. Stevenson: *Enhancements to the FLUKA86 program (FLUKA87)*, CERN Divisional Report TIS-RP/190 (1987)
- [Ale98]: M. Aleksa, M. Deile, N.P. Hessey, W. Riegler: *MDT Performance in a High Rate Background Environment*, ATLAS MUON-NO-98-258, CERN (1998)
- [ALI95]: ALICE Collaboration: *ALICE Technical Proposal*, CERN/LHCC 95-71 (1995).
- [Amb99]: G. Ambrosini et al.: *Measurement of charged particle production from 450 GeV/c protons on beryllium*, Eur. Phys. Jour. C10 (1999) 604
- [ATC96]: ATLAS Calorimeter Collaboration: *ATLAS Calorimeter Technical Design Report*, CERN/LHCC 96-40, 96-41, 96-42 (1996)
- [ATI:97]: ATLAS Inner Detector Collaboration: *ATLAS Inner Detector Technical Design Report*, CERN/LHCC 97-16 and 97-17 (1997).
- [ATM97]: ATLAS Collaboration: *ATLAS Muon Spectrometer Technical Design Report*, CERN/LHCC 97-22 (1997)
- [Ber72]: L. Bertochi: *Il Nuovo Cimento*, 11A (1972), 45
- [Boh39]: N. Bohr and J. A. Wheeler: Phys. Rev. 56 (1939) 426
- [Bop94]: F. W. Bopp et al.: Phys. Rev. D, 49 1994
- [Cap94]: A. Capella et al: *Dual Parton Model*, Phys. Rep. 236 (1994), 225
- [CMS:94]: CMS Collaboration: *CMS Technical Proposal*, CERN/LHCC 94-43 (1994).
- [Emm75]: M. B. Emmet: *The MORSE Monte Carlo radiation transport system*, Oak Ridge National Laboratory report ORNL-4972 (1975)

- [Eph67]: M. Epherre and E. Gradsztajn: *J. Physique* 18 (1967) 48
- [Fas99]: Alberto Fassò: *FLUKA99 manual*, available under: <http://b.home.cern.ch/b/bnv/www/fluka/>
- [Fer70]: E. Fermi: *Prog. Theor. Phys.* 5 (1950) 1570
- [Fer91a]: A. Ferrari, P. R. Sala, R. Guaraldi, F. Padoani: *An improved multiple scattering model for charged particle transport*, *Nucl. Instr. Meth. in Physics, Res. B* 71 (1992), 412 - 426.
- [Fer95]: A. Ferrari and P. R. Sala: *Physics of Showers induced by Accelerator Beams*, Lecture given at the 1995 "Frederic Joliot" Summer School in Reactor Physics, Cadarache, France, 1995
- [Fer96]: A. Ferrari, J. Ranft, S. Roesler and P. R. Sala: *Cascade particles, nuclear evaporation, and residual nuclei in high energy hadron-nucleus interactions*, *Z. Phys.* C70 (1996) 413
- [Fer96b]: A. Ferrari and P. R. Sala: *The physics of high energy reactions*, in *Proceedings of the Workshop on Nuclear Reaction Data and Nuclear Reactors Physics, Design and Safety*, Miramare-Trieste, Italy, World Scientific in press (1996)
- [Gei65]: J.A. Geibel, J. Ranft: Part VI: *Monte Carlo calculation of the nucleon meson cascade in shielding materials*, *Nucl. Instr. Meth.* (1965), 32, 65
- [Gla55]: R. J. Glauber: *Phys. Ref.* 100 (1955), 242
- [Goe71]: K. Goebel: *Radiation problems encountered in the design of multi-GeV research facilities*, CERN Yellow Report (1971) 71-21
- [Gri70]: V. N. Gribov: *Interaction of gamma quanta electrons with nuclei at high energies*, *Sov. Phys. JETP* 30 (1970) 709
- [Gsc00]: Edda Gschwendtner: *Benchmarking the Particle Background in the LHC Experiments*, PhD Thesis, CERN (2000)
- [Hän79]: K. Hänßgen, R. Kirschner, J. Ranft, H. Wetzig: *Monte Carlo simulation of inelastic hadron-hadron reactions in the medium energy range (\sqrt{s} less 3 GeV). Description of the model used and of the Monte Carlo code HADRIN*, KMU-HEP-79-07 (1979)
- [Hän84]: K. Hänßgen, J. Ranft: *Hadronic event generation for hadron cascade calculations and detector simulation I. Inelastic hadron nucleon collisions at energies below 5 GeV*, *Nucl. Sci. Eng.* 88 (1984) 537.

- [Hän84a]: K. Hänßgen, H-J. Möhring, J. Ranft: *Hadronic event generation for hadron cascade calculations and detector simulation II. Inelastic hadron-nucleus collisions at energies below 5 GeV*, Nucl. Sci. Eng. 88 (1984) 551.
- [Hän86]: K. Hänßgen, J. Ranft: *The Monte Carlo code HADRIN to simulate inelastic hadron-nucleon interactions at laboratory energies below 5 GeV*. Comp. Phys. Comm. 39 (1986) 37-51
- [Hän86a]: K. Hänßgen, J. Ranft: *The Monte Carlo code NUCRIN to simulate inelastic hadron-nucleus interactions at laboratory energies below 5 GeV*. Comp. Phys. Comm. 39 (1986) 53-70
- [Kim86]: L. Kim, R.H. Pratt, S.M. Seltzer, M.J. Berger: *Ratio of positron to electron bremsstrahlung energy loss: An approximate scaling law*, Phys. Rev. A33, (1986) 3002
- [Lan52]: L. Landau, I. Pomeranchuk: *Electron-cascade processes at ultra-high energies*, Dokl. Akad. Nauk SSSR 92 (1952), 735. Collected papers of L.D. Landau, Pergamon Press, Oxford, p. 589
- [Lan53]: L. Landau, I. Pomeranchuk: *The limits of applicability of the theory of bremsstrahlung by electrons and of creation of pairs at large energies*, Dokl. Akad. Nauk SSSR 92, 535 (1953). Collected papers of L.D. Landau, Pergamon Press, Oxford, p. 586
- [LHC98]: LHCb Collaboration: *LHCb Technical Proposal*, CERN/LHCC 98-4 (1998).
- [Mig56]: A.B. Migdal: *Bremsstrahlung and pair production in condensed media at high energies*, Phys. Rev. 103, 1811 (1956)
- [Mig57]: A.B. Migdal: *Bremsstrahlung and pair production at high energies in condensed media*, Zh. Exp. Teor. Fiz. SSSR 32 (1957) , 633, Sov. Phys. JETP 5 (1957) , 527
- [Möh81]: H.-J. Möhring, J. Ranft, J. Sandberg: *FLUKA81 - A new version of the hadron cascade code*, CERN HS-RP/IR/81-55 (1981)
- [Möh89]: H.-J. Möhring: *On the contribution of electro-production off nuclei to the generation of energetic hadrons in electromagnetic showers*, DESY 89-150 (1989)
- [Mol47]: G.Z. Moliere: *Theorie der Streuung schneller geladener Teilchen I – Einzelstreuung am abgeschirmten Coulomb-Feld*, Z. Naturforsch. 2a (1947), 133
- [Mol48]: G.Z. Moliere: *Theorie der Streuung schneller geladener Teilchen II – Mehrfach und Vielfachstreuung*, Z. Naturforsch. 3a, (1948), 78

- [Mol55]: G.Z. Moliere: *Theorie der Streuung schneller geladener Teilchen III – Die Vielfachstreuung von Bahns Spuren unter Beruecksichtigung der statistischen Kopplung*, Z. Naturforsch. 10a (1955), 177
- [Nel85]: W.R. Nelson, H. Hirayama, D.W.O. Rogers: *The EGS4 code system*, SLAC-265 (1985).
- [Pra98]: R.E.Prael et al.: proceedings of the SARE-4 conference, (1998) 171
- [Ran64]: J. Ranft: *Monte Carlo calculation of the nucleon-meson cascade in shielding, materials initiated by incoming proton beams with energies between 10 and 1000 GeV*, CERN (1964), 64-47
- [Ran72]: J. Ranft: *Estimation of radiation problems around high energy accelerators using calculations of the hadronic cascade in matter*, Particle Accelerators 3 (1972) 129-161.
- [Ran70]: J. Ranft: *Monte Carlo calculation of energy deposition by the nucleon-meson cascade and total-absorption-nuclear-cascade (Tanc) counters*, Nucl. Instr. Meth. 81 (1970) , 29
- [Ran74]: J. Ranft, J. T. Routti: *Monte-Carlo programs for calculating three-dimensional high-energy (50 MeV - 500 GeV) hadron cascades in matter*, CERN LAB II-RA/PP/73-1 (1973), Comp. Phys. Comm. 7 (1974) 327.
- [Ran83]: J. Ranft, S. Ritter: *Particle production in hadron-nucleus collisions in a multi-chain fragmentation model CERMN*, TIS-RP/103/PP (1983), Z. Phys. C20 (1983) 347-355.
- [Ran83a]: J. Ranft, S. Ritter: *The Monte-Carlo codes NUCEVT and HADEVT to simulate hadron production in hadron-nucleus and hadron-hadron collisions*, CERN Internal Report TIS-RP/IR/83-23 (1983).
- [Ran85]: J. Ranft, S. Ritter: *Rapidity ratios, Feynman-x distributions and forward-backward correlations in hadron-nucleus collisions in a dual Monte-Carlo multi-chain fragmentation mode,l* CERN TIS-RP/128/PP (1984) Z. Phys. C27, (1985) 569.
- [Ran85a]: J. Ranft, S. Ritter: *Particle production and correlations in hadron-hadron collisions in the dual Monte-Carlo chain fragmentation model*, CERN TIS-RP/137/PP (1984) Z. Phys. C27, (1985) 413-418
- [Sau31]: F. Von Sauter: *Über den atomaren Photoeffekt bei großer Härte der anregenden Strahlung*, Ann. der Phys. 9 (1931) , 217-247, Ann. der Phys. 9 (1931) , 454
- [Sch74]: H. Schönbacher: *Short write-up of standard RA-Group Monte Carlo programs available on permanent file on the 7600 computer library*, CERN Technical Memorandum LABII-RA/TM/74-5 (1974)

- [Sel85]: S.M. Seltzer, M.J. Berger: *Bremsstrahlung spectra from electron interactions with screened nuclei and orbital electrons*, Nucl. Instr. Meth. B12, 95 (1985)
- [Sel86]: S.M. Seltzer, M.J. Berger: *Bremsstrahlung spectra from electrons with kinetic energy 1 keV-10 GeV incident on screened nuclei and orbital electrons of neutral atoms with $Z = 1-100$* , At. Data Nucl. Data Tab. (1986), 35, 345
- [Ste84]: R.M. Sternheimer, M.J. Berger, S.M. Seltzer: *Density effect for the ionisation loss of charged particles in various substances*, At. Data Nucl. Data Tab. 30 (1984) , 261
- [Ter54]: M.L. Ter-Mikaelyan: *Bremsstrahlung radiation spectrum in a medium*, Dokl. Akad. Nauk SSSR 94, 1033 (1954)
- [Vin00]: Helmut Vincke: *FLUKACAD/PIPSICAD: A 3 dimensional interface between FLUKA and AutoCAD*, SATIF-5 (2000).
- [Wei37]: V. F. Weisskopf: Phys. Rev. 52 (1937) 295.
- [Wet81]: H. Wetzig, K. Hänßgen, J. Ranft, *Monte-Carlo simulation of elastic hadron nucleus reactions with the computer code NUCREL*, KMU-HEP 81-07 (1981).
- [Zie77]: J.F. Ziegler, H.H. Andersen: *The stopping and ranges of ions in matter*, Vol. 1-4, Pergamon Press, New York-Toronto-Oxford-Sydney-Frankfurt-Paris 1977

Acknowledgement

First of all I want to thank my supervisor at CERN, Chris Fabjan, for the scientific guidance and support of my thesis. Not only his knowledge about particle physics but also his way to lead a scientific project made the work with him to a real pleasure.

I would like to thank Hansjörg Müller, my supervisor of the Technical University of Graz. The discussions with him contributed a lot to the success of this thesis. It was also a great delight for me that he and his wife visited me at CERN.

A special “thank you” goes of course to Edda Gschwendtner. She was not only the main responsible person for the experiments but she also provided the project with reliable analysis results of the measurement data. The close work with her was a real pleasure for me.

I am very grateful to my brother Heinz and to Stefan Rösler. Especially in the beginning of my work at CERN, they helped me a lot in doing my first steps with FLUKA simulations. Also later on, fruitful discussions with them provided me with many hints for solving difficult calculation problems.

Thanks to Alfredo Ferrari. The discussions with him were maybe a little bit rare. But the effect of them on my work was tremendous. His enormous knowledge of particle physics and Monte Carlo simulations astonished me each time I met him.

I am indebted to Jean François Laporte and Adele Rimoldi for getting me started with Geant4 and C++.

I want to express my gratitude to the Austrian Ministry of Science for the financial support, which made my stay at CERN possible.

Also a big “thank you” goes to Martin, Adrian, Nigel and Christoph, my colleagues at CERN. I really enjoyed the time we spent together during our coffee breaks.

I am very thankful to Dave Bouffard not only for proof reading my thesis but also for being a very good friend during the last two years. Dedicated to him I changed the spelling program of my computer from British English to US English.

Thanks also to my friends Nick, Norman, Gitta and Michelle. I always had a good time when we were together.

I am very grateful to my parents for their unconditional support during my studies. Each time I return to Graz I am looking forward to be with them.

Last but certainly not least I want to thank Petra. She read my thesis accurately and provided me with helpful stylistic corrections. I am really thankful that she was at my side as often as it was possible. I really enjoyed each minute of being together with her. During the last twelve years she was the sunshine of my life.

Curriculum Vitae

Helmut Vincke

Date of birth: 06/12/67
Place of birth: Graz, Austria

Education and Qualifications:

09/74 – 07/78 Primary School in Graz

09/78 – 07/82 Secondary School in Graz

09/82 – 06/87 High School (“Bundes-Oberstufenrealgymnasium”)

10/87 – 07/96 Study of Physics at the “Technische Universität Graz”;
passed first part of diploma with distinction (average grade: < **1.1**) ;
passed second part with distinction (average grade: **1.0**).
Diploma Thesis: *Monte-Carlo-Simulation eines Neutronenspektrometers zur Bestimmung des Wassergehaltes im Marsboden (Monte Carlo Simulation of a Neutron Spectrometer in order to investigate the water contents in Mars soil)*

02/97 – 12/97 11 month civil service at the Red Cross:
(worked in an ambulance team; in my spare time I was occupied with computer business and particle transport simulations)

04/98 – 11/00 Ph.D. in physics at CERN.
Doctoral thesis within the ATLAS Muon collaboration about:
Benchmarking of the Simulation of the ATLAS Hall Background